UiT
THE ARCTIC
UNIVERSITY
OF NORWAY

Faculty of Science and Technology
Department of Physics and Technology

Waveguide Mach-Zehnder interferometer for measurement of methane dissolved in water

—

Susan M. Lindecrantz

A dissertation for the degree of Philosophiae Doctor – January 2016

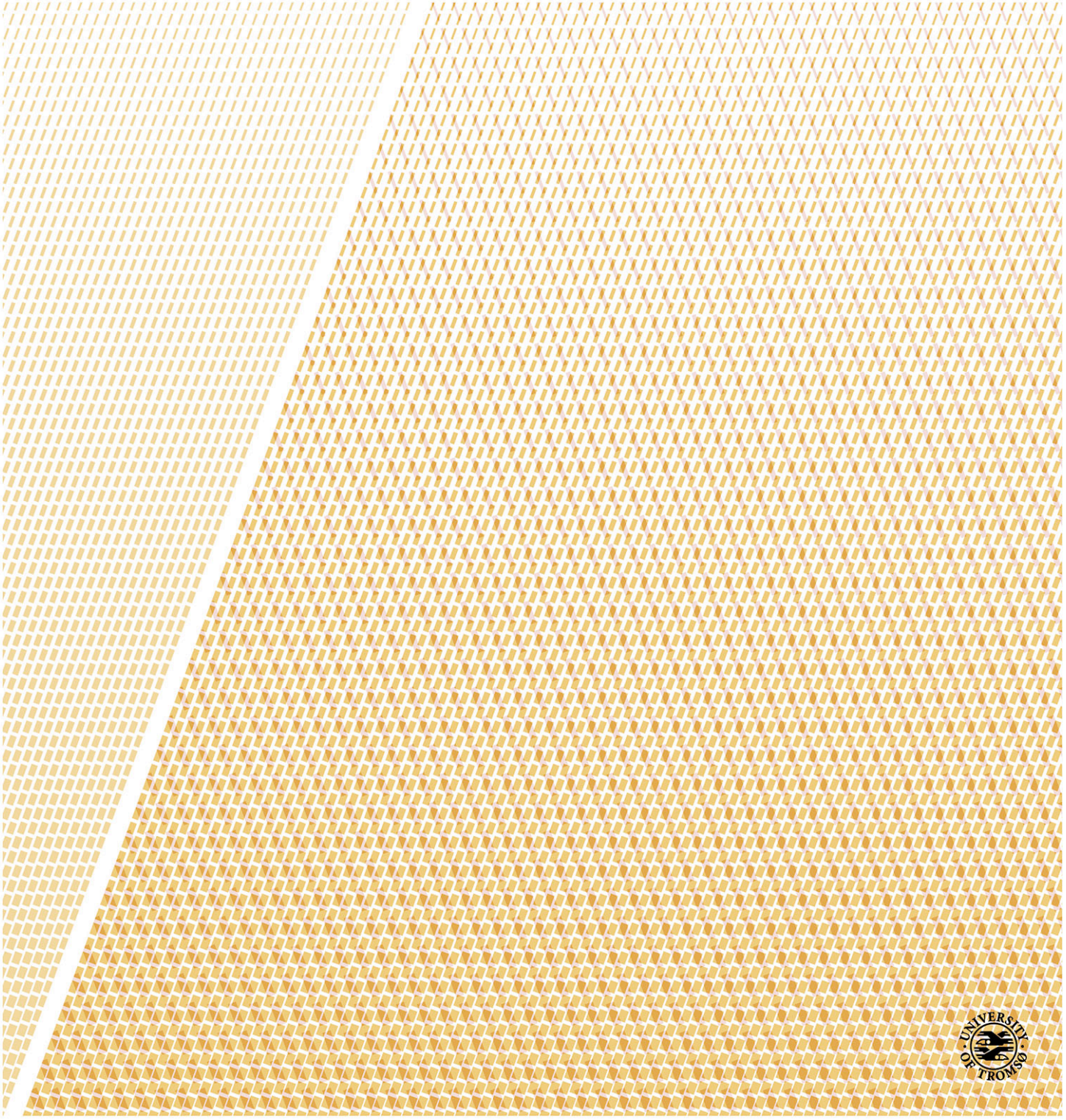

Abstract

In this dissertation, we present the development of a novel, compact and highly sensitive waveguide Mach-Zehnder interferometer to measure methane dissolved in water. Methane is a greenhouse gas, like carbon dioxide, and is emitted from both natural sources and human activities. Due to the challenges to measure dissolved methane in the sea and the vast area it covers, much of the methane cycle is unknown. In the last couple of years, there has been an up-swing in the development of subsea methane sensors. These high-end sensors rely on successfully separating the dissolved gas from the water with a membrane before the measurements, effecting the limit of detection, response time and it may give rise to hysteresis effects. Alternatively, samples can be transported to an on-shore laboratory, which can be time-consuming and expensive.

We developed a methane sensor with the possibilities of direct and in-situ detection of methane with a relatively cheap and compact optical sensor-chip. A methane sensitive layer, consisting of a host-polymer and cryptophane-A, is deposited onto the chip. Cryptophane-A is a supra-molecular compound that can entrap methane molecules within its structure and thus, induce a change in the refractive index of the host-polymer. This change is detected by the evanescent field from the waveguide, in the sensing arm of the interferometer. Thus, with a change in refractive index in the sensitive layer, a phase change between the reference and the sensing arms of the interferometer is obtained.

For obtaining optimal design, simulations were made for shallow silicon nitride rib waveguides with respect to the sensitivity as function of refractive index and the mode-behaviour of the waveguide. Once the design had been established, the waveguides were fabricated externally, with a core thickness of 150 nm, a rib height of 5 nm, rib widths of 1.5, 2 and 3 μm and sensing lengths of 1, 2 and 3 cm. The propagation losses were measured and simulated for tantalum pentoxide (similar to silicon nitride) strip and rib waveguides, to find the dependence of the propagation losses on the waveguide width. The sensitivity of the sensor was characterised with a diluted acid (HCl) and, in a separate measurement, by changing the temperature of the sensor coated with a polymer (PDMS).

The sensor was combined with a methane sensitive layer of styrene acrylonitrile (SAN) and cryptophane-A, to detect methane gas. The sensitive layer showed a 17-folded sensitivity increase with a cryptophane-A to SAN ratio of 1:9. Methane gas was measured in the range of 300 ppm to 4.4%(v/v), with a detection limit of 17 ppm. Finally, the sensor was tested with methane in water. It was found that when the sensitive layer was exposed to water, the SAN polymer showed fractures along the surface. In an effort to circumvent the problem, a protecting layer of PDMS was deposited directly onto the SAN layer. However, after some time bubble structures appeared within the layer after exposure to water. Despite this, dissolved methane was successfully and repeatedly detected for concentration in range 9 to 46 μM. A detection limit of 49 nM was obtained, showing that the sensor is suitable for measurements of methane dissolved in water.

Dedicated to the memory of my mother,
Marie Lindecrantz.

Acknowledgement

I would like to express my special appreciation and thanks to my PhD advisors Professor Olav Gaute Hellesø and Dr. Balpreet Singh Ahluwalia, in their endless encouragements, support, guidance and constructive advice of my research and for allowing me to grow as a research scientist. A special thanks for the support in my final year, through a difficult time when losing someone close to me.

I am sincerely thankful for the optics group at UiT for being such great colleagues and for creating a productive research atmosphere. To my fellow colleges in the lab, Firehun, Adit, Viktor, Martin, Jana and to the other master students I didn't mention, I am very grateful for those fun days we had in the lab.

I would also like to give acknowledge the staff of the mechanical workshop at the Department of Physics and Technology for helping us realising our mechanical designs for our setups.

In the beginning of my PhD, I had the pleasure of staying four months at the ICN2, Barcelona, Spain. I would like to thank professor Laura Lechuga and the rest of the group members for their hospitality, guidance and stimulating discussions.

A special thanks to my former advisor Zhongshan Li (from my Master of Science in Engineering studies) and lecturer Sven-Göran Pettersson at Lunds University, for their advice and tremendous support.

Finally, I would like to acknowledge the support I received from my mother, which sacrifice, tremendous strength and endless love, encouraged me to reach for the stars and fulfil my dreams. I lost you in my final year, but your encouragement and strength remains in my memories. I would also like to give thanks to the rest of the family for their support.

List of publications

Listed in chronological order:

Articles

1. Susan M. Lindecrantz and Olav Gaute Hellesø. *"Estimation of propagation losses for narrow strip and rib waveguides."* IEEE Photonics Technology Letters, vol. 26, no. 18, p. 1836–1839, September, 2014.

2. Susan M. Lindecrantz, Jean-Claude Tinguely, Balpreet Singh Ahluwalia, and Olav Gaute Hellesø. *"Characterisation of a waveguide Mach-Zehnder interferometer using PDMS as a cover layer."* Journal of the European Optical Society-Rapid publications, vol 10, April, 2015.

3. Firehun T. Dullo, Susan M. Lindecrantz, Jana Jàgerskà, Jørn H. Hansen, Magnus Engqvist, Stian Andre Solbø, and Olav Gaute Hellesø. *"Sensitive on-chip methane detection with a cryptophane-A cladded Mach-Zehnder interferometer."* Optics Express, vol 23, no. 24, p. 31564-31573, November, 2015.

Conference proceedings

1. Susan M. Lindecrantz, Firehun Tsige. Dullo, Balpreet S. Ahluwalia, and Olav G. Hellesø. *"Sensitivity of Mach-Zehnder interferometer for dissolved gas monitoring."* In SPIE OPTO, pp. 898818-898818. International Society for Optics and Photonics, March 2014.

2. Firehun Tsige Dullo, Viktor Sokolov, Cyprien Chauvet, Susan M. Lindecrantz, Stian Andre Solbø, and Olav Gaute Hellesø. *"Temperature sensitivity of waveguide Mach-Zehnder interferometer."* In SPIE OPTO, pp. 89881T-89881T. International Society for Optics and Photonics, March 2014.

Contents

Chapter 1

Introduction

1.1 Motivation

Next to carbon dioxide, methane is considered one of the most damaging gases to global warming. This greenhouse gas has become an important environmental topic because of its ability to absorb radiation in the atmosphere. Methane is the main component of natural gas and is commonly used as fuel. Vast amounts of methane are stored in the oceans and in the arctic ice, and could potentially be released into the atmosphere and further impact the greenhouse effect. Thus it is important to be able to monitor methane for climate research.

The aim of this PhD is to develop a novel, highly sensitive methane sensor, able to measure dissolved methane in water. Using evanescent field sensing, high sensitivity and on-chip integration can be achieved with optical waveguide interferometers. For this purpose, we looked into the waveguide Mach-Zehnder interferometer. Integrated optics offers potentially cheap, miniaturised sensors and waveguides that can be integrated with microfluidic systems. For this aim, optical waveguide structures are studied with regards to propagation loss, sensitivity and single-mode behaviour, and Mach-Zehnder interferometers are made.

A sensitive layer for specific measurements of methane is developed in this work. When in contact with methane, this layer should give a change in refractive index. Cryptophane-A is a supra-molecular compound that has a cavity structure with a size suitable for capturing methane molecules. With cryptophane-A mixed into the sensitive layer, the cavity can contain the methane molecules long enough to change the refractive index of the sensitive layer. Cryptophane-A is known for its high affinity towards methane and has successfully been used for optical fibre sensors, for detecting methane gas and dissolved methane [1–4]. We investigate mainly two host-polymers for the sensitive layer: polydimethylsiloxane (PDMS) and styrene acrylonitrile (SAN), doped with cryptophane-A for capturing methane.

This project was conducted in parallel with the PhD-project of Firehun T. Dullo, on sensing of methane in air using the same sensing technique. Our efforts for designing the sensor were done for the most part separately, but in collaboration. In the finale stage of the project, our efforts were combined to do measurements of methane in nitrogen. Later on, I did measurements of methane dissolved in water with the sensor.

1.2 Dissertation outline

This dissertation consists of the introductory chapters, three published articles and a concluding chapter.

Chapter 2 introduces a selection of methane sensors, divided into spectroscopic and evanescent field sensing techniques. The chapter also describes the waveguide Mach-Zehnder interferometer used in this work.

Chapter 3 presents simulations and characterisation results for waveguides and the Mach-Zehnder interferometer. The chapter describes the optical waveguides used for the project with simulation of the single-mode behaviour and expected sensitivity for the Mach-Zehnder interferometer. The chapter continuous with characterisation of the fabricated waveguides with respect to dimensions, propagation losses and measured sensitivity. The cleaning procedures and facet polishing is also briefly discussed.

Chapter 4 presents the methane-sensitive layer containing cryptophane-A. Two host polymers were studied: Polydimethylsiloxane (PDMS) and Styrene Acrylonitrile (SAN).

Chapter 5 gives an overview of the experimental setup used for methane sensing. The results for measuring methane gas in nitrogen are included in Paper 3, while the results for dissolved methane are presented in this chapter.

Chapter 6 contains the three peer-reviewed articles that are included in the dissertation:

> **Paper 1:** Susan M. Lindecrantz and Olav Gaute Hellesø. *Estimation of propagation losses for narrow strip and rib waveguides.* IEEE Photonics Technology Letters, 26(18): 1836–1839, 2014. doi: 10.1109/LPT.2014.2337055
> **Contribution notes:** Propagation losses for strip and rib waveguides were measured and simulated by Susan M. Lindecrantz. The MATLAB program for estimating the propagation losses from scattered light using a CCD camera was written by Susan Lindecrantz and Pål Løvhaugen. The article was written together by Susan Lindecrantz and Olav Gaute Hellesø.
>
> **Paper 2:** Susan M. Lindecrantz, J-C Tinguely, B. Singh Ahluwalia, and Olav Gaute Hellesø. *Characterisation of a waveguide Mach-Zehnder interferometer using PDMS as a cover layer.* Journal of the European Optical Society-Rapid

publications, 10, 2015. doi: 10.2971/jeos.2015.15020

Contribution notes: The modal behaviour and sensitivity of the optical waveguides was simulated by Susan M. Lindecrantz using COMSOL Multiphysics. These simulations were later verified and confirmed by J.-C. Tinguely using the software Fimmwave (Photon Design, Oxford, UK). All experiments were performed by Susan M. Lindecrantz. Balpreet S. Ahluwalia and Olav Gaute Hellesø supervised the project. The article was written together by Olav Gaute Hellesø and Susan Lindecrantz.

Paper 3: Firehun T. Dullo, Susan M. Lindecrantz, Jana Jàgerskà, Jørn H. Hansen, Magnus Engqvist, Stian Andre Solbø, and Olav Gaute Hellesø. *Sensitive on-chip methane detection with a cryptophane-A cladded Mach-Zehnder interferometer.* Optics Express, 23(24):31564-31573, Nov 2015.
doi: 10.1364/OE.23.031564.

Contribution notes: The experimental work was done in collaboration between Susan M. Lindecrantz and Firehun T. Dullo (joint first authors). Jana Jàgerskà contributed to the final stage of the methane sensing and wrote the main parts of the article. Jørn H. Hansen and Magnus Engqvist contributed with the fabrication of cryptophane-A and provided helpful discussions regarding cryptophane-A and the chemistry.

Chapter 7 gives conclusions and suggestions for future work that can be done to improve the sensor.

Chapter 2

Methane sensors

2.1 Why measure methane?

In the last decade, interest in the development of optical sensors for gas detection has increased due to the political and environmental focus on the effects of greenhouse gases on climate change. The amount of methane gas in the atmosphere has at least doubled in concentration over the last 300 years, since the dawn of the industrial era [5]. In the atmosphere, methane absorbs light from the sun and traps 25 times more heat than carbon dioxide [6]. Because of this it is considered a greenhouse gas. Once released, methane stays in the atmosphere for at least 10 years before it decomposes into water and carbon dioxide.

Methane is a colour- and odourless gas that is flammable above a concentration of 4.4% in air, at standard pressure and temperature (1 bar, 20^oC) [7]. Because of its chemical composition and structure, consisting of one carbon and four hydrogen atoms, the molecule is chemically stable (non-polar, symmetrical, uncharged) and is only affected by the weak van der Waals forces [8]. Because of this, it is a difficult task to detect methane with methods that require a chemical reaction.

Methane is emitted from both human and natural sources. The natural sources includes wetlands and oceans. Vast amounts of methane are stored as clathrate hydrates and permafrost in the arctic and on the ocean floors. When the climate becomes warmer, the ocean temperature will rise and may destabilise these vast methane reservoirs, potentially releasing large amounts of methane into the atmosphere. Methane also comes from human activities such as agriculture, waste management, leakage from natural gas production and transportation facilities, leakages during drilling for oil, gas or even coal mining [9] and from the use of fossil fuels.

From the ocean, samples of water have been obtained and measured in a laboratory with a gas-chromatograph equipped with a flame-ionization detector [10]. It has showed dissolved methane concentrations varying from a few nM in the near-shore and up to

1.08 μM in the deep basins in the central Baltic Sea [11]. In the summer 2012, a newly developed methane sensor (based on surface plasmon resonance) recorded methane concentrations, also in the central Baltic Sea, varying from 5 nM up to a few hundred nM [2].

To better understand the global methane cycle and being able to track the global warming effects of methane emissions from wetlands and oceans, it is necessary to quantify methane sources in-situ and in real-time with the use of optical sensors that can be deployed as a sensor grid and robust enough to be operated in extreme conditions at large depths in the oceans.

2.2 Current methane sensors

Many sensors have been designed for monitoring methane in the atmosphere and in the sea, such as acoustic [12, 13], electrochemical, metal-oxide semiconductor [14], capacitive and catalytic sensors [15]. Although some of these sensors are cheap to produce and in general simple in design, they exhibit in general low sensitivity, long-term drift and can respond to other chemical species than methane [14, 16].

Table 2.1 displays a summary of some technologies used to measure methane gas and their advantages and disadvantages, based on review articles [17, 18].

The most accurate instruments use optical spectroscopy, which is capable of detecting concentrations as low as ppb-levels. But these are usually laboratory based instruments that are expensive, bulky and require skilled personnel to be operated. In recent years, tunable diode laser absorption spectrometers (TDLAS) have been developed for in-field sensing of gas. A measurement is obtained by scanning over an isolated absorption line of methane using a narrow laser. TDLAS are able to measure methane concentrations at ppm-level [19, 20], but require methane to be in the gas phase (free from water interference).

The main limitation of sensors operating in the gas phase, such as optical and mass spectrometers, is the necessary use of gas-extraction membranes to be able to measure methane dissolved in water. This is done by using silicone membranes (e.g. polydimethylsiloxane (PDMS), Teflon) that are semi-permeable to gas [21, 22]. This is because water absorbs strongly in the infrared region and interferes with the spectral bands of interest, prohibiting the use of optical spectrometers directly on water samples. These membranes are sensitive to environmental conditions, increase the response time, influence the limit of detection and may show strong hysteresis effects[23].

Another method for measuring methane is the use of Raman-spectroscopy, which gives good selectivity, but is much less sensitive than IR-spectroscopy, with a reported limit of detection of 36 ppm [18, 24]. The reason for this is the very low Raman-scattering, which can be improved using surface enhanced Raman scattering (SERS).

Raman spectrometers can directly measure gas hydrates, gases, liquids and dissolved species [25].

Mass spectrometers are very useful for sensing methane. Just a few years ago, these spectrometers were large and laboratory based. However, development of the technique has made the spectrometers more compact, enabling measurements of methane in the field [18]. In 2012, an in-situ mass spectrometer (InSpectr200-200) was reported for measurements of dissolved methane in surface and bottom waters of coastal areas and lakes. The limit of detection was improved from previously reported 100 nM to 16 nM [23, 26, 27].

Most of today's subsea measurement systems require either that a sample is taken from location and measured in a laboratory, or the data collected during the measurement cannot be analysed on site. It would be preferable to have a stand-alone system that can measure in-situ, is remotely operated, low cost and miniaturised, but robust enough to survive in the environment of the deep or shallow ocean. Moreover, it is highly desirable to be able to deploy these methane sensors in an array in parallel fashion, monitoring several spatial locations simultaneously.

A new type of methane sensors has been developed over the last decade, using a supra-molecular compound in a host polymer. This sensitive layer, deposited onto an evanescent field sensor, changes the refractive index of the host polymer when the guest molecule is introduced into the compound structure. The change in refractive index is measured by the sensor and can then be related to the concentration of the guest molecule. There is a potential for extending the range and improve the sensitivity of these sensors. However, to bring optical sensors to the bottom of the ocean will be challenging due to the high pressure the sensor (and the wafer) would experience. The sensor would have be be placed in a protective casing. Since this has been done for other sensors such as mass- and Raman spectrometers, this should be possible with some clever engineering. Alternatively, the sensor could be measured on the surface, with water being pumped up from the ocean, as was done for the surface plasmon resonance (SPR) sensor [2].

In the following, a brief description of selected sensors used for dissolved methane is presented. These sensors can be divided into two categories: spectroscopic and evanescent field sensors.

2.2.1 Spectroscopic sensors

2.2.1.1 IR-absorption spectrometers

Infrared absorption (IR) spectroscopy is one of the most common methods for gas sensing in the environment and industry [28]. It is based on detection of a single spectral line, a transition (absorption), from the gas under investigation. Each spectral line has a

TABLE 2.1: A summary of some advantages and disadvantages of selected detection methods for methane.

Technology	Detection limit	Advantage	Disadvantage
Tunable diode laser absorption spectrometer (TDLAS)	1.1 to 6 ppm for gas[19, 20]	High resolution, sensitivity, accuracy and quick measurements of gas. Scan of single absorption line with compact diode laser.	Limited availability of the laser source, sensitive to temperature variations, challenges to maintain and operate a stable laser over time. Interference from other spectral lines in the gas. Strong water absorption lines. Requires membrane for measurements of dissolved methane.
Raman spectroscopy	36 ppm in water [18, 24]	High spatial resolution and do not require sample preparation. Indirect, in-situ measurements of gas.	Bulky and expensive equipment. It is generally laboratory based, but in recent years developed for field measurements. Low sensitivity due to the weak Raman signal. Can be enhanced by SERS. Interference problems from fluorescence.
Mass spectroscopy	100 nM to 16 nM in water [23, 26, 27]	Accurate and highly selective for detecting concentrations of methane gas. Previously used only for head-space sampling, but has recently been developed as portable unit	Bulky, consumes power and comparatively expensive. Requires membrane for measurements of dissolved methane.
Surface plasmon resonance (SPR, coated with methane sensitive layer)	lab: 0.1 nM [2], in-field: 3-7 nM [2] in water	Highly sensitive, direct, rapid, in-situ, cost-effective.	Non-selective due to refractive index sensing (unless a specific indicator for methane is used in the polymer).
fibre sensor (coated with methane sensitive layer)	0.1% (v/v)[4] for gas	Simple sensing design, in-situ, direct, rapid response and ease of operation.	Non-selective (unless a specific indicator for methane is used in the polymer). Low sensitivity.

specific wavelength, width and line shape, that is measured to identify species and to estimate the concentration of the molecule. Each molecule has its own fingerprint forming "bands" of spectral lines, emerging from the harmonics, vibration and rotation bands of the molecule of interest. An IR-absorption spectrometer contains a collimated light source such as a diode laser, an absorption cell containing the gas molecules to be investigated and a photodetector to record the transmitted intensity, as shown in Figure 2.1. The concentration of the gas is determined by the Beer Lambert's law [29] :

$$I = I_0 e^{\sigma(\lambda)} \tag{2.1}$$

$$\sigma(\lambda) = \epsilon l c \tag{2.2}$$

where σ is the absorbance (a.u.), I_0 is the initial power of the light beam, I the power after absorption, ϵ is the molar absorptivity ($Lmol^{-1}cm^{-1}$), l the path length (cm), and c the concentration of the molecule ($molL^{-1}$).

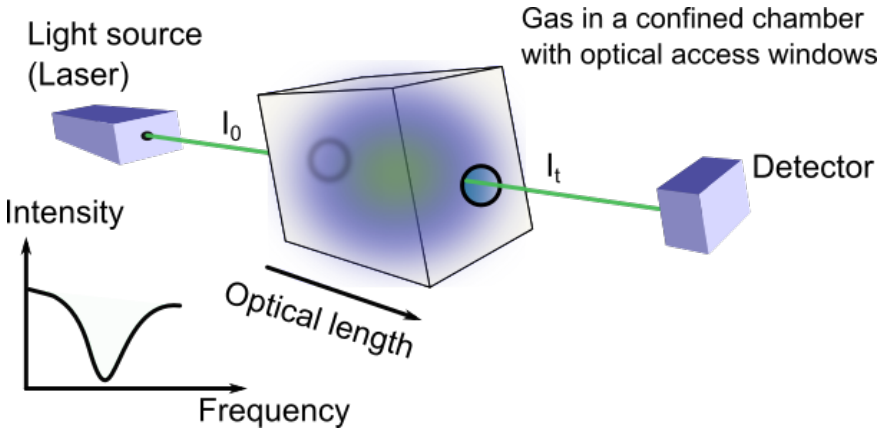

FIGURE 2.1: Principle of an IR-absorption spectrometer.

IR-spectrometers are sensitive to temperature variations since it requires time for the gas to reach thermal equilibrium. These spectrometers are also sensitive to optical noise and background absorption. The sensor is also sensitive to interference by water lines, as water has very strong absorption bands in the same regions as the hydrocarbons. Because of this water interference, to measure methane dissolved in water, the methane has to be separated from the water with a membrane system and measured in gas phase. Although these sensors are very accurate, the spectrometers are usually expensive and bulky [17]. Methane gas has been measured with TDLAS with a limit of detection of 6 ppm to 1.1 ppm [19, 20].

In 2013, a highly-sensitive methane sensor (HISEM) with laser diode for infrared absorption and equipped with a membrane inlet system, measured concentrations down to 50 nM methane in a test area off-shore and with a limit of detection of 3 nM [30, 31].

To avoid the use of membranes, a spectrometer based on a polymer coated waveguide (or fibre) has been proposed [32]. As light is guided at the interface of the waveguide-polymer, an evanescent field is produced. Any resonant absorptions from molecules occurring at this surface, give spectra similar to conventional transmission absorption spectra. The hydrophobic nature of the polymer coating prevents the water from being in contact with the evanescent field while methane diffuses through the polymer. This sensor is this also an evanescent field sensor (see section 2.2.2.2) with a polymer layer similar to the one used in this work. The output signal of the waveguide is measured with a compact Fourier Transform IR spectrometer.

2.2.1.2 Mass spectrometers

A charged particle that pass through a magnetic field, is deflected along a circular path with a radius proportional to the ratio of mass to charge (m/e). In an electron mass spectrometer, high energy electrons are used to form molecular ions and even break apart the molecule into smaller ions. Ions are focused into a beam and accelerated into a magnetic field. The ions are deflected along different circular paths depending on their masses. By adjusting the magnetic field, the ions are focused onto a detector.

Large efforts have been made to develop the mass spectrometer for underwater applications. A mass spectrometer (TETHYS) was used for in situ-measurements of methane in the deep waters of the Gulf of Mexico (down to 30 m, 200 m is possible) [33]. The relatively small compartment of TETHYS can be attached to a remotely operated vehicle (ROV) and controlled remotely for detection of hydrocarbons in the sea [34]. A limit of detection down to sub-ppm has been obtained [31, 35]. One of the limitations of the sensor is that it requires separation of the gas from the water by a membrane [34].

2.2.1.3 Raman spectroscopy

Spectroscopy based on the Raman-effect is a well established technique. Raman spectroscopy measures the scattered light from a molecule when the molecule is excited by a light source. The Raman scattered radiation has wavelengths different from the excitation source due to the exchange of energy between the incident photons and the molecule.

One of the main disadvantages of Raman spectroscopy is that the Raman scattering is weak and the species for investigation has to be Raman active. Raman scattering also competes with the much stronger fluorescence. In the ocean, there are many fluorescent

species, e.g. chlorophyll, that exhibit auto-fluorescence and can compete with the Raman measurement [36].It exhibits low sensitivity due to the weak Raman scatterering and the extremely small cross section of the Raman process ($10^{-31} - 10^{-29} cm^2$ per molecule) [35].

Surface enhanced Raman scattering (SERS) allows enhancement of the Raman signal by resonance of surface plasmons, which produce a strong electromagnetic field around the analyte. The $10^{14} - 10^{15}$ enhancement factor provided by a SERS substrate therefore allows detection of molecules at very low concentration [25].

A deep-ocean Raman in-situ spectrometer (DORISS) has been developed, using this principle, for geochemical studies at oceanic depths [37–41]. It has some challenges, as it contains fragile optical components that can be damaged during transportation. Also, it requires a vibration-free environment and temperature stability during measurements. Special attention is required in preparation of the SERS substrates. This is because the smallest variation in the SERS structures can give rise to a different amplification factor [41]. In addition, the SERS surfaces are sensitive to photo-degradation with use of high-intensity laser sources [37]. Gas hydrates containing methane has been detected near the seafloor at the Hydrate Ridge [39, 40]. A detection limit of 36 ppm [18, 24] was reported with the same sensor using proper calibration and temperature measurements.

2.2.2 Evanescent field sensors

The evanescent field of light guided in a dielectric or metallic structure can be used for sensing purposes. When light propagates through a guiding structure by total internal reflection, an evanescent field is created that is exponentially decaying from the reflecting boundaries. This is discussed further in section 2.3.1. For a waveguide, a change in refractive index of the layer within the evanescent field, will change the effective refractive index, N, of the guided mode. Examples of evanescent field sensors are surface plasmon resonance (SPR), fibres and (planar) optical waveguides, see Fig. 2.2.

2.2.2.1 Surface plasmon resonance sensor

Surface plasmon resonance (SPR) was first demonstrated in 1968 [42] and is today one of the more common principles for label-free evanescent field sensors. It measures the refractive index variation near a metal-dielectric interface in real-time. An incident light beam resonates with free electrons on the surface of a metal (gold or silver), introducing electromagnetic waves called surface plasmons. A change of the (complex) refractive index near the surface leads to attenuation of the reflected beam and a change of the resonance angle. This can be seen as a dip in the SPR reflection curve and the shape and location of the dip can be used to convey information about the environment near

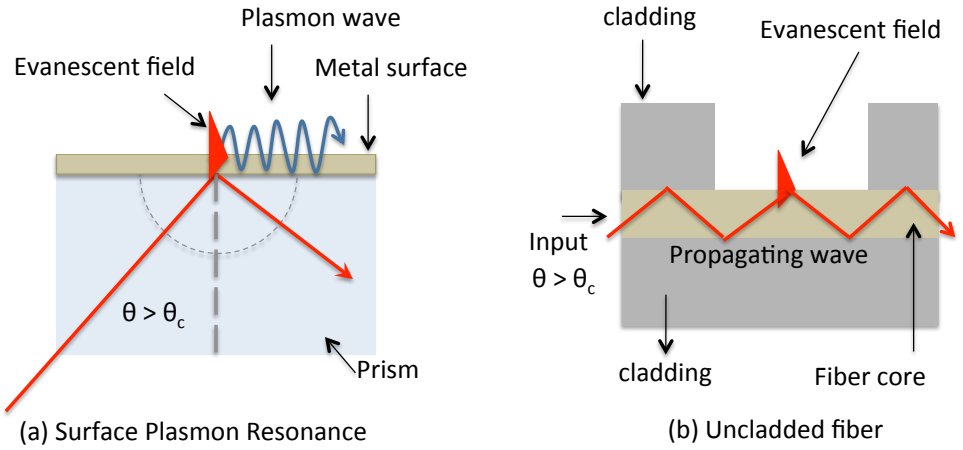

FIGURE 2.2: Examples of some common evanescent field sensors. a) shows a surface plasmon resonance (SPR) sensor with a prism and a metal layer coating. b) shows a simple fibre sensor with an uncladded sensing region. The red peaks represents the evanescent field at the sensing interface. Here θ_c is the critical angle for which total internal reflection occurs.

the metallic surface. As an example, when a molecular binding takes place on a functionalised surface, the SPR curve is shifted.

The limit of detection for SPR sensors is generally around 1×10^{-6} RIU [43], and can be improved with various techniques such as phase modulation [43, 44]. The sensor can be quite large and expensive if a tuneable laser is added to the system [45]. The SPR sensor is used in the bio-sensing community and is commercially available.

In 2001, an SPR senor was reported for hydrocarbons (including methane gas) using a gold layer coated with an isoprene rubber (IPR), with a limit of detection of 1800 ppm [46]. Later, this was improved to 700 ppm by using SPR with polarization interferometry and angle modulations [47, 48]. An SPR sensor using a polydimethylsiloxane (PDMS) layer incorporating molecules of cryptophane-A was reported to sense methane gas in 2008 [49]. The reported limit of detection was 0.2 nM. In 2013, this sensor was successfully used for measurements of methane in the Baltic Sea. The measured concentrations were from 75 nM to 130 nM, at 100 m depth. At 70 m depth, lower concentrations were found, from a few nM up to 65 nM [2]. In the field, the SPR sensor showed to have a sensitivity of 6 to 7 x 10^{-7} RIU/nM and the detection limit varied from 3 to 7 nM. [2]. The advantage of SPR sensors for dissolved methane measurements is insensitivity to water and thus separation of the gas from the water column is not required. The sensor uses a sensing layer (see chapter 4) for specific measurements and this polymer layer may degrade with time.

2.2.2.2 Fibre sensors

A fibre is an optical waveguide with a cylindrical structure, that guides light through a core with higher refractive index than the surrounding cladding. Light is guided by total internal reflection (TIR). The propagating optical wave is then bounded in the core and forms an evanescent field that reaches into the surrounding cladding. Fibres may be single-mode or multi-mode depending on the core diameter. Fibre sensors are, like optical waveguides, immune to electromagnetic interference, small in size, operating at a wide temperature range, chemically passive and have relatively low fabrication costs. Several techniques have been developed for interaction of the guided light with an external measurand, e.g. using tapered fibres, fibres with the cladding pealed off, short or long-period grating structures [50].

Several of these fibre sensors have recently been specially adapted to measure methane, by using a transparent polymer cladding with Cryptophane-A (or Cryptophane-E) deposited onto the fibre core. In 2005, Benounis et al. showed that the specific absorption of methane in Cryptophane-A led to an increase of the refractive index of the cladding [4]. They reported a limit of detection of 2% (v/v) with Cryptophane-A and 6% (v/v) with Cryptophane-E. In 2009, a mode-filtering technique was used with a silicone cladding incorporating Cryptopahane-A. The sensor was characterised for a range of 0-16% (v/v), with a limit of detection of 0.15% (v/v) [3]. A fibre sensor with a long-period grating has been reported to measure methane with a thin styrene-acrylonitrile (SAN) film containing Cryptopane-E, with a detection limit of 0.2 % (v/v) [1, 51].

2.3 Methane sensing with waveguide interferometers

Waveguide sensors have proved to be highly sensitive for biological- and chemical applications. In this work, we develop an interferometric waveguide sensor for specific detection of methane with a sensitive layer. To specifically detect methane it is necessarily to use a sensitive layer that gives a change in refractive index when interacting with methane. The following sections give an introduction to optical waveguides and the principles of evanescent field sensing. This is followed by a description of the principles of waveguide interferometers and the Mach-Zehnder interferometer used in this work.

2.3.1 Evanescent field sensing with optical waveguides

In a dielectric optical waveguide, the propagation of light can be described by Maxwell's equations. The waveguide consist of different layers. By imposing boundary conditions to these layers, the guided modes of the waveguide structure can be found. These modes are determined by the geometry of the structure, the refractive index of the different layers and the wavelength and polarisation of the light.

The simplest structure of an optical waveguide is the slab waveguide, in which light is confined by total internal reflection (TIR) between a high refractive index material (n_2) surrounded by two layers with a lower refractive index (n_1 and n_3), see Figure 2.3. Slab waveguides are not very useful for sensing applications, because they only confine light along one axis (y-axis in Figure 2.3). Instead it is more common to use channel waveguides, that confines light in two dimensions (x- and y-axis). Examples of such waveguides are strip-waveguides and rib-waveguides. The modes of a slab waveguide can be found analytically, while the mode analysis for channel waveguides is more complex and has to be done numerically.

When studying the optical modes, it is convenient to separate between transverse electric (TE) and transverse magnetic (TM) polarisation of the modes. For a TE mode, the electric field exhibits only a component perpendicular to the incidence plane, corresponding to E_x ($E_x \neq 0$, $E_y = E_z = 0$), imposing $H_x = 0$ with H_y and $H_z \neq 0$. In the case of TM polarisation, the modes are characterised by a magnetic field vector perpendicular to the incidence plane ($H_y = H_z = 0$ and $H_x \neq 0$), imposing E_y and $E_z \neq 0$, $E_x = 0$.

The effective refractive index, N, represents the guided mode as it propagates along the z-direction of the waveguide, such that $n_2 > N > n_1, n_3$. It is related to the propagation constant of the electromagnetic field, β, by $\beta = k_0 N$.

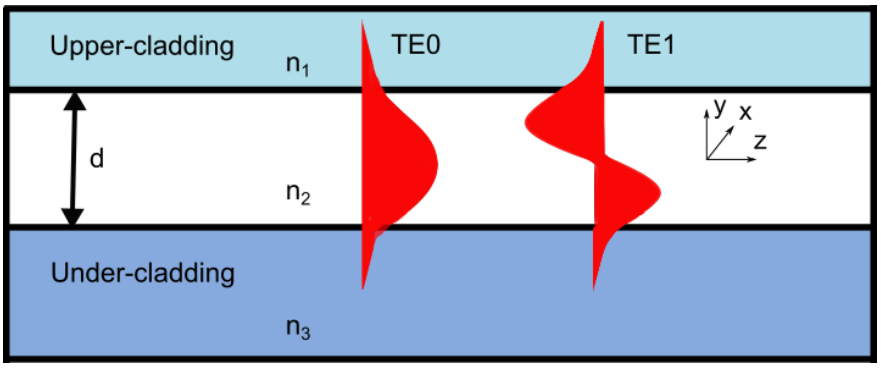

FIGURE 2.3: Shows an sketch of the fundamental transverse electric (TE0) and first transverse electric mode (TE1) of an asymmetric waveguide, such that $n_1 \leqslant n_3 < n_2$.

The waveguide can supports one or many modes. If the waveguide only support one mode, it is referred to as single-mode, while if the waveguide supports several modes it is referred to as multi-mode. See Figure 2.3 for an illustation of the two first modes of a slab-waveguide.

Away from the boundaries of an optical waveguide, the electromagnetic field of the guided light decays exponentially to zero. This part of the field, that extends into the upper and under claddings, is called the evanescent field and is illustrated in figure 2.3.

The electric component of the evanescent field decays exponentially into the (upper-) cladding according to:

$$E_x(y,z) \propto E_{x0} \times \exp^{-\alpha(y-d/2)} \tag{2.3}$$

where E_{x0} is the electric field at the interface of the waveguide, d is the thickness of the waveguide and α is the attenuation coefficient. The attenuation coefficient is given by,

$$\alpha = \frac{2\pi}{\lambda_0}\sqrt{N^2 - n_i^2} \tag{2.4}$$

where n_i is the refractive index of the upper- (i = 1) or under-cladding (i = 3) and λ_0 is the wavelength of the propagating wave. The evanescent field can reach a few hundred nanometers, up to about 1μm away, from the waveguide surface. The strength of the field depends on the dimensions of the waveguide and the difference in the refractive index between the core and the cladding. It is critical for waveguide sensors to have a strong evanescent field in the upper-cladding (i.e. sensing layer).

To achieve high intensity in the evanescent field, it is desirable to work with a waveguide material with high refractive index contrast and with thin waveguide layers ($<$ 200 nm), as shown in **paper 2**. However, it is shown in section 3.1 that to be single mode strip waveguides must be more narrow than what can be achieved by standard photolithographic techniques and give higher losses compared to rib waveguides (shown in **paper 1**). Therefore, rib waveguides were chosen for this work. The waveguides were fabricated on a silicon wafer, with a waveguide core of silicon nitride (Si_3N_4, n = 2.0) surrounded by upper- and under-claddings of silicon oxide (SiO_2, n = 1.46).

Methane, being an inert molecule, cannot be directly attached to the surface of the waveguide by means of direct chemical binding. Instead, a host polymer incorporating a supra-molecular compound, can be applied onto the surface as a sensitive layer. The supra-molecular compound captures the methane molecule so that the presence of methane can be detected by the evanescent field. Chapter 4 describes the creation and characterisation of this sensitive layer.

2.3.2 Waveguide interferometers

As early as 1804, a scientist named Young performed a very famous experiment with a double-split, showing that light could behave as waves. This played a crucial role in establishing the wave theory of light. In his experiment, light passed through two closely spaced slits, producing an interference pattern in the far-field. A century later, interference of two collimated beams was used for measurement of phase change and hence change of refractive index [52, 53].

When optical waveguides were invented, waveguide Young and Mach-Zehnder interferometers proved to be useful for sensing. Many variations of these have been proposed in the last few decades as reviewed in [54]. In this work, however, we limit our investigation to two basic configurations, the normal Mach-Zehnder and the tapered Young interferometer as seen in Fig. 2.4. These optical interferometers have shown detection limits on the order of 1×10^{-7} RIU for the Mach-Zehnder interferometer [55] and 1×10^{-8} RIU for the Young interferometer [56].

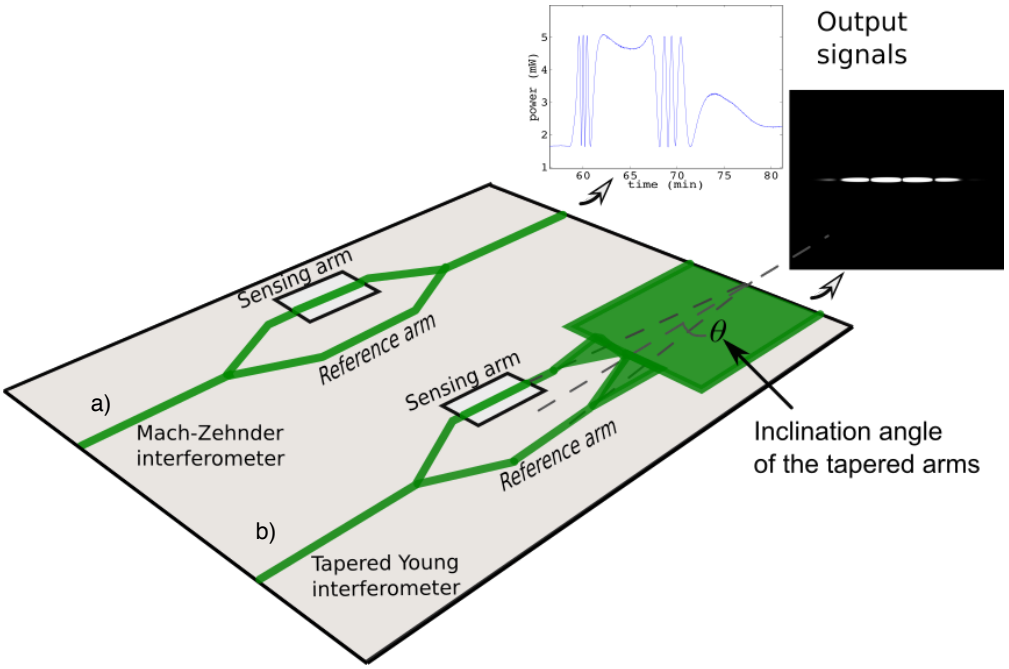

FIGURE 2.4: Showing a sketch of the Mach-Zehnder interferometer (above) and the tapered Young interferometer (below) with examples of their respective output signals.

Both interferometers have an input single-mode waveguide. The waveguide is split into two arms by a Y-juncion. The sensing arm has a window where the silica top-cladding is removed by etching, exposing the optical waveguide, where the sensing layer is introduced. The optical mode in the reference arm is protected with a top-cladding.

In the case of the Mach-Zehnder interferometer, the two arms are recombined with a second Y-junction into a single-mode output waveguide, see Fig. 2.4. A change in refractive index in the sensing window changes the effective refractive index of the guided mode in the sensing arm. When the two arms are recombined, this gives a phase difference between the two arms, which causes interference. A fringe pattern is obtained as function of time if the measurand changes.

In the Young interferometer, the tapered and inclined arms give two oblique beams, see Fig. 2.4. These are combined in a slab and give rise to an interferogram at the crossing point of the two beams. The chip is cut at the crossing point and the interference

pattern at this point is projected onto a CCD camera. The phase is obtained by monitoring the position of the interference pattern with time. This is a challenging design because the sensor chip must be cut and polished at this intersection point to give an interferogram with high visibility.

Both types of interferometers were designed and fabricated, but only Mach-Zehnder interferometers were used for gas detection due to its simple output reading. It is described further in the following section.

2.3.3 The Mach-Zehnder interferometer

For the Mach-Zehner interferometer, the phase difference between the two propagating modes is given by:

$$\Delta\phi = 2\pi\frac{L}{\lambda_0}(N_S - N_R) \tag{2.5}$$

where N_S andN_R are, respectively, the effective refractive index for the guided mode in the sensing arm and in the reference arm, L is the length of the sensing window and λ_0 is the wavelength in free space. The phase difference induces a change of the output intensity, I:

$$I = I_S + I_R + 2\sqrt{I_S I_R}cos(\Delta\phi) \tag{2.6}$$

where I_S and I_R are the intensities of the light in the sensing and reference arms, respectively. The output intensity from the waveguide Mach-Zehnder interferometer is thus directly related to the phase difference between the sensing arm and the reference arm. The phase change can then be expressed as:

$$\Delta\phi = \Delta\phi_0 + cos^{-1}\left(\frac{I - (I_S + I_R)}{2\sqrt{(I_S I_R)}}\right) \tag{2.7}$$

This can be expressed as function of the maximum and minimum values of the measured intensity (I_{max} and I_{min}, respectively) according to:

$$I_S + I_R = \frac{I_{max} + I_{min}}{2} \tag{2.8}$$

$$\sqrt{(I_S I_R)} = \frac{I_{max} - I_{min}}{4} \tag{2.9}$$

The phase $\Delta\phi_0$ is the initial phase difference between the two arms. Due to different coatings on the reference and sensing arm, the initial phase might vary. However, the temperature of the sensor was adjusted to place the output intensity in the middle of an interference fringe before each measurements, as discussed in section 2.3.3.

The intensity of the Mach-Zehnder interferometer is periodic in nature due to the cosine-term in Eq. 2.6. This gives some drawbacks such as sensitivity fading, fringe order and directional ambiguity, as illustrated in Fig. 2.5.

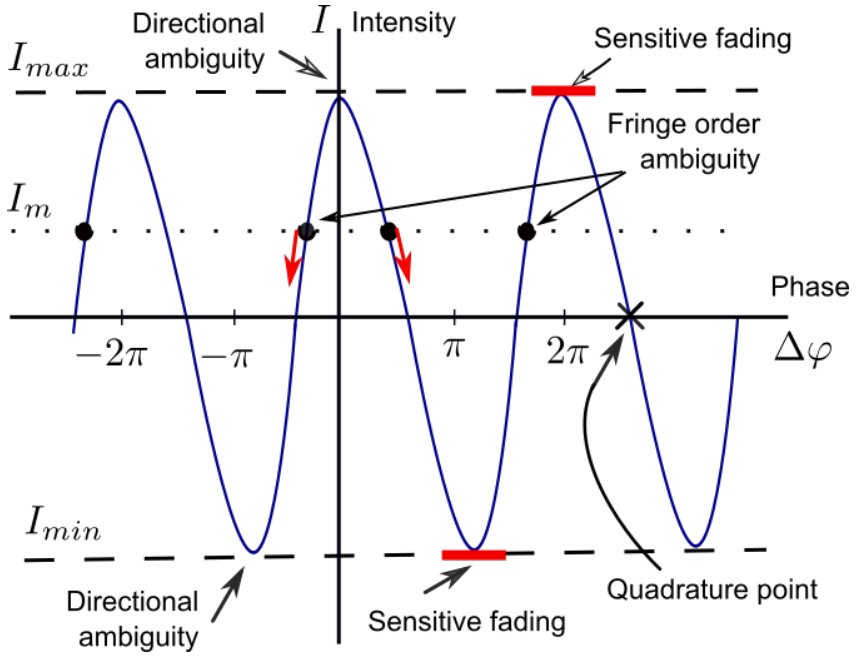

FIGURE 2.5: Sketch of the transmission curve and the intrinsic drawbacks of the Mach-Zehnder interferometer: sensitivity fading, fringe order ambiguity and directional ambiguity.

The interferometer has an initial phase between the two interferometer arms. When a phase shift is introduced, the output signal will change according to the transmission curve. Sensitivity fading occurs when the initial phase is located at one of the extremes of the transmission curve. If a small phase change is introduced at this position, it will generate a small or no intensity change compared to if the interferometer is tuned to a quadrature point. At the quadrature points, the sensitivity is at a maximum, while at the extremes of the periodic transmission curve, the sensitivity is at a minimum, giving rise to sensitivity fading. For this reason, the sensor will respond differently depending on the "working point" of the interferometer. A second problem is the directional ambiguity: if the "working point" is at an extreme point of the periodic function, the direction of a phase change cannot be determined from the output signal alone. The fringe order ambiguity occurs because any 2π integer of the phase shift is an equally probable solution. In addition, changes in temperature and fluctuations of the input-coupling can cause a drift of the "working point" of the interferometer.

To solve these intrinsic limitations, various solutions have been reported. One method is electro-optical modulation [57] and various modulation techniques (such as electro-optical, thermo-optical and wavelength modulations) [54]. The disadvantage

of electro-optical modulation is a complex fabrication process that it is no longer all-optical, but includes electrodes and electrical connections. Electrical components can be dangerous for gas detection.

A new phase modulation technique has been presented by tuning the wavelength of the light source [58, 59]. The disadvantage is, however, that an expensive tuneable laser is required. Despite its advantages and several realisations in the laboratory, the only commercially available waveguide Mach-Zehnder interferometer is, as far as we know, Optisense, for applications in bio-sensing and chemical analysis [60].

In our work, care was taken to avoid or reduce some of the drawbacks of the Mach-Zehnder interferometer. To avoid sensitivity fading and directional ambiguity, all measurements started from a quadrature point. Regarding the fringe order ambiguity, the low concentrations of methane, in the range of a few μM or less, did not give rise to a phase change larger than $\pi/2$ radians. A Peltier-element was used to stabilise the temperature during the measurements. Since the phase change for methane was so small, the temperature had to be manually tuned to find maximum and minimum intensity values to be able to calculate the phase change using Eq. 2.7, 2.8 and 2.9.

Chapter 3

Simulation and characterisation of Mach-Zehnder interferometers

In this chapter, the design and the requirements for the waveguides in the Mach-Zehnder interferometer are presented. This includes the number of modes, the sensitivity to change of refractive index and the propagation losses. The fabrication method is described briefly as it was done externally. Procedures for chip preparations (such as cleaning of chip and polishing) are included, together with some methods and results regarding the characterisation of the optical waveguides after fabrication.

3.1 Simulation of single-mode waveguides

In a waveguide Mach-Zehnder interferometer, light propagates in the sensing arm and the reference arm. If the refractive index in the upper-cladding changes in the sensing arm, the phase velocity of its guided modes change relative to the modes in the reference arm. When the two arms recombine, interference is obtained. If these waveguides are multi-mode, each mode carries information, all the modes interfere with each other and the information is averaged out, not giving clear maxima and minima. This is why it is important to have single-mode waveguides in a Mach-Zehnder interferometer.

COMSOL Multiphysics^{TM} was used for mode analysis of optical waveguides. COMSOL is a multipurpose software platform for simulating physics-based problems. In this software, the radio frequency (RF) module was chosen for 2D mode-analysis. The RF-module is based on the finite element method. The method of finding the single-mode limit is described in the following, together with some results from **paper 2**.

For the upper-cladding, different mediums were considered. When these simulations were first done, Polydimethylsiloxane (PDMS, n = 1.412) was the polymer considered as a sensitive layer. For comparison, water (n = 1.33) was also simulated as a cover medium. The layout of the shallow rib-waveguide is shown in figure 3.1. The

TABLE 3.1: Parameters used for the mode analysis.

Parameter	Dimension (nm)	Refractive index
Upper-cladding	-	1.56 / 1.412 / 1.33
-Thickness	2000	-
Core	-	2.0
-Thickness (H)	50 - 200	-
-Rib height (h)	1 - 20	-
-Rib width (w)	2000	-
Under-cladding	-	1.46
-Thickness	4000	-

simulations were made for the parameters given in table 3.1 and a wavelength of 785 nm, which is the wavelength of the laser used in the experiments.

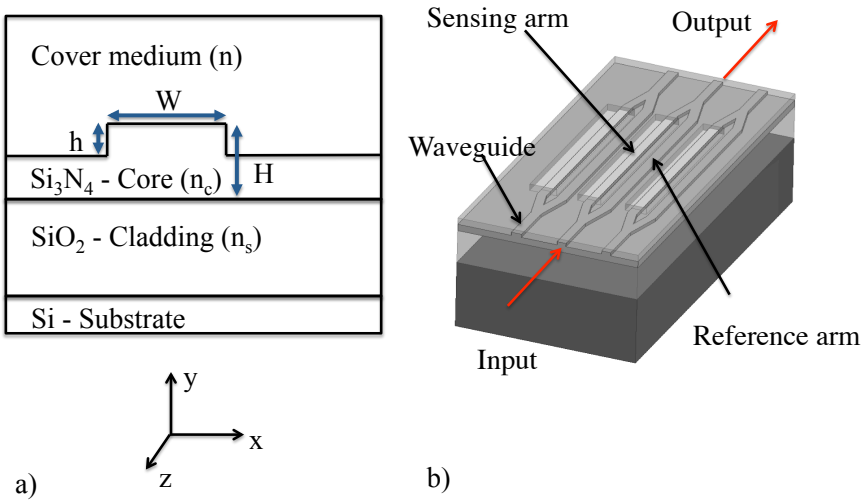

FIGURE 3.1: a) shows a sketch of the cross-section of a rib-waveguide. W is the waveguide width, H is the core thickness and h is the rib height. b) shows an illustration of the chip sensor with three Mach-Zehnder interferometers (not to scale).

The modes of the waveguide were found in COMSOL and further analysed in MATLAB, as shown in Fig. 3.2. The mode is taken to be guided when the field of the mode decreases exponentially away from the rib-waveguide.The limit between single-mode and multi-mode waveguides was thus chosen as the point where the evanescent field of the fundamental mode ceases to decrease exponentially.

Figure 3.2 shows an example of the profile of evanescent fields for different rib heights and for a structure with core thickness of 140 nm, waveguide width 2 μm and PDMS as cover medium. It shows the fields for the first order mode for TE- and TM-polarisations. For TE-polarisation, the mode becomes guided for rib heights of 8 nm and

higher. This means that the waveguide is single-mode for rib heights $\leq$ 7 nm. Likewise, for TM-polarised light, the first order mode starts to become guided at 10 nm. The rib waveguide is thus single-mode for rib heights less than 10 nm. A summary of the mode analysis can be found in figure 3.4.

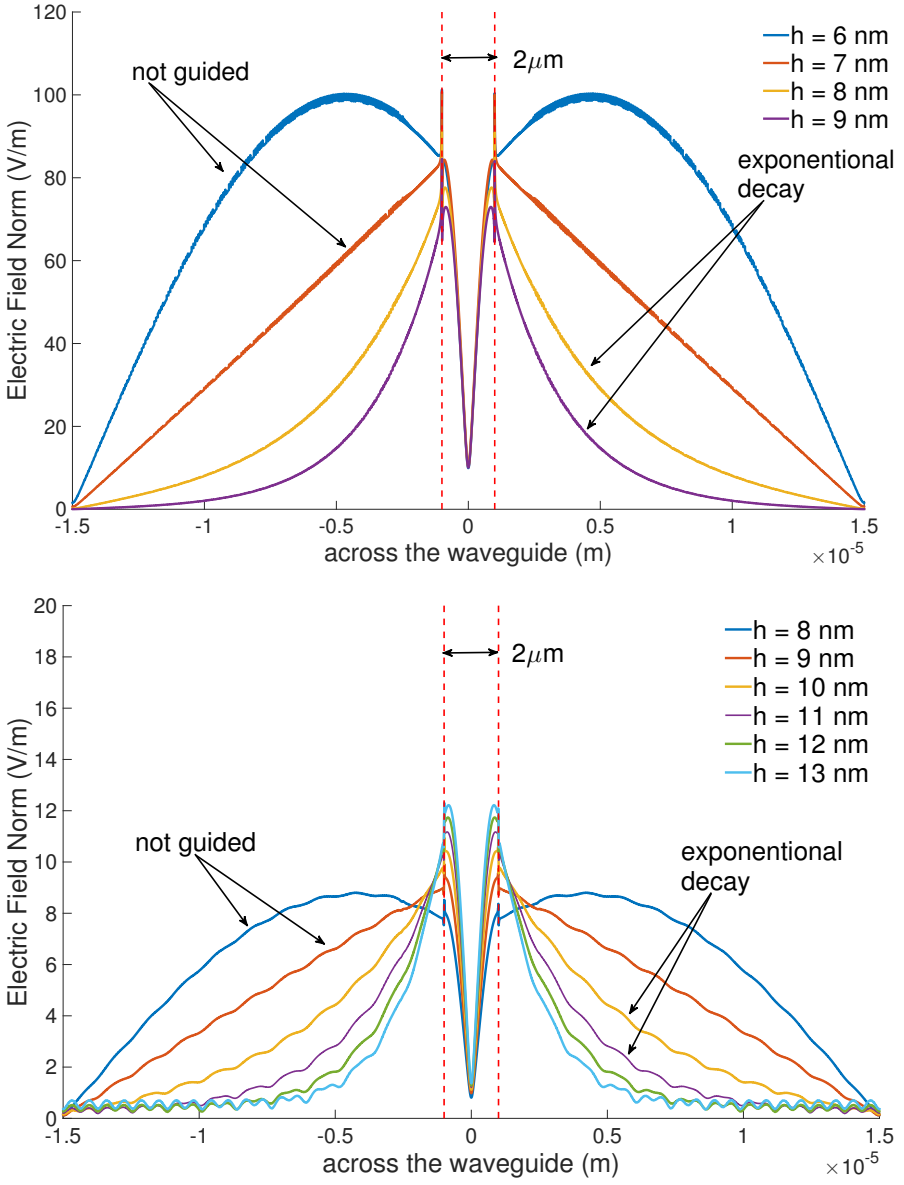

FIGURE 3.2: The evanescent field of the first order mode with PDMS as sensing layer, core thickness of 140 nm, waveguide width 2 μm and different rib heights. a) shows the field for TE polarised light (TE1) and b) for TM polarised light (TM1).

The results obtained with Comsol were later verified by Jean-Claude Tinguely, using the software FIMMWAVE (Photon Design, Oxford, UK). FIMMWAVE is based on the film mode matching method (FMM) [61]. Using Fimmwave, the single-mode limit was taken as the point where the first-order mode becomes leaky (TM-polarisation) or where its loss increases sharply (TE- polarisation) when decreasing the rib height

[62]. For both polarisations, the differences between the two methods are small and comparable to the resolution of the methods (approximately 1 nm). It has been shown previously, by reducing the rib height to 3 nm, that waveguides can be made single-mode for a width of 4 μm [63] at 633 nm.

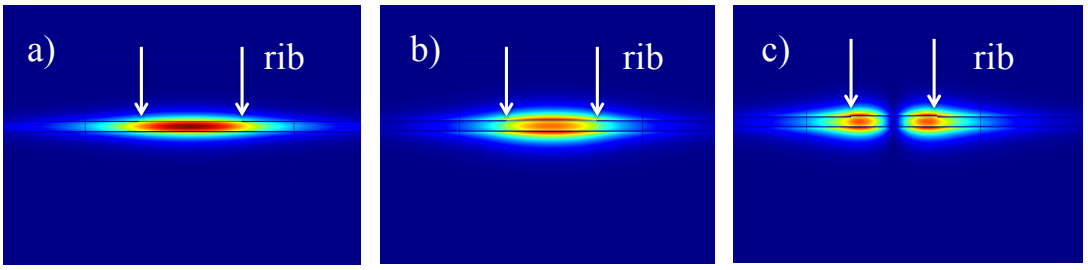

FIGURE 3.3: Examples of modes for a shallow rib-waveguide. a) and b) shows the fundamental TE- and TM-mode, respectively (5 nm rib height, 2 μm rib width and 200 nm core thickness). c) shows the first order TM-mode (15 nm rib height, 2 μm rib width and 200 nm core thickness).

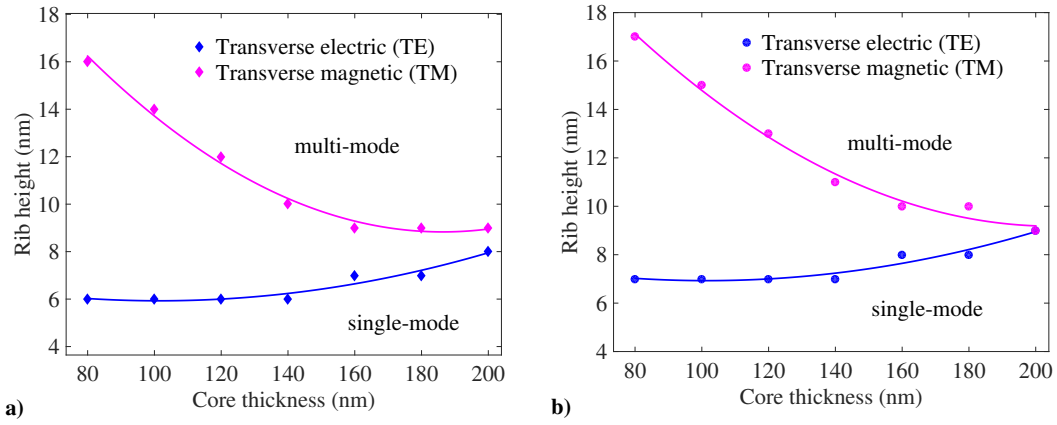

FIGURE 3.4: Limit between single-mode and multi-mode waveguides for 2 μm wide rib-waveguides for TE- and TM-polarisation and for a cover medium of a) water (n = 1.33) and b) PDMS (n = 1.412).

The single-mode limit is decreasing for TM-polarisation and slowly increasing for TE-polarisation for increasing core thickness as shown in Fig. 3.4. As the core thickness decreases towards zero, the guiding of the first-order mode will cease for any rib height. Thus, for decreasing core thickness, the single-mode limit increases. This effect is dominating for TM-polarisation. For fixed rib height and increasing core thickness, the ratio of rib height to core thickness decreases. This will, at some point, give weaker guiding and the single-mode limit will increase with core thickness. This effect causes the slow

increase of the single-mode limit for TE-polarisation. The mode-behaviour is comparable to the work published by Firehun T. Dullo, where he also investigated bending losses of our sensor [62]. For a given polarisation and core thickness, the single-mode limit is shown to be approximately the same for water, Figure 3.4(a), as for PDMS, Figure 3.4(b).

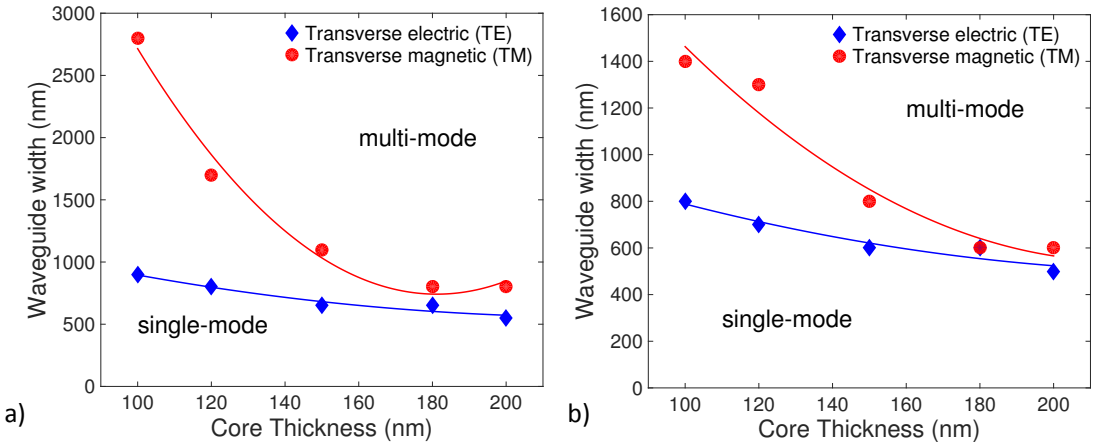

FIGURE 3.5: Limit between single-mode and multi-mode strip waveguides for TE- and TM-polarisation and for a cover medium of a) water (n = 1.33) and b) PDMS (n = 1.412).

Figure 3.5 shows single-mode limits for strip-waveguides. Single-mode waveguides are obtained for waveguide width less than 1μm, which is difficult to fabricate using standard photolithography and has high propagation losses due to side-wall roughness (see section 3.5 and paper 2). Shallow rib waveguides were thus selected for the sensor.

In conclusion, for a waveguide with width 2μm, core thickness 150 nm and TM-polarisation, a rib height less than 7 nm gives single-mode behaviour. With fabrication margins in mind, the height of the rib structure was chosen to be 5 nm. In the next section, we study the sensitivity of the sensor with different polymer layers.

3.2 Simulation of sensitivity to refractive index changes

The sensitivity to changes in the refractive index of the upper-cladding of rib-waveguides is studied. For comparison, the sensitivity for strip-waveguides was also simulated. In this section, the method used in **paper 2** is presented together with some supplementary results with styrene-acrylonitrile (SAN).

The homogeneous (bulk) sensitivity is defined as the sensitivity to variation of the effective index of a guided mode induced by a change of the refractive index of the cover medium. The surface sensitivity is defined as the sensitivity to changes in the thickness of the cover medium. It is not considered here, since the sensing layer thickness should

remain unchanged during the measurements. The homogeneous sensitivity, for a three layer slab waveguide, is given by [64, 65]:

$$\frac{\Delta N}{\Delta n_1} = \frac{n_1}{N}\frac{P_0}{P_T} * (2\frac{N^2}{n_1^2} - 1)^r \tag{3.1}$$

where n_1 is the refractive index of the cover medium, N is the effective refractive index of the guided mode, P_0 is the power of the evanescent field in the cover medium, and P_T is the total power of the guided mode. Here, r = 0 for TE-polarisation and r = 1 for TM-polarisation.

Eq. 3.1 is for a slab waveguide, but since we are using a shallow rib-waveguide with a rib height of only a few nanometers, Eq. 3.1 can be considered a good approximation.

The power fraction was estimated with COMSOL, based on the simulated power flux, $P_z(x, y)$ [W/m^2] in the direction of the propagation (z-direction). The total power flux through an area A, P_z, is then given by,

$$P_z = \iint_A P_z(x, y)\, dxdy. \tag{3.2}$$

The area A is the entire waveguide for the total power of the guided mode and the cover medium for the power in the evanescent field. Thus, with the obtained refractive index of the fundamental modes and using Eq. 3.1, the sensitivities could be estimated for TE- and TM-polarisation.

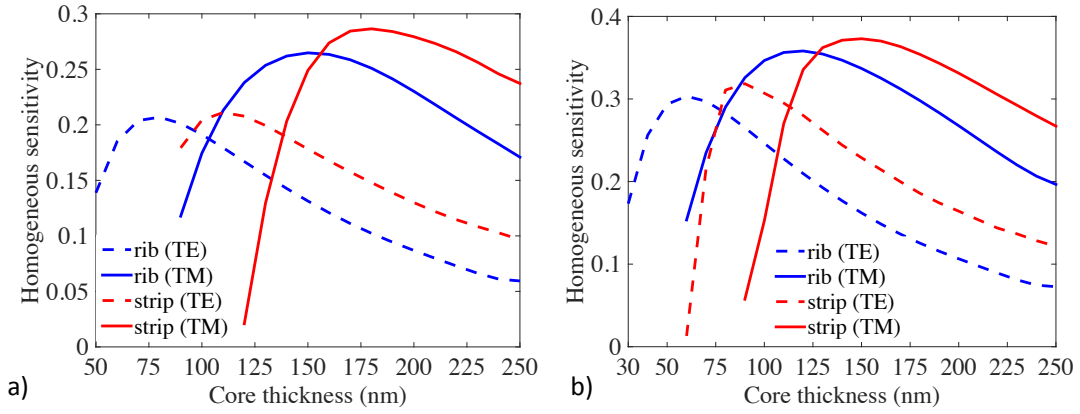

FIGURE 3.6: Shows the homogeneous sensitivity with a) water as sensing medium (n = 1.33) and b) with PDMS as sensing medium (n = 1.412). The sensitivity is shown as function of core thickness for a 0.5 μm wide strip-waveguide (red) and for a 2 μm wide rib-waveguide (blue, 5 nm rib height). Both waveguides are single-mode.

Figure 3.6 shows the sensitivity for strip and rib-waveguides as function of the core thickness. These graphs were simulated with water (n = 1.33) and PDMS (n = 1.412) as cover media. It shows that the sensitivity is in general higher for TM-polarisation than for TE-polarisation. The sensitivity as function of rib height (h) and waveguide width

(w) proved to be constant (not shown) for a fixed total thickness (H), as defined in Fig. 3.1. Instead, the sensitivity changes with the total thickness (H) since it has a bigger impact on the power in the evanescent field. This is because the sensitivity is directly proportional to P_0/P_T as seen in Eq. 3.1. Thus, when the core thickness decreases, the power in the cover medium (P_0) increases, while the effective refractive index of the mode (N) decreases, giving rise to an increased sensitivity.

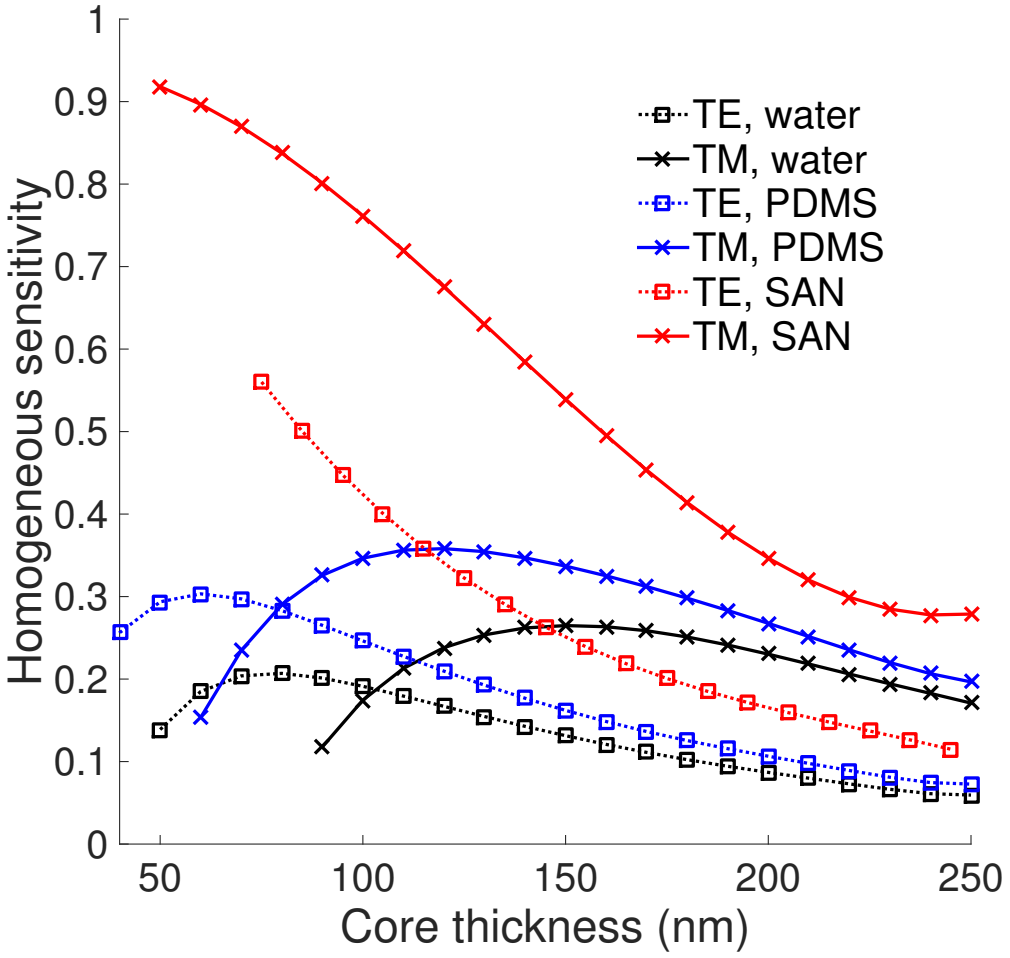

FIGURE 3.7: Shows the homogeneous sensitivity with water (n = 1.33), PDMS (n = 1.412) and SAN (n = 1.556) as cover medium. The sensitivity is shown for a 2 μm wide single-mode rib-waveguide with 5 nm rib-height.

Strip-waveguides give a slightly higher sensitivity than rib-waveguides, with the maximum of the sensitivity curve shifted to thicker cores. Strip-waveguides were not considered for the final design because the width giving single-mode waveguides was less than 1 μm, as shown in section 3.2. This would be difficult to fabricate with standard photolithography techniques.

During the experiments, it was discovered that PDMS might not be optimal as a sensitive layer, as discussed in chapter 4. For this reason, a new cover layer was

investigated: styrene-acrylonitrile. The sensitivity for SAN was not included in **paper 2** and it is thus given here.

Figure 3.7 shows the sensitivity as function of core thickness with water (n = 1.33), PDMS (n = 1.412) and SAN (n = 1.556) as cover medium for a rib-waveguide (w = 2 μm , h = 5 nm). The figure clearly shows that with higher refractive index of the sensing layer, the "maximum" sensitivity is shifted towards smaller core thicknesses. The last sensitivity point (i.e. thinnest core) for SAN as cover medium is for a core thickness of 75 nm and 50 nm for TE and TM-polarised light, respectively. No modes were found for thinner cores. This is because the fundamental mode has reached cut-off faster than when we used PDMS and water as cover layer, due to the higher refractive index of SAN.

For example, for a core thickness of 150 nm and TM-polarisation, the sensitivity is found to be 0.26 for water, 0.34 for PDMS and 0.54 for SAN. For SAN, 47% of the optical field (P_0/P_A) is located within the cover medium, as seen in Figure 3.8. The corresponding value for water is 19% and for PDMS 27%.

For a core thickness of 50 nm and TM-polarisation, the homogeneous sensitivity for SAN reaches 0.91, as the fundamental mode approach cut-off. This is a very high value for evanescent field sensing and close to the sensitivity for a free-space beam (= 1).

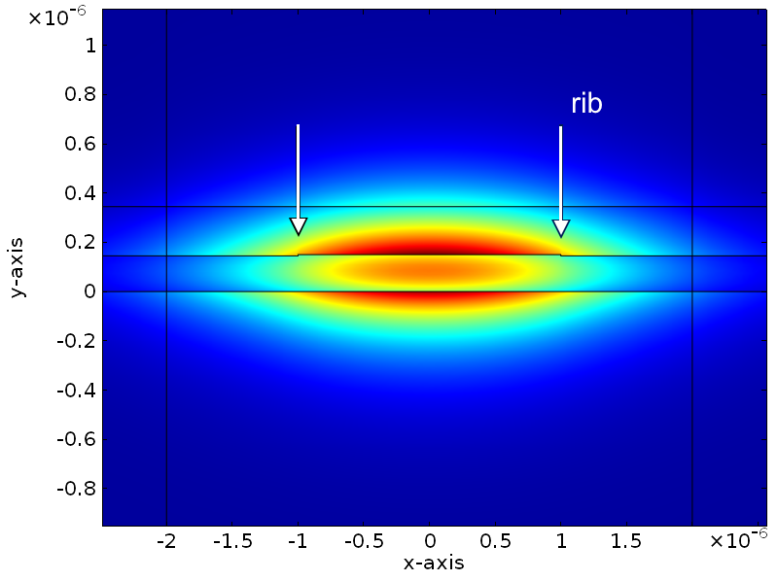

FIGURE 3.8: Shows the 47% mode-overlap for the TM0 mode with SAN (n = 1.556) as cover medium for a rib-waveguide with 2 μm width, 5 nm rib height and 150 nm core thickness.

In conclusion, a cover medium with high refractive index gives higher sensitivity with the maximum shifted towards smaller core thicknesses, approaching guiding cut-off. The sensitivity is not dependent on the waveguide width or the rib height for a fixed

core thickness. TM-polarised light gives higher sensitivity than TE-polarised light. A core thickness of 150 nm was chosen for the fabrication based on using PDMS as cover medium, giving maximum sensitivity for PDMS of 0.34.

When the dimensions of the waveguides had been determined in relation to obtaining single-mode waveguides with high sensitivity, the next step was to design and fabricate the sensors. Once the sensors were designed and fabricated, the sensitivity of the waveguide to refractive index was measured and is discussed in section 3.6 and **paper 2**.

3.3 Design, fabrication and characterisation

A set of wafers was fabricated by IMB-CNM (CSIC, Barcelona, Spain). The photolithography masks with the design were created by Firehun T. Dullo and Viktor Sokolov, based on the simulated design parameters from sections 3.1 and 3.2. Six wafers were made with the same layout and material structure, each of them with a diameter of 100 mm. Figure 3.9 shows the complete mask design made with the commercial software CleWin 5 (PhoeniX).

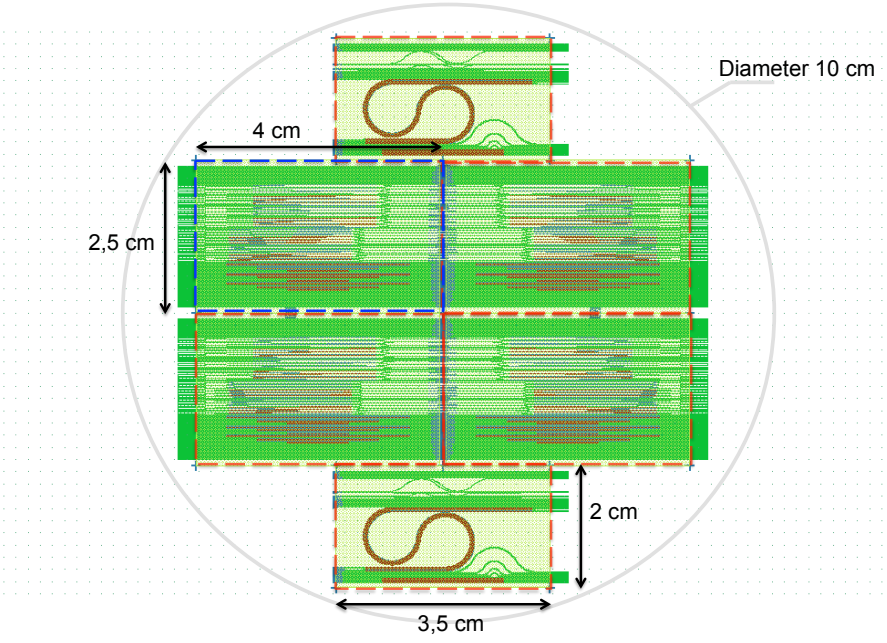

FIGURE 3.9: The layout of the photolithography mask. The wafer contains four "normal" sensor chips and two additional chips with a "special" design.

Each wafer contains six chips, with four standard chips (25 x 40 mm) and two special chips (20 x 35 mm) with straight waveguides, bended waveguides of different radius, unbalanced interferometers and interferometers with extra long sensing windows for additional characterisation. Each standard chip contains several Mach-Zehnder and Young interferometers. The chip also contains straight waveguides, with and without

tapered structures for characterisation of Young inteferometers. The interferometers have been designed with a combination of different sensing lengths (1, 2 and 3 cm), waveguide widths (1.5, 2 and 3 μm) and with a sensing window on one arm or on both arms, as seen in Fig. 3.10.

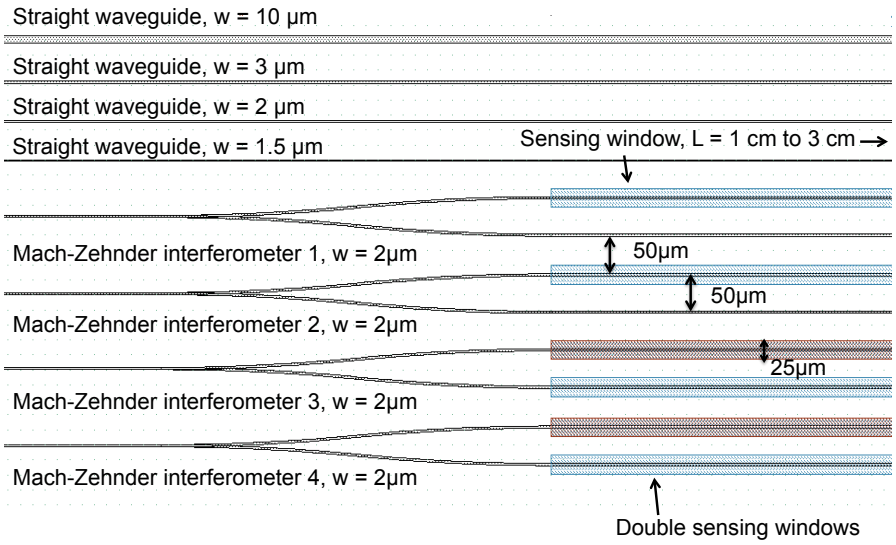

FIGURE 3.10: Shows the mask-layout for the input y-junction of the Mach-Zehnder interferometers with one or two sensing windows.

In the fabrication process, a silica (SiO_2) layer (n = 1.46) with a thickness of 3 μm was thermally grown on a 500 μm thick silicon substrate . The 150 nm thick core layer of silicon nitride, Si_3N_4 (n = 2.00) , was deposited by low-pressure chemical vapour deposition (LPCVD) at 800 °C and the rib structure of 5 nm was etched by reactive ion etching (RIE). A protective layer of 1 μm SiO_2 was deposited by plasma-enhanced chemical vapour deposition (PECVD) at 300 °C. Sensing windows were opened in the protective layer by RIE and wet etching. These windows were 1, 2 and 3 cm long, 1 μm deep and 25 μm wide. The two arms of the Mach-Zehnder interferometer were separated by 50μm, see Fig. 3.10.

After fabrication, the actual dimensions of the rib-waveguides were verified with atomic force microscopy (AFM) and scanning electron microscopy (SEM), by Dr. Stefania Dante (Nanobiosensors and Bioanalytical Applications Group, CIN2, CSIC). The topography was scanned in the sensing area with AFM, where the cladding has been etched away and the core is accessible for measurements. Fig. 3.11 shows an example from the AFM scan of the rib-waveguide with a nominal height of 5 nm and width of 2 μm. It displays a 3D topography image, a phase image and the average profile of the waveguide. In this case, the rib-waveguide was estimated to be 5.7 nm high and 2.23 μm wide. A summary of the measured values for two interferometers is shown in table 3.2.

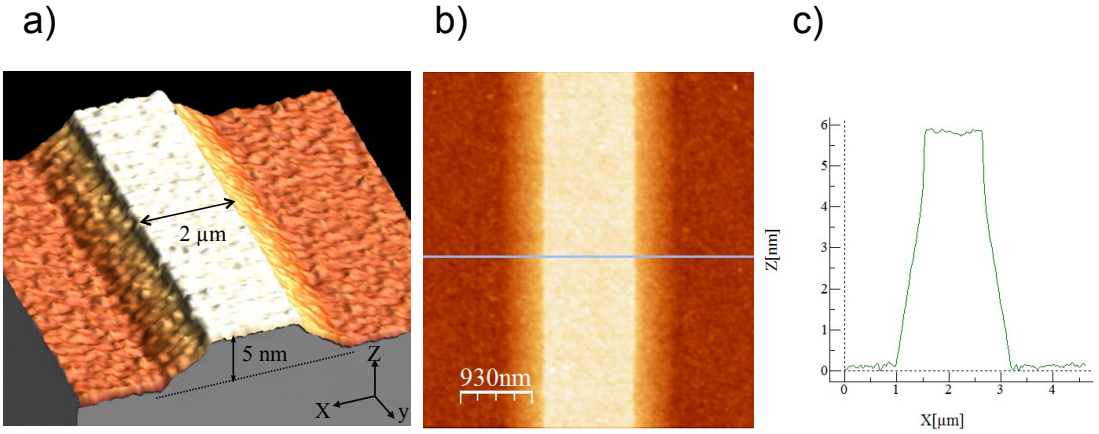

FIGURE 3.11: Shows an example from an AFM scan of the fabricated rib-waveguide (chip 2 in table 3.2). The image shows a) the 3D topography from the scan b) the corresponding phase image and c) the average profile. The dimensions are evaluated from the average profile.

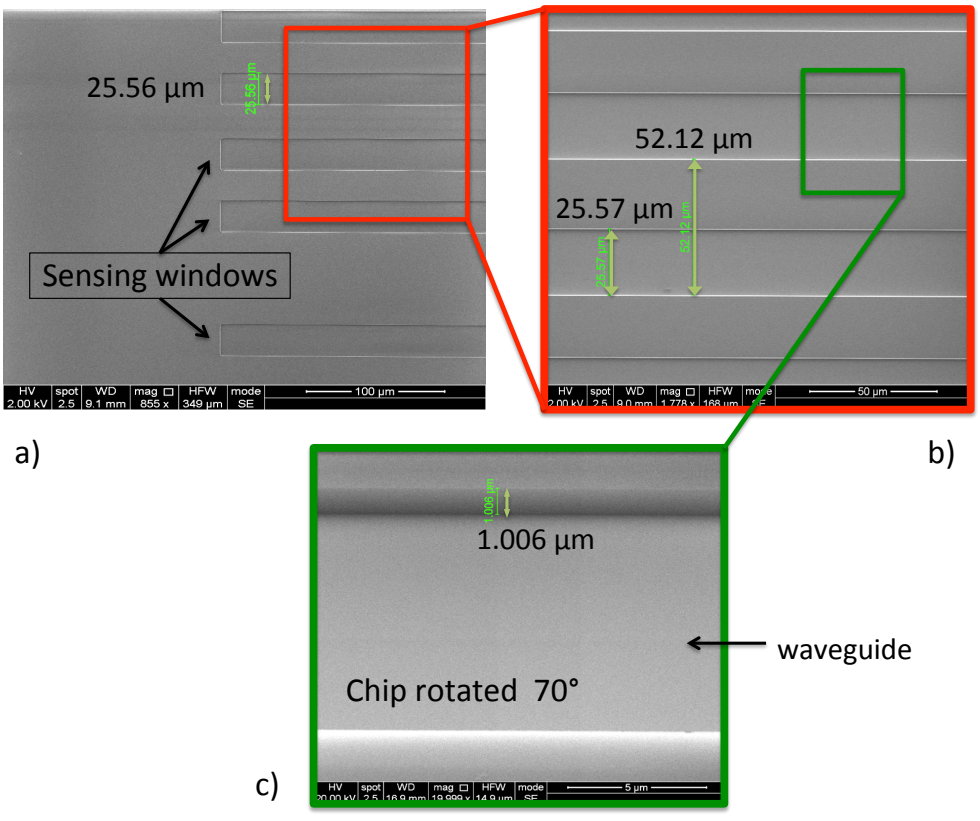

FIGURE 3.12: a) Shows a SEM image of the surface of the fabricated sensor with the sensing windows. b) shows a zoomed in image of a) and c) shows a zoomed-in image of b) with the sample rotated 70° to measure the height of the sensing window (1μm). The sensing window has been etched with a width of 25 μm, lengths of 1, 2 and 3 cm respectively (not shown here). The arms of the interferometers are separated by 50 μm.

TABLE 3.2: Displays the measured width and height of the rib-waveguides from two different chips using the average profile from the AFM characterisation.

Chip 2		
Nominal width (μm)	Measured width (μm)	Measured height (nm)
1.5	1.81	5.7
2.0	2.30	5.8
2.0	2.23	5.7
3.0	3.33	5.7
Chip 3		
Nominal width (μm)	Measured width (μm)	Measured height (nm)
1.5	1.89	5.8
2.0	2.40	5.7
3.0	3.40	5.8

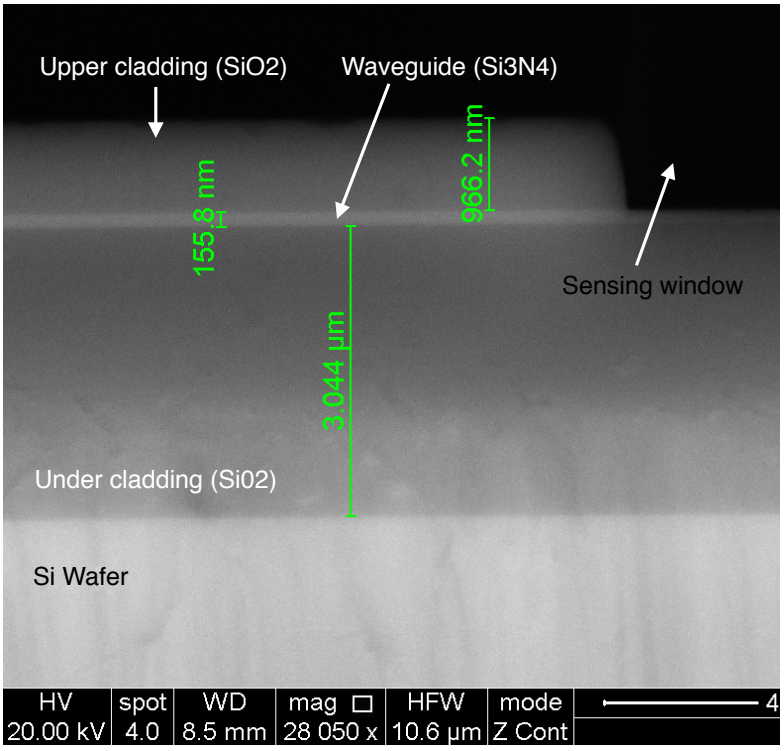

FIGURE 3.13: Shows a SEM image of the cross-section of the rib-waveguide. The thickness of the upper-cladding (SiO_2) is estimated to about 1 μm, the core thickness 150 nm and the thickness of the under-cladding 3 μm.

In addition, the cross-section of the chip was investigated by scanning electron microscopy (SEM), as seen in Figures 3.12 and 3.13. The thickness of the upper-cladding (SiO_2) is estimated to about 1 μm, the core thickness 150 nm and the thickness of the under-cladding 3 μm. The sensing window width, height and the separation of the interferometer arms was also measured, see Fig 3.12, and can be compared to Fig. 3.10.

3.4 Chip preparation

Each chip is polished manually at the end-facets to minimise insertion loss during end-fire coupling. This was done with a polishing machine. The chip was placed vertically to the rotating platform with a polishing paper. Polishing papers are applied with decreasing grain size, starting from 20 μm, 5, 1, 0.3, and down to 0.1 μm. A constant water flow is applied to the location of the polishing, to wash away particles from further damaging the surface of the chip. After each polishing step, the surface of the facet is studied with a microscope before the next grain-size is applied.

Prior to deposition of a sensing layer or characterisation of a new chip, the chip has to undergo a cleaning procedure to remove any dust or unwanted residuals from the polishing. In the cleaning process, the chip is first wiped with a clean-room swab soaked in acetone. The chip is then sonicated successively in acetone, isopropanol and distilled water for 5 min in each liquid. Once sonicated, the chip is blow-dried with nitrogen (N_2) gas.

Then the chip is introduced to a 5% Hellmanex III solution, which is heated to 70°C for at least 10 min. If the chip is really dirty, the chip is placed in 1:1 HCl:MeOH and sonicated for another 10 minutes. The chip is finally rinsed with distilled water and blow-dried using N_2 gas.

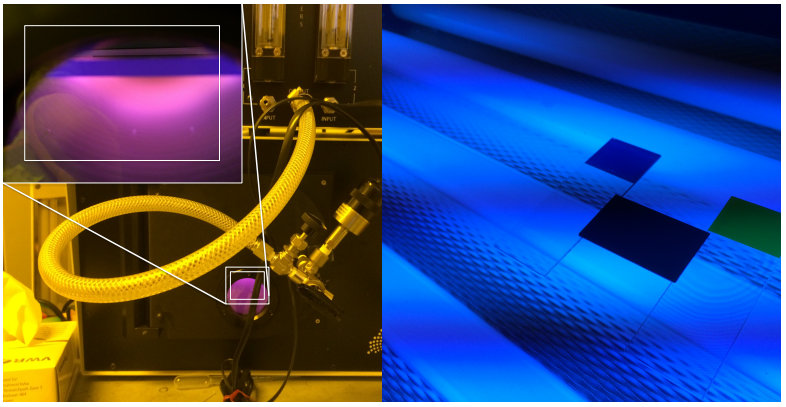

FIGURE 3.14: Displays methods for oxidation of the surface: (left) air-plasma treatment of the chip and (right) UV-exposure of the surface.

Prior to deposition of the methane sensitive polymer coating, discussed in chapter 4, the chip surface was silanized to improve the adhesion between the methane sensitive layer and the waveguide surface. After the cleaning process, the surface is activated with exposure of UV-light for at least 1 hour. Alternatively, the chip can be placed in air-plasma chamber, see Fig. 3.14, for 5-10 minutes to activate the surface. After activation, the chip is immersed into a silane solution for 1 hour. The silane solution consists of 50 μL of 1% 3-aminopropyl-riethoxysilane (APTES) in 4.9 mL of ethanol.

The silanised chip was rinsed in ethanol and distilled water and then dried with N_2. Once dried, the chip is placed in an oven at 110 °C for 1 hour. The chip is now ready for deposition of the methane sensitive layer.

For recycling the silanized chip, the chip is placed in Dynasolve 218 solution for at least 30 min (overnight if possible) and rinsed with isopropanol and distilled water. The solvent Dynasolve 218 dissolves cured silicone, and can also dissolve polymers such as PDMS. The same cleaning procedures, as described above, are then used. Finally, the chip is also exposed to air-plasma, see Fig. 3.14, for at least 5 minutes.

3.5 Simulation and measurement of propagation losses

Propagation losses as light propagates along a straight optical waveguide, can be caused by absorption, imperfections from within the waveguide material and scattering from surface roughness of the waveguide structure. In dielectric waveguides, the absorption loss is expected to be small compared to the scattering loss due to surface roughness.

The most common experimental method to determine propagation losses is the cut-back method, which is a destructive method since the chip is successively shortened [66]. Most analytical methods to estimate the scattering losses, require knowledge about the standard deviation and the autocorrelation length of the sidewall roughness [67–70]. These parameters can be measured by atomic force microscopy (AFM). For shallow rib (1-10 nm) and thin strip-waveguides (thickness 200 nm and below), this is a challenge.

In **paper 1**, a non-destructive method is described and used for measuring the propagation losses for rib and strip dielectric waveguides. The measured propagation losses were also used as a reference to estimate the propagation losses of waveguides with different widths. Waveguide with a core of tantalum pentoxide were used in paper 1.

Once the silicon nitride waveguides had been fabricated, the propagation losses were measured to 0.8 - 1.3 dB/cm, using the same method as in paper 1. These measurements were made by master student Martin Ingvaldsen.

3.6 Measurement of sensitivity to refractive index changes

The sensitivity of the waveguides to refractive index change was measured with two different methods. For the first method, the concentrations of HCI was varied between 0.03 M and 0.3 M (measured with a refractometer) and the resulting phase change measured with a Mach-Zehnder interferometer. HCl was supplied directly to the waveguide surface by a microfluidic system connected to an injection port.

For the second method, the sensing window of the interferometer was covered with PDMS. By increasing the temperature of the chip with a Peltier-element, the refractive

index of the PDMS changes, thus giving rise to a phase change. This is because the thermo-optic coefficient of PDMS ($\Delta n/\Delta T = -4.2 \times 10^{-4}$ RIU/K) on the sensing arm, is different from that of silica ($\Delta n/\Delta T = 1.28 \times 10^{-5}$ RIU/K, [71]) on the reference arm. Table 3.3 gives a summary of the sensitivities obtained for 1, 2 and 3 cm sensing lengths with both methods. This work was published in **paper 2**, together with the simulation results in sections 3.1 and 3.2.

TABLE 3.3: The sensitivities for various sensing lengths, with water or PDMS as the cover medium in the upper-cladding. L is the sensing length, S is the phase sensitivity as function of the refractive index S(n) or temperature S(T), dP is the mean visibility of the fringes, σ is the noise of the signal, $\Delta\theta_{min}$ is the minimum phase change that can be detected and LOD is the limit-of-detection as function of refractive index, LOD(n), or temperature, LOD(T).

Cover medium:	**HCl-solution**			**PDMS**		
$Sensinglength, L\ [cm]$	1	2	3	1	2	3
Simulated $S(n)\ [\times 10^3 \pi rad/RIU]$	6.7	13.5	20.2	8.5	17.2	25.7
Measured $S(n)\ [\times 10^3 \pi rad/RIU]$	6.5	13.0	19.8	8.8	15.2	26.2
Measured $S(T)\ [\pi rad/K]$	–	–	–	3.7	6.4	11.0
$dP\ [mW]$	3.4	0.6	0.8	0.7	1.4	0.7
$\sigma\ [\mu W]$	7.1	0.9	9.0	1.9	2.8	4.0
$\Delta\theta_{min}\ [\times 10^{-3} \pi rad]$	6.3	4.5	33.7	8.1	6.0	17.1
$LOD(n)\ [\times 10^{-7} \pi RIU]$	3.1	1.1	5.4	3.0	1.3	2.1
$LOD(T)\ [mK]$	–	–	–	2.2	0.9	1.6

In conclusion, the measured sensitivities showed good correspondence with the simulated sensitivities obtain in section 3.2. As expected, the sensitivity increased linearly with the length of the sensing windows. Due to the higher noise for 3 cm sensing length than for 2 cm, as discussed in paper 2, the limit of detection is lowest for a sensing length of 2 cm, at 1.1 and $1.3 \times 10^{-7} \pi rad/RIU$ for water and PDMS, respectively. With PDMS on the sensing arm of an unbalanced Mach-Zehnder interferometer, the corresponding limit of detection for temperature is approximately 1 mK.

Chapter 4

Methane-sensitive layer

To measure methane with evanescent field sensing, the methane molecule has to be accumulated in the immediate vicinity to the waveguide surface. Since the methane molecule is by nature highly symmetrical, uncharged and non-polar, it is difficult to chemically bind the molecule to the surface using receptors [8].

In recent years, a new field has been developed to circumvent this problem by encapsulating the molecule within a cavity structure of an organic supra-molecular compound. With this technique, the methane molecule can be encapsulated into the cavity by van der Waals forces and released again, after being sensed. For this purpose, cryptophane-A has been developed, which has shown to have high affinity towards methane because the molecule fits well within its cavity. An optically transparent polymer can act as a host for cryptophane-A and the polymer doped with cryptophane-A can be deposited onto the surface of the waveguide sensor. When methane is captured, the refractive index is locally changed in the host-polymer and its accumulated effect can be measured by our sensor.

In this chapter, we briefly discuss cryptophane-A and the polymers studied to be used as host-polymer for sensing methane: polydimethylsiloxane (PDMS) and styrene acrylonitrile (SAN). We also discuss the different methods of deposition, mixing and dissolving cryptophane-A into the polymer.

4.1 Cryptophane-A

Cryptophanes are organic super-molecular structures, forming cavities of different sizes depending on their chemical construction. The smallest in the cryptophane family, cryptophane-A, was first developed by André Collet et al, in 1981 [72]. The internal cavity volume of cryptophane-A has been estimated to be 81.5 $\mathring{A}^3$ [72] and, in more recent works, 95 $\mathring{A}^3$ with computational modelling [73, 74]. Cryptophane-A is able to fit a neutral molecule within its cavity. It can bind effectively with methane, which has a volume of 28 $\mathring{A}^3$ [8, 75]. In addition to methane, other small neutral molecules like

xenon (molecular volume of 42 $\AA^3$) and chloroform (molecular volume of 72 $\AA^3$) have some affinity towards cryptophane-A [74, 76]. In this work, we will use cryptophane-A to detect methane.

A sketch of the steps to synthezise cryptophane-A and its structure is shown in Figure 4.1. Cryptophane-A was prepared from commercial vanillin according to a published procedure [77] and purified by column chromatography. The synthesised material was characterised by NMR and high-resolution mass spectrometry, and found to exhibit identical properties to those reported [78], including host-guest behaviour towards methane. The material was prepared to high purity ($\geqslant$96 procent) as determined by liquid chromatography-analysis. The synthesis and characterisation was done by Magnus Engqvist and Jørn H. Hansen from the Department of Chemistry, UiT. The synthesis produces cryptophane-A in powder form.

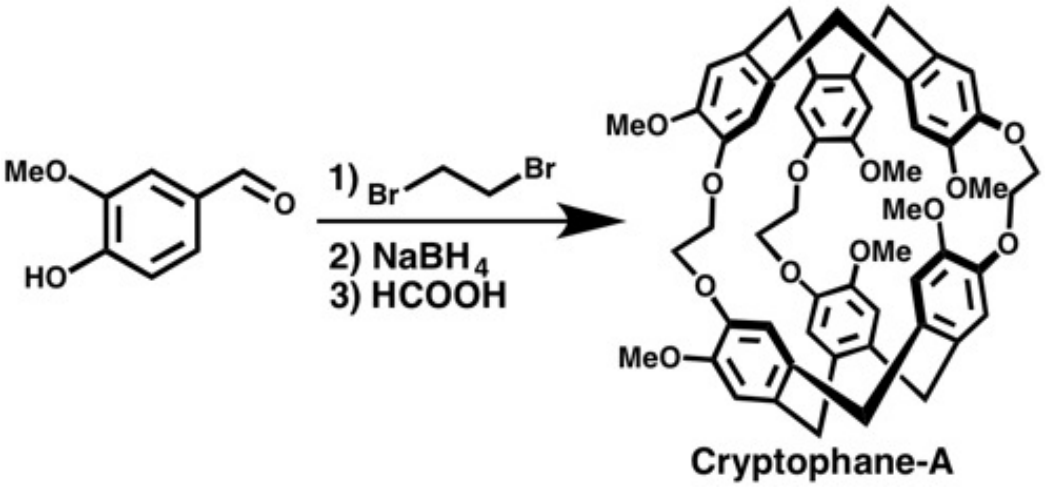

FIGURE 4.1: Shows the synthesis steps used by the group from the Department of Chemistry (UiT) and the structure of cryptophane-A.

Methane penetrates into the host-polymer and is trapped inside the cavity structure of the cryptophane-A by weak Van der Waals forces [79]. As light propagates along the waveguide, its evanescent field reaches out into the host-polymer. The encapsulation of the methane molecule results in a local change in refractive index of the host-polymer and is detected by the evanescent field of the guided mode. This changes the effective refractive index of the guided mode in the sensing arm of the sensor. When the reference and sensing arms of the Mach-Zehnder interferometer are recombined, as described in chapter 2, the concentration of methane can be correlated to the change of refractive index of the host-polymer. Benounis et al. (2005) [4] showed that the refractive index of the host-polymer increased proportionally to the concentration of encapsulated methane using a fiber sensor.

4.2 Host-polymer

The methane-sensitive layer consists of cryptophane-A and a host-polymer. The host-polymer must meet a few criteria. The polymer has to be optically transparent to avoid additional scattering in the sensing arm and thus propagation losses. The refractive index must be lower than that of the waveguide core to produce total internal reflection and give rise to a strong evanescent field. A strong evanescent field and a long interaction length are key requirements for obtaining high sensitivity for the optical waveguide sensor. The polymer must also be open to diffusion of the methane gas, i.e. exhibit high permeability to methane. In addition, the polymer has to be compatible with the solvent that dissolves the cryptophane-A powder.

As mentioned in chapter 2, other types of evanescent field sensors have been using cryptophane-A for sensing methane. Based on these published works, the most commonly used host-polymers are polydimethylsiloxane (PDMS) and styrene acrylonitrile copolymer (SAN). In the following sections, these two polymers are studied for our sensor.

4.2.1 Polydimethylsiloxane

Polydimethylsiloxane (PDMS) is a silicon rubber. It is widely used due to its simple fabrication and ability to create structures of a few hundred nanometer in size with soft lithography techniques. In bio-sensing, it is often used for creating mircofluidic channels [80]. It has also been used for optical waveguide devices [81]. PDMS is, by itself, an optically transparent polymer with a refractive index of 1.412. It has a high permeability to methane [21, 35].

In the first set of tests, 5 mg cryptophane-A was dissolved with 0.9 ml of the solvent tetrahydrofuran (THF). PDMS was made by mixing 0.1 ml of siloprene (K1000, Sigma-Aldrich) with 0.01 ml of cross-linking agent (K11, Sigma-Aldrich). The mixture was stirred vigorously with a glass-pen. PDMS was then mixed with the dissolved cryptophane-A. A few droplets of the mixture were placed on the chip and uniformly distributed by spin-coating at 4500 rpm for 2 minutes. The chip was cured at 80 °C for at least 10 hours before any measurements were done.

Figure 4.2 shows an example of the sensitive layer when using THF as solvent with PDMS. It shows that the sensitive-layer is not optically transparent and contains undissolved residuals. This was already observed during the mixing-process, as the fluid mixture at this stage was not transparent. Various mixing techniques were applied (mixing with pulses of ultrasound, mechanical stirring using a magnetic pin, with and without heating), but all tests showed the same result. In previously reported works [2], [4], [49], [82], THF is most commonly used to dissolve cryptophane-A. Based on our experiments, THF does not completely dissolve cryptophane-A, which is required for

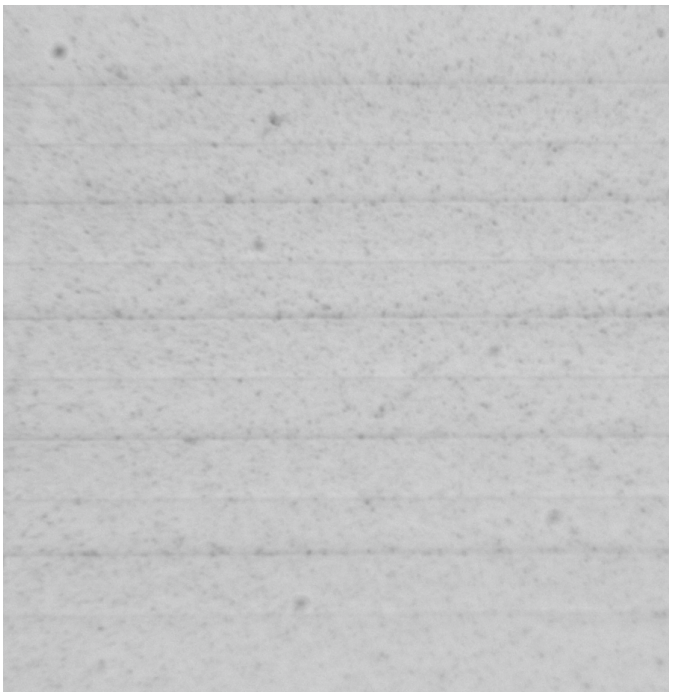

FIGURE 4.2: Displays an example of a layer of PDMS on the sensor chip, with undissolved cryptophane-A, using THF as solvent.

low scattering. Thus, when light is coupled into the waveguide sensor, all light in the sensing arm is scattered away, making the sensor useless for sensing.

To overcome the problem with dissolving cryptophane-A, various available solvents were tested, e.g. dichloromethane (DCM), chloroform, 1,2-dichlorobetzene and 1,1,2,2-tetrachloroethane. The latter, 1,1,2,2-tetrachloroethane dissolved cryptophane-A very well and does not compete with methane, since 1,1,2,2-tetrachloroethane does not fit inside the cryptophane-A cavity.

A new test was made, following the same recipe as above, but with 1,1,2,2-tetrachloroethane as solvent: 0.9 ml of 1,1,2,2-tetrachloroethane to 5 mg of cryptophane-A. Already at the mixing stage, it was apparent that 1,1,2,2-tetrachloroethane completely dissolved cryptophane-A . The mixture was completely transparent. However, when PDMS was added, it did not mix well with the solvent. Figure 4.3 shows the behaviour of the mixture before and after curing. Before curing, the PDMS and the solvent does not mix well. The mixture displays structures of droplets as if the solvent and the polymer were oil and water. Despite efforts to mix the solution, it remained inhomogeneous. After curing, a rainbow-pattern appears and the light is scattered away in the sensing arm. The conclusion is that the solvent 1,1,2,2-tetrachloroethane is not compatible with the PDMS polymer.

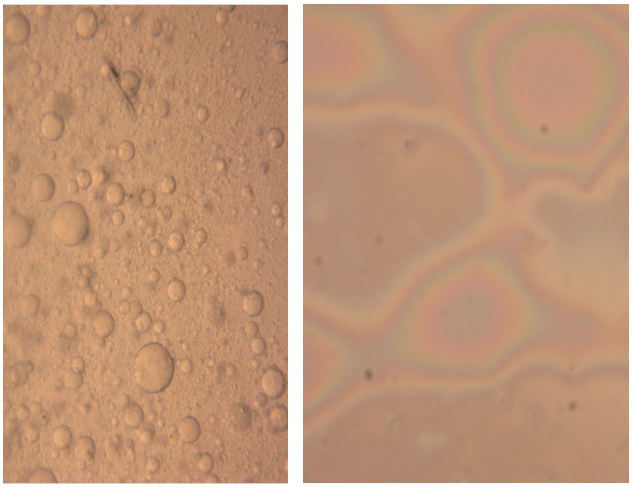

FIGURE 4.3: Displays an example of 1,1,2,2-tetrachloroethane mixed with PDMS, uncured solution (left) and cured (right) PDMS.

4.2.2 Styrene Acrylonitrile

Styrene Acrylonitrile (SAN) is a copolymer consisting of 70% styrene and 30% acrylonitrile by weight. SAN is not as elastic as PDMS, and cures to a brittle and transparent layer. It has a higher refractive index of 1.56 and thus gives a higher sensitivity compared to PDMS (see section 3.2). Methane sensing using SAN as a host-polymer for cryptophanes has been reported in[1, 51]. The polymer should therefore be open to diffusion of methane.

In this trial, 45 mg of SAN pellets and 5 mg of cryptophane-A was dissolved in 0.9 ml of 1,1,2,2-tetrachloroethane. The mixture was completely clear and was deposited onto the chip with the same procedure as for PDMS. Figure 4.4 shows an example of the sensitive layer when using SAN and 1,1,2,2-tetrachloroethane as solvent. It shows that, unlike previous trials, 1,1,2,2-tetrachloroethane completely dissolves cryptophane-A and is compatible with the SAN polymer. When light is coupled into the waveguide sensor, light in the waveguide wasn't scattered away, thus enabling the sensor to measure methane. The thickness of the methane sensitive layer was measured with a mechanical profiler (KLA-Tencor P-6) and was estimated to 200 nm on the silica-coated surface and 1200 nm inside the sensing window, see **paper 3**.

A second sensor was made to investigate the dependency of the sensitivity with respect to the concentration of cryptophane-A in the SAN polymer. In the previous trial, a ratio of cryptophane-A to SAN of 1:9 was used. For the second sensor, a sensitive-layer with a ratio of 1:26 was prepared using the same procedure.

To study the enhancement of methane detection using cryptophane-A, a third sensor was produced in the same manner as the first two sensors, but without cryptophane-A. This allowed us to study how the host-polymer, by itself, reacts to methane.

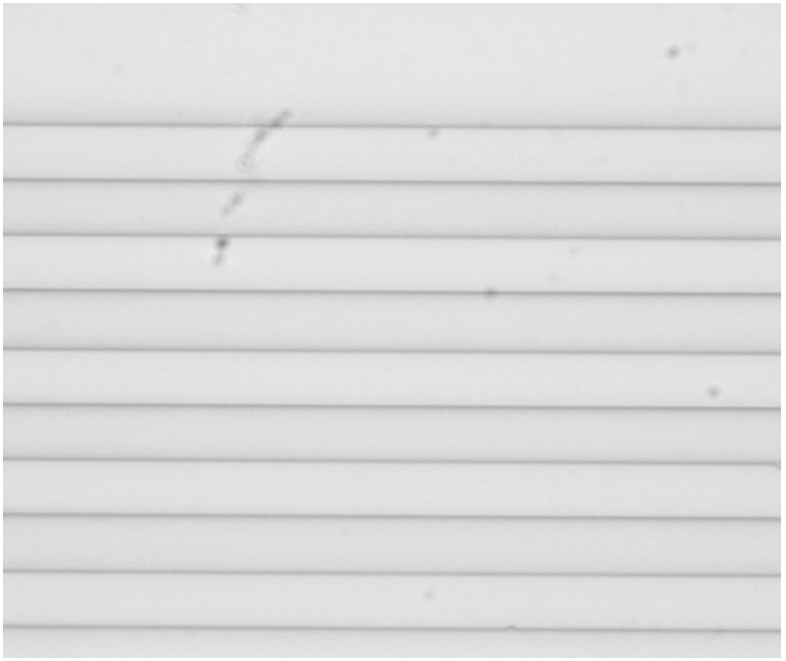

FIGURE 4.4: Displays an example of a layer of SAN on the sensor chip, with cryptophane-A dissolved using 1,1,2,2-tetrachloroethane.

Since the polymer SAN is brittle in behaviour and does not have the "sticky" elastic quality of the PDMS, the polymer showed to have poor adhesion with the surface of the waveguide. In the laboratory (not shown here), the layer could easily be pealed off after being cured on a glass-plate. In the first test, a methane reaction was obtained, but the output signal oscillated randomly. This was not reproducible. In our second attempt, no methane reaction was obtained. A new chip was made with the same recipe, but no reaction to methane was seen. In our first attempt, it is possible that the polymer layer was partially in contact with the waveguide surface, but then detached during the measurement. To conclude, the polymer was not properly attached to the waveguide.

To improve the adhesion between SAN polymer and the waveguide, the surface of the chip was silanized using 3-aminopropyl-riethoxysilane (APTES). The silanization process is described in section 3.4. The silanization step improved the adhesion and measurement of methane was achieved with the methane sensitive layer (without any oscillations).

The surface of the SAN-layer was clearly effected when exposed to water, leaving fractures along the surface, as seen in Figure 4.5. Experiments showed that SAN does not dissolve in water, even after being submerged for several days.

A possible explanation of the fractures could be that SAN partially absorbs water, causing it to swell, and thus introduces stress in the polymer layer. Because of SAN's brittle mechanical nature, tensions along the sensing windows due to swelling can cause the polymer to eventually crack when being exposed to water. The SAN layer can also

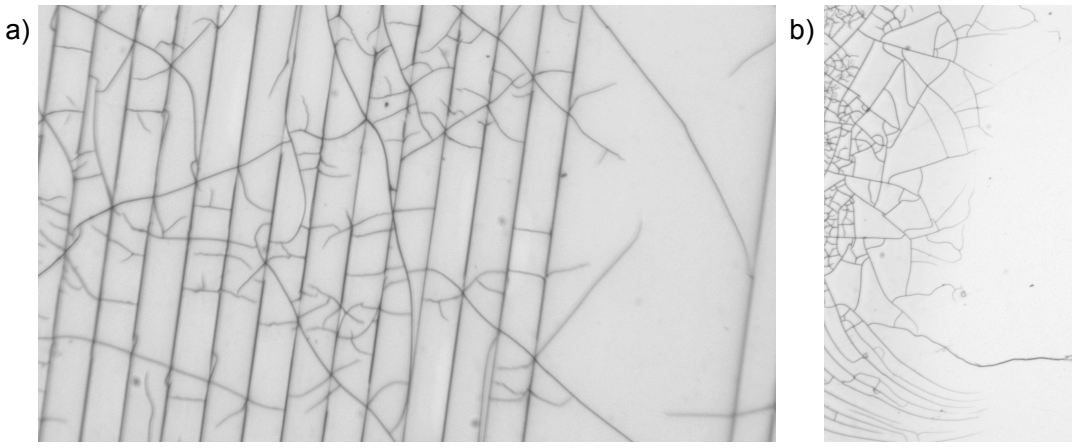

FIGURE 4.5: Photos of SAN after direct exposure to water, a) over the sensing windows and b) at the end of the microfluidic chamber, showing the exposed and unexposed areas.

be ripped away by the flow of the water or in the process of removal of the microfluidic PDMS chamber, which was observed a few times.

Stress in the film can also be introduced by shrinkage during evaporation of the solvent. An effort was made to reduce the stress by thermal annealing after deposition, instead of letting the substrate cure over-night in atmospheric conditions. The oven temperature was slowly increased, in an effort to avoid stress introduced by thermal shock. However, this did not solve the problem.

To circumvent the fracturing and protect the SAN surface from being exposed to water, an additional (pure) PDMS layer was deposited on top of the methane sensitive SAN-layer (doped with cryptophane-A). The idea is that PDMS will keep the water away, while methane diffuses through to the SAN-layer. The additional coating of PDMS was deposited onto the sensor using spin-coating at 4500 rpm for 2 min. The layer of PDMS and SAN combined was measured, with KLA-Tencor P-6 stylus profiler, to have a thickness of about 8 μm on the silica surface. As the thickness of SAN alone was 200-300 nm (paper 3), the thickness of the PDMS-layer is estimated to be 7.7-7.8 μm thick.

Chapter 5

Methane sensing

An optical waveguide Mach-Zehnder interferometer has been developed and coated with a methane sensitive layer as described earlier. In this chapter, we begin with describing the experimental setup used for measuring methane gas and methane dissolved in water. The results from measuring methane gas was published in **paper 3** and performed together with my colleagues Firehun T. Dullo and Jana Jàgerskà. The final section presents the results from measurements of dissolved methane.

5.1 Experimental setup

The experimental setup for measuring dissolved methane consists of three integral parts, as seen in Fig. 5.1: the optical setup, the mechanical setup with temperature stabilisation and the microfluidic delivery system. The latter can be connected either to a gas supply system (for gas measurements) or a mixing system for methane dissolved in water.

The laser, as seen in Fig. 5.1a), is a compact diode-pumped solid-state laser at 785 nm with maximum power of 108 mW. The laser beam was coupled into the input facet of the waveguide chips, through an objective lens (25x, NA = 0.65, NIR, Thorlabs) fixed on a 3D translation stage. In the input path, the polarization of the light was rotated with a half-wave plate to TM-polarization for optimal sensitivity, see chapter 3.

A set of beam-expanding lenses was placed in front of the input objective lens to fill the aperture of the objective lens for optimised coupling. The light emerging out from the waveguide was collected with a second objective lens (10x, NA = 0.3, NIR, Thorlabs) and directed to a photodiode (SM1PD1A, Thorlabs). A custom-written Labview program records the interferometric signal from the photodiode at a rate of 2 Hz. The program also controls the temperature and regulates the gas flow. The sensor is mounted on a temperature-stabilised stage equipped with a Peltier element to reduce phase shift due to external temperature variations.

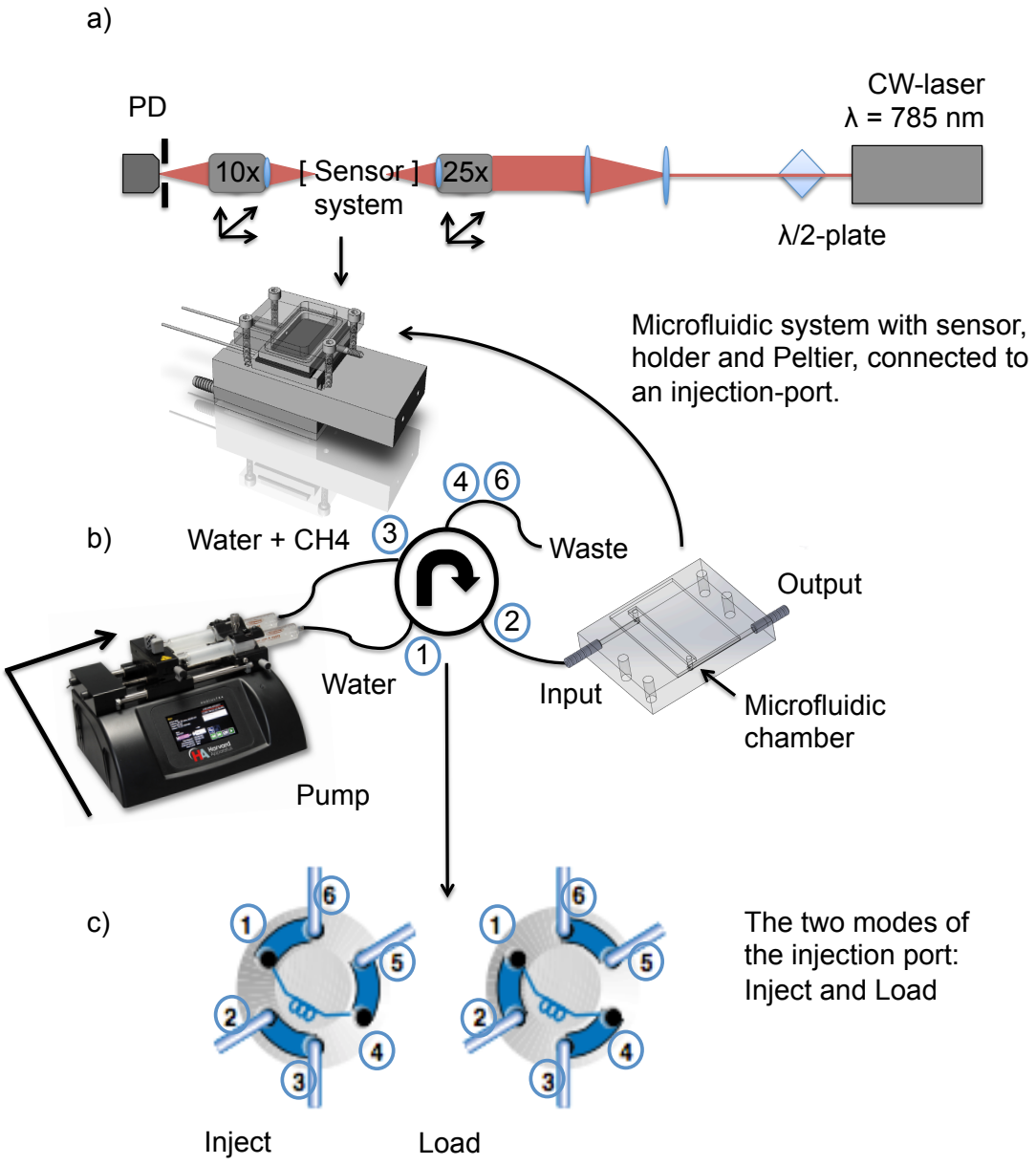

FIGURE 5.1: Shows the experimental setup for dissolved measurements with a) optical setup b) methane/water injection system and c) the injection port. The fluidic system in b) shows the connection from the syringe pump to the chamber lid (pressed down on the chip). The concentration of dissolved methane is directly measured with a reference sensor from the methane mixing reservoir (not seen here). A sample is extracted with a syringe and added to the pump system. The 2-modes of the injection-port system in c) allows continuous flow of either water or dissolved methane.

To deliver the measurand (water or gas) to the surface of the waveguide sensor, a microfluidic lid is placed on the surface of the chip. A microfluidic channel (made of PDMS) is attached to the transparent lid made of polystyrene. The lid was fixed with nylon screws to the chip holder (made of aluminium). The microfluidic channels were made with a mold of aluminium. A channel with dimensions 32 mm x 6 mm x 1 mm was made to cover a group of sensors on the chip, giving an enclosed sample volume of 0.192 ml. The mold is filled with PDMS to create the channel structure. The PDMS liquid is first put in vacuum to remove excess bubbles, created when mixing PDMS. Once the bubbles were removed, the PDMS was cured at 100°C. After pealing the PDMS structure out of the mold, it was fixed to the lid to create the microfluidic cell.

For dissolved methane measurements, gas with 4% methane in nitrogen was bubbled in a water reservoir. The concentration of dissolved methane was continuously measured with a reference sensor throughout the measurements. The reference sensor was provided by Franatech (Methane field sensor; T90 = 15 min, LOD = 2 ppmv) and uses tunable diode laser spectroscopy (TDLAS) to measure the concentration of methane gas). To measure methane in water, the reference sensor extracts the gas from the water using silicon membranes. Franatech provides a formula, based on Henry's law, to convert the methane gas concentration to the concentration of dissolved methane in μmol/L. According to Henry's law, at a constant temperature, the amount of methane gas that dissolves in water is directly proportional to the partial pressure of methane in equilibrium with water. The methane reservoir consisted of a bucket with water, connected with input and output tubes to the reference sensor and an output tube for our system. To create a "closed" system, the reservoir was wrapped in a transparent plastic bag. A thermometer was placed in the water to keep track of the temperature during measurements.

Water samples were extracted from the reservoir with a 60 ml syringe and placed together with a second syringe with pure water. The two syringes were pushed continuously with a syringe pump (Harvard PHD Ultra 2000), giving a flow-rate of 0.2 ml/min. Water and the dissolved methane was pumped to the microfluidic sensor system through transparent Tygon tubings (inner-diameter 1.5 mm) connected via an injection-port system modified for continuous feed of sample or water. Figure 5.1c) shows the two standard configurations of the injection-port for loading and injection. Pure water from the pump system was connected to port 1 and sample from the pump system was connected to port 3. Port 2 was connected to the sensor system. Port 5 and the loop, between port 1 and 4, were not in use. Ports 6 and 4 are outputs for water and sample to waste. When the injection-port system is in mode "load", the pure water is pumped directly to the sensor system and the sample water is by-passed to waist. When the injection-port system is placed in mode "inject", the sample is transported to the sensor system and the pure water is by-passed to waste. In the inject-mode, pure water is replaced with

dissolved methane, causing interference at the output of the sensor. When the mode is switched to "load", pure water is pumped back into the system, giving rise to a second set of interference fringes.

For gas measurements as discussed in section 5.2, the microfluidic system was directly by-passed to a gas delivery system, consisting of two mass-flow controllers (MFCs, max: 100 ml/min, flow used: 10 ml/min, EL-flow, Bronkhorst). The MFCs were connected to a pre-mixed bottle of methane in nitrogen (2-4%) and a bottle of pure nitrogen, respectively. The gas system is shown in paper 3.

5.2 Measurement of methane gas

In chapter 4, we discussed the deposition of SAN as host-layer with cryptophane-A on three different sensors with different ratios of cryptophane to polymer. Sensor 1 had a ratio of 1:9, sensor 2 had 1:28 and sensor 3 contained pure SAN-polymer. It should be noted that PDMS was also considered as host-layer in chapter 4, but it was not compatible with the solvent that dissolved cryptophane-A. All three sensors were used for measuring methane gas, with the experimental setup described in the previous section. Sensor 3 was tested and characterised for three different sensing lengths, 1, 2 and 3 cm. A summary of the sensitivities and their respective limit of detection (LOD) is displayed in table 5.1. Higher concentration of cryptophane-A increased the sensitivity and consequently decrease LOD. Similarly, increasing the sensing length also increases the sensitivity and decreased LOD. The experiments and the results are presented and discussed in **paper 3**.

TABLE 5.1: Sensitivities of the respective sensors and their detection limits for methane gas. The standard deviation has been estimated from an Allen plot to $\sigma_y = 0.00165$ rad, as shown in paper 3.

Sensor	crypt-A:SAN	Sensing length	Sensitivity (rad/ppm)	LOD (ppm)
1	1:9	1 cm	0.96×10^{-4}	48
1	1:9	2 cm	1.77×10^{-4}	26
1	1:9	3 cm	2.67×10^{-4}	17
2	1:28	3 cm	0.94×10^{-4}	50
3	0:1	3 cm	0.16×10^{-4}	289

5.3 Measurement of methane dissolved in water

Methane dissolved in water was measured using the experimental setup described in section 5.1. The sensor was covered with the most sensitive layer (Cryptophane-A:SAN of 1:9) from the previous measurements of methane gas. A second coating of PDMS with a thickness of about 7 μm was added to protect the SAN surface from being exposed to water, as discussed in section 4.3.

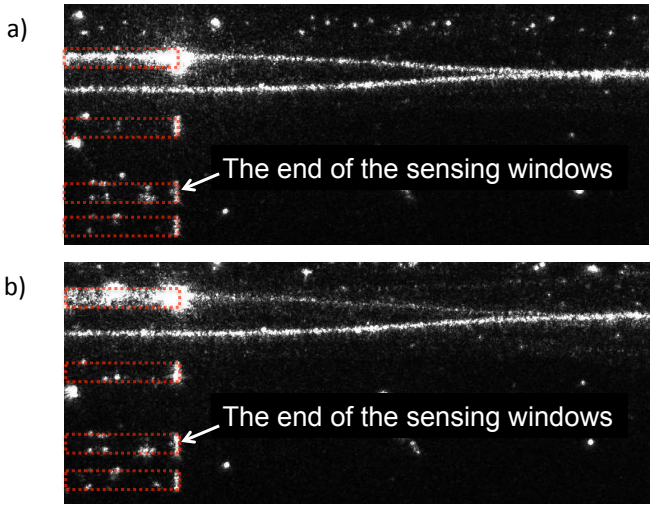

FIGURE 5.2: Shows the loss of intensity in the sensing arm with time after exposure to water. The images show the coupling after the second y-junction, a) before and b) as water is entering the chamber. The methane sensitive layer has been coated with PDMS.

Various concentrations were extracted with a syringe from the methane mixing reservoir and injected into the microfluidic system, as described in section 5.1. The concentration of methane in the reservoir was measured continuously with the reference sensor (Franatech). During the first measurement with the sensor (labelled 1A), it was discovered that the fringe amplitude decreased with time. This problem is described and discussed before returning to the measurement results. The intensity in the two waveguides, at the end of the sensing window, is shown in Fig. 5.2. The light in the two waveguides is equally strong before water enters the microfluidic chamber, in Fig. 5.2a). In Fig. 5.2b), water has entered into the chamber and the intensity in the sensing arm is starting to decrease and continued to decrease with time. This effect could also be seen in the measurements as the visibility of the interference fringes decreased with time, as seen in Fig. 5.3.

By moving the microscope along the sensing window, small structures or "bubbles" (1-25 μm in size) were observed randomly in the polymer layers, as shown in Fig. 5.4. Each structure is a source of scattering, and the intensity in the sensing arm is lost. In microfluidic systems, it is a common problem to introduce small air bubbles in the

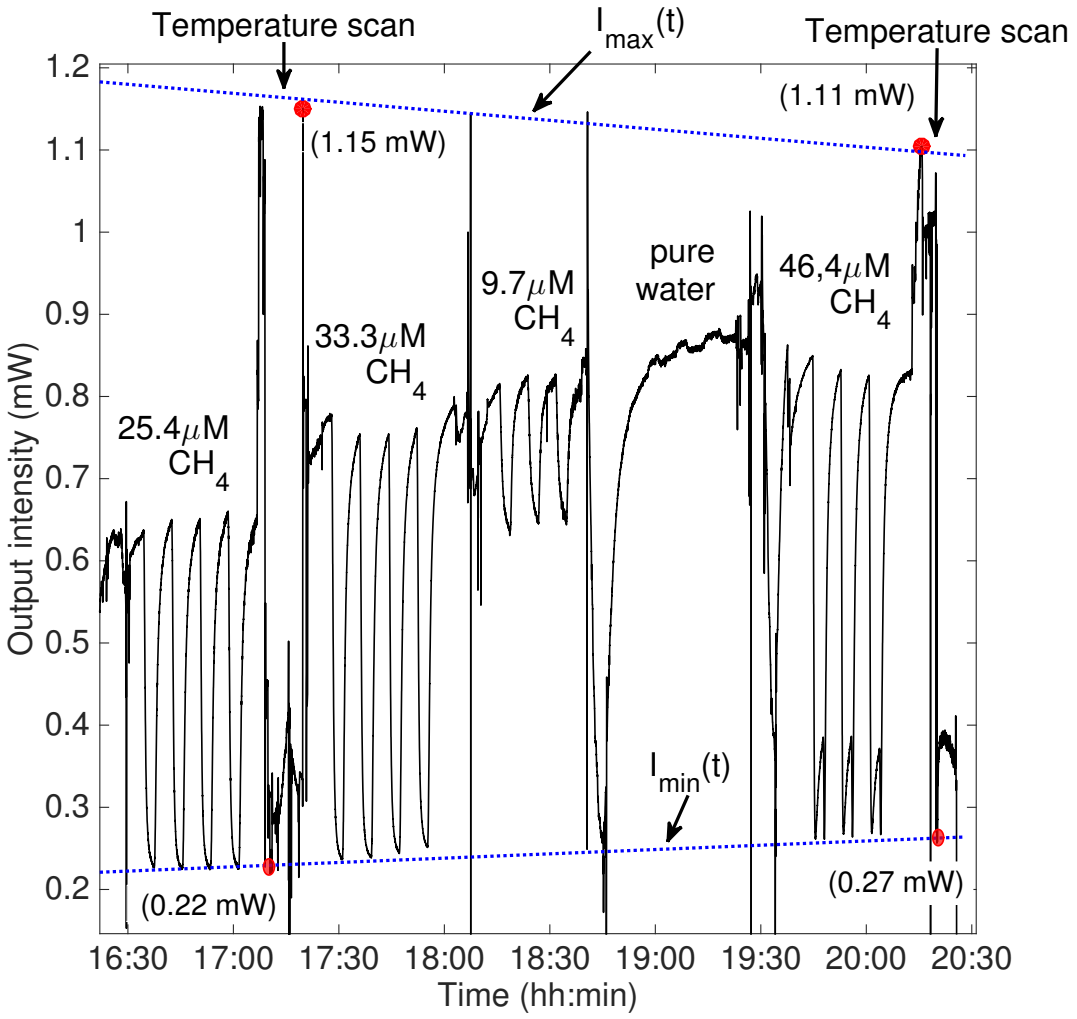

FIGURE 5.3: Shows the output intensity when introducing methane in water to sensor 1A. Each measurement of concentration was repeated three to four times.

system from the syringe or small openings in the tubing connections. However, these are air bubbles in the chamber and can be seen with the naked eye. The "bubble" structure that appeared during the exposure to water, appears to be formed beneath the layer of the sensitive polymer. Since intensity is lost, the structure must be within the range of the evanescent field. The water pump was turned off and water removed slowly from the microfluidic chamber by flushing the system with N_2 gas. The "bubble" structures seemed to disappear and the light in the sensing window was eventually restored back to its original strength (within 10-15 min). When exposed to water again, the structures eventually disappear and measurements were done (see later paragraph). The appearance and number of bubbles varied from one interferometer to another on the same chip, as these seem to appear randomly.

In the first tests with PDMS as sensing layer before changing to SAN, PDMS was directly exposed to water. With PDMS deposited directly on the waveguide, the bubble

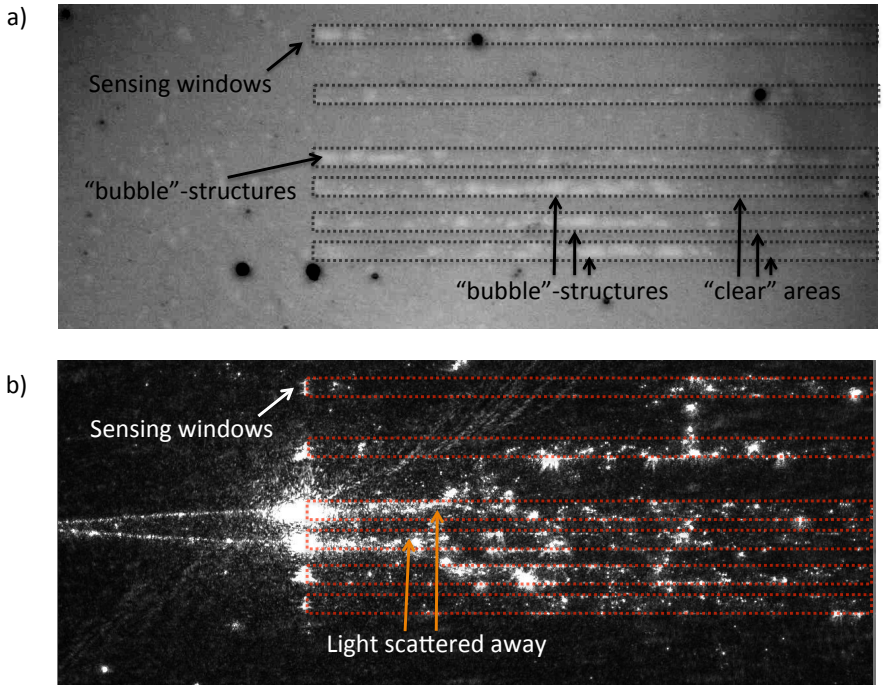

FIGURE 5.4: Shows an example of the "bubble"-structures formed in the beginning of the sensing window (seen as brighter areas) after exposure to water. a) shows the bright-field image of the surface after being exposed to water and laser off. b) shows the dark-field image of the same location with the laser on. Light is scattered away due to the "bubble"-structure.

structures were not observed. Thus, the "bubbles" appearing for SAN is probably due to a silanization problem or water diffuses through PDMS, exposing SAN to water. A possible reason, based on discussions with Jørn Hansen at the Department of Chemistry (UiT), is that ammonia (NH_3) is formed on the waveguide surface of silicon nitride when exposed to water. Since ammonia is an acid, it can destroy the connection between silane and the silicon nitride surface, thus forming bubbles filled with gas or water. Another possibility is that the silanization of the surface is not uniform. However, these structures were not observed for the methane gas sensing, despite using the same method for silanization and deposition. Another explanation, is that water has penetrated through the PDMS layer by diffusion, giving cracks as when SAN was directly exposed to water.

After exposing the chip to water, a Mach-Zehnder was chosen with minimal effects of the bubbles and measurements were done using sensor 1A. The measured intensity is shown in Fig. 5.3 and transformed to phase using Eq. 2.7. For further details on phase unwrapping, see Fig. 4 and Eq. 2 of paper 3. Figure 5.5 shows the phase change as function of different concentrations of dissolved methane injected to sensor 1A. First, the two syringes were filled with water, giving minimal phase change. The

small bump is probably due to a difference in temperature between the two syringes. For the other measurements, one syringe was filled with water while the other syringe was filled with increasing concentrations of dissolved methane. Concentration 9.7 ± 0.07 μM was obtained by filling 1/4 of the volume of the syringe with a concentration of 38.7 ± 0.23 μM dissolved methane and the remaining 3/4 with water. The other concentrations (25.4 ± 0.4 μM , 33.3 ± 0.23 μM and 46.4 ± 0.003 μM) were extracted directly from the methane reservoir at certain times.The concentration was measured with the reference sensor from the reservoir, and the concentration was taken as an average with ± 1 min from the time of extraction. The phase increases linearly with concentration. In addition, Fig. 5.3 shows that the results were reproducible. The five measurements, each repeated three to four times, took three and a half hour to complete. During this time, the amplitude changed 90 μW and it changed 0.29 mW for the whole day.

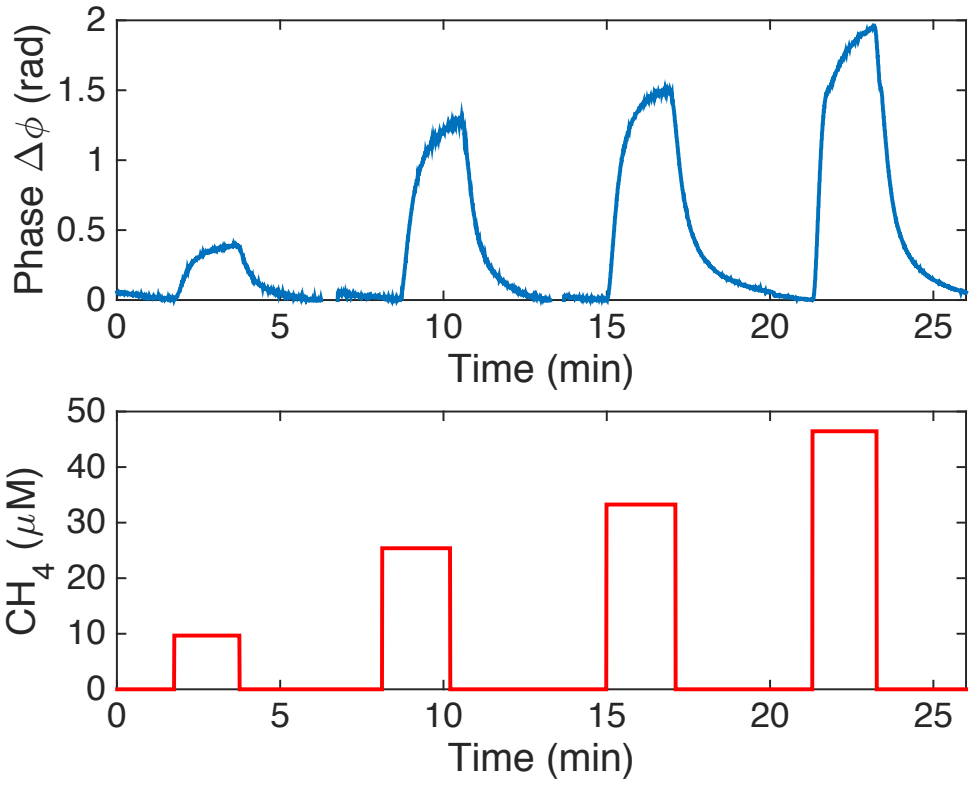

FIGURE 5.5: Shows the measured phase with applied concentration of methane for sensor 1A, with waveguide width 2 μm and sensing length of 2 cm. The top of 46.4 μM has been unwrapped since the phase change exceeds $\pi/2$.

A second measurement series was made with the same sensor, but with a new methane sensing layer. The bubble structures were also seen on this chip, but an interferometer was chosen with few bubble structures and with visible intensity propagating

in the waveguide after the sensing window. The measurement was also done quickly (within 30 min) to avoid any decay of the amplitude during the measurement.

Figure 5.6 shows the measured phase change, $\Delta\phi$, plotted as a function of the concentration of dissolved methane for sensor 1. Measurements were made on two different days (labelled sensor 1A and 1B in the figure), each with a new methane sensitive layer with a Cryptophane-A:SAN ratio of 1:9. Sensor 1B was measured for lower concentrations. The response of the interferometer shows a linear dependence, with the slope defined as the sensitivity, S.

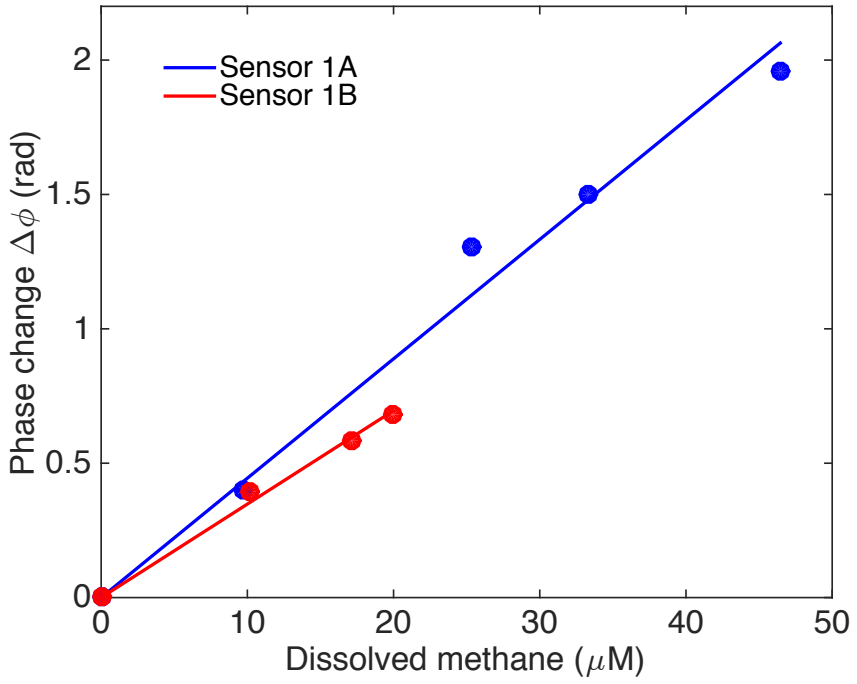

FIGURE 5.6: Shows the sensitivity of the device for dissolved methane. The sensing length was 2 cm, the waveguide width 2μm and cryptophane-A:SAN ratio1:9. Sensor 1A (blue) and Sensor 1B (red) are made with the same recipe described in chapter 4. Sensor 1B was used to measure lower concentrations of dissolved methane than sensor 1A.

The limit of detection (LOD, 99% confidence level) was estimated according to the procedure suggested by the American Chemical Society [83, 84]:

$$LOD = \frac{2.821\sigma_y}{S} \tag{5.1}$$

where S is the sensitivity and σ_y is the standard deviation from the measurement.

To find the standard deviation, the Allan-deviation was estimated with the program Igor. Figure 5.7 shows the Allan deviation of the measured data as a function of the integration time. The line marked as 2 is the Allan deviation with drift, while the line marked as 1 is without drift (with confidence intervals). From the Allan-plots

the standard deviation for sensor 1A was estimated to $\sigma_y = 0.00121$ radians (35 second integration time) and for sensor 1B, $\sigma_y = 0.00061$ radians for 1.6 second integration time, as shown in Fig.5.7. The sensitivities and the limits of detection (LOD) are displayed in table 5.2. For an interferometer with 2 cm long sensing window, a sensitivity of 4.44×10^{-2} rad/ μM (sensor 1A) and 3.48×10^{-2} rad/ μM (sensor 1B) was obtained. The best LOD obtained with the sensor in its current state is thus 49 nM with a sensing length of 2 cm.

TABLE 5.2: Sensitivities of the two sensors and their detection limits for methane dissolved in water. The standard deviation has been estimated from an Allen plot. For sensor 1A, 35 second integration time was used and for sensor 1B, 1.6 second integration time.

Sensor	Crypt-A:SAN	Sensing length	Sensitivity (rad/nM)	σ_y (rad)	LOD (nM)
1A	1:9	2 cm	4.44×10^{-2}	0.00121	76.84
1B	1:9	2 cm	3.48×10^{-2}	0.00061	49.47

The sensitivity for a sensing length of 3 cm was not measured because the bubble structures, mentioned earlier, did not give a good output after the sensing window. The microfluidic chamber is also about 3 cm, which made it difficult to check the intensity after the sensing window.

The limit of detection can be compared to the methane concentrations measured with an SPR sensor in the Baltic sea, ranging from 5 nM to a few hundred nanomolar [2]. In the field, the SPR sensor showed a sensitivity of 6 to 7 x 10^{-7} RIU/nM and the detection limit varied from 3 to 7 nM. Although our sensor has not reached a detection limits as low as 3 nM, it is not far from this limit and there is room for improvements using a different polymer and a longer sensing length.

The stability of the sensor can be improved by solving the described issues with the SAN polymer. Since the "bubbles" introduce scattering over time, the signal is lost and render the sensor useless. It was apparent that with increasing loss in the sensing window, the sensitivity of the sensor decreased. Although the sensitivity was identical for the sensor at two different times, the repeatability is not satisfactory and it is possible that the sensitivity will decrease with time also for a "good" sensor with a few bubbles. This should be investigated further.

Finding a polymer that is compatible with the solvent used for dissolving Cryptophane-A, is water resistant, transparent and let methane diffuse though could potentially improve the detection limit of the sensor and give reliable measurements. Possible candidates are perfluoropolyethers (PFPEs) and perfluoropolyethers (PFPE) that is a

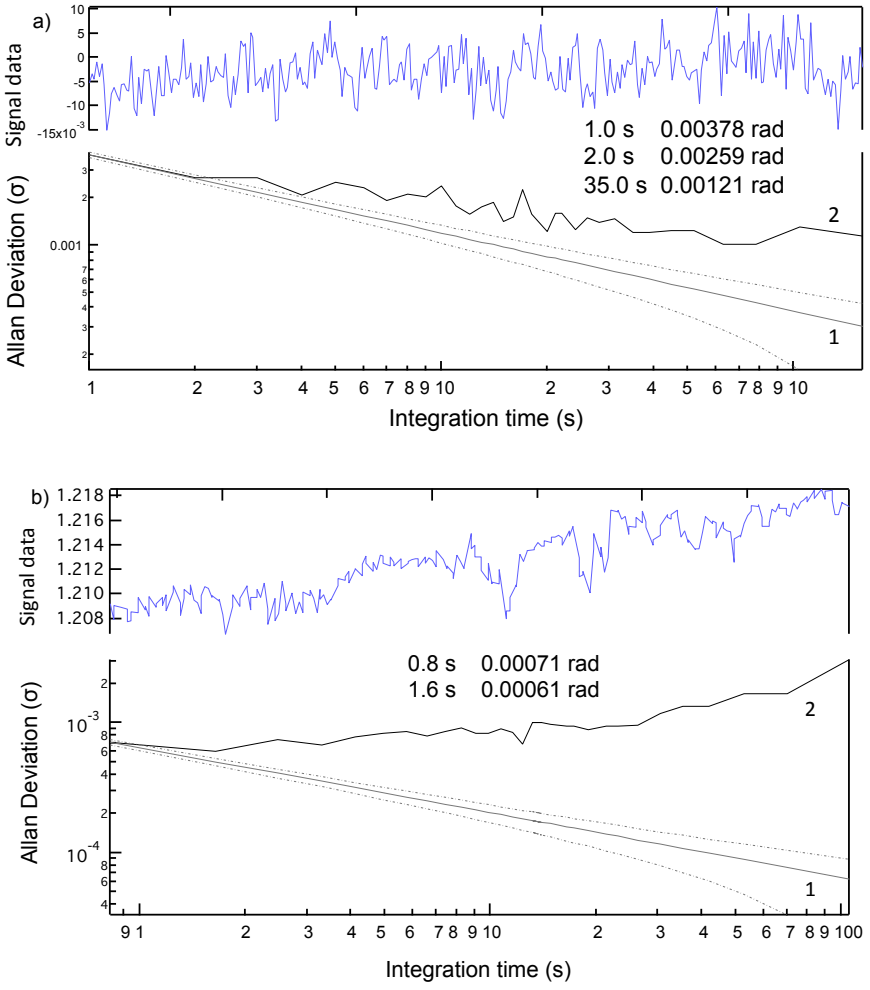

FIGURE 5.7: Shows the Allan deviation for the output signal of a) sensor A and b) sensor B as function of integration time, with drift (2) and excluding drift (1).

solvent-resistant elastomer [85, 86]. However, these would have to be tested with the solvent 1,1,2,2-tetrachloroethane.

Chapter 6

Included publications

6.1 Paper 1: Estimation of Propagation Losses for Narrow Strip and Rib Waveguides.

Published in Photonics Technology Letters, IEEE, July, 2014.

Authors: Susan M. Lindecrantz and Olav Gaute Hellesø

Contribution notes: Propagation losses for strip and rib waveguides were measured and simulated by Susan M. Lindecrantz. The MATLAB program for estimating the propagation losses from scattered light using a CCD camera was written by Susan Lindecrantz and Pål Løvhaugen. The article was written together by Susan Lindecrantz and Olav Gaute Hellesø.

Estimation of Propagation Losses for Narrow Strip and Rib Waveguides

Susan M. Lindecrantz, *Member, IEEE*, and Olav Gaute Hellesø, *Member, IEEE*

***Abstract*— The dependence of propagation losses on waveguide width and polarization is measured for strip and rib waveguides made of tantalum pentoxide. For strip waveguides, the propagation losses are found to increase rapidly for widths <3 μm. The losses were significantly smaller for rib than for strip waveguides, as expected. A method is developed for estimating the dependence of propagation losses on waveguide width. The method is based on approximating sidewall imperfections with an area with complex refractive index in a 2D model and showed a good agreement with the measured dependence on waveguide width. The method is also used to predict that propagation losses will decrease rapidly for rib heights less than 20 nm for TM-polarization.**

***Index Terms*— Strip waveguide, rib waveguide, propagation loss, sidewall roughness, scattering loss, tantalum pentoxide.**

I. Introduction

IN ORDER to tightly confine light in optical waveguides, the refractive index of the core must be high and the cross-section of the waveguide must be small. At the same time, propagation losses must be kept low to allow complex optical circuits. The main sources of propagation loss for a dielectric straight waveguide are absorption within the materials and radiation losses from imperfections in the materials and on the sidewalls [1]. As the refractive index is increased and the cross-section reduced, the imperfections of the sidewalls become the dominating source of propagation losses. In this letter, the influence of the height of the sidewalls (i.e. rib height) and the waveguide width on propagation losses is studied experimentally and simulated.

Propagation losses are of general importance for integrated optics. The wavelength, waveguide structure and materials used in this letter are particularly relevant for evanescent field sensors, e.g. based on the Mach-Zehnder waveguide interferometer. Two commonly used materials for waveguide sensors and biosensors are Si_3N_4 [2], [3] and Ta_2O_5 [4]. These materials are transparent in the visible and near infrared, and have a refractive index of 2 and 2.1, respectively. For the experimental work, we have chosen Ta_2O_5 and the corresponding refractive index is used for the simulations. For evanescent field sensors, the sensitivity increases with the refractive index of the core and with decreasing core thickness [5]–[7]. For the Mach-Zehnder interferometer, it is imperative that the waveguides are single-mode. This can be obtained by reducing the width of the waveguide or by using rib waveguides where the core is only partially etched down on the sides. Shallow rib waveguides with 4 nm rib height, widths of 3-4 μm and 200 nm core thickness have been made with propagation losses as low as 0.15 dB/cm for TE-polarization and 0.30 dB/cm for TM-polarization [8].

Several methods exist to estimate propagation losses from surface roughness, see [9]–[11]. These methods require parameters such as the roughness standard deviation and the autocorrelation length of the sidewall roughness to be known. Surface roughness is usually measured using atomic force microscopy (AFM). For narrow waveguides, the critical parameter is the sidewall roughness, rather than the surface roughness. However, it is a challenge to measure the sidewall roughness for strip waveguides (200 nm high sidewalls) and very difficult for shallow rib waveguides (1-10 nm high sidewalls). Rather than basing the simulations on roughness measurements, we have used a measured propagation loss for a narrow waveguide as a reference to estimate the propagation loss for other waveguide widths. Our method is based on approximating the surface roughness with a small section with complex refractive index in a 2D model. The method is described in the next section and it is tested on strip and rib waveguides.

II. Methods

A. Experimental Methods

Strip and rib waveguides were produced by sputtering a core layer of tantalum pentoxide ($n_{core} = 2.15$) onto a 5 μm silica layer (n = 1.45). The waveguides were defined by photolithography followed by argon ion-beam milling at an angle of 45° to reduce the sidewall roughness. The waveguides were treated with plasma-ashing for 10 minutes to remove remaining photoresist and annealed at 450 °C-600 °C in oxygen in a tube furnace for 2-5 hours [12]. Rib waveguides were made with a core thickness, H, of 170 nm and a slab thickness, h, of 150 nm, see Fig. 1. The strip waveguides had a core thickness, H, of 215 nm and by definition a slab thickness h = 0. These dimensions have been determined using a scanning electron microscope (SEM) and a mechanical profiler (Tencor P6).

The propagation losses were measured for w = 1-10 μm wide strip waveguides and w = 1-5 μm wide rib waveguides. Light from a 785 nm diode laser was coupled into the waveguide using beam expanding lenses and a 40× objective lens. The polarization was rotated with a half-wave plate

Manuscript received March 12, 2014; revised May 2, 2014; accepted July 4, 2014. Date of publication July 9, 2014; date of current version August 15, 2014. This work was supported by the Research Council of Norway.

The authors are with the Department of Physics and Technology, UiT - The Arctic University of Norway, Tromsø 9037, Norway (e-mail: susan.lindecrantz@uit.no; olav.gaute.helleso@uit.no).

Color versions of one or more of the figures in this letter are available online at http://ieeexplore.ieee.org.

Digital Object Identifier 10.1109/LPT.2014.2337055

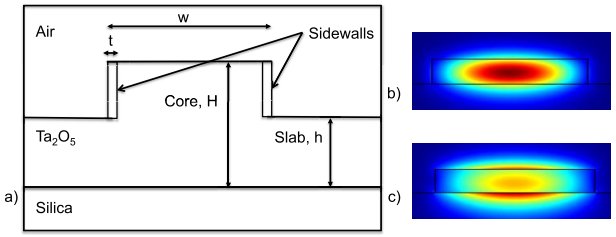

Fig. 1. a) Schematic diagram of the waveguide cross-section used in Comsol simulations (not to scale). Examples of the fundamental mode for a strip waveguide for b) TE- and c) TM-polarization.

to obtain TE- or TM-polarization. A second 40× objective lens was used to couple light out from the waveguide into a photodetector. The photodetector was used to ensure that optimal and stable coupling was obtained during the measurements.

The propagation losses were measured by taking images of light scattered from the waveguide with a microscope on a translation stage. The microscope was moved along the waveguide and images of the scattered light captured. This is a non-destructive method independent of input coupling and suitable for measurement of relatively high propagation losses (dB/cm-range) [1], [13], [14]. The images of scattered light were captured with an objective lens with a relatively large magnification, 50×, and NA = 0.8, in order to avoid interference between scattering points and to limit the area observed. The exposure time for the microscope's CCD camera was adjusted to the maximum time not giving saturated points in the image. The images were processed with a Matlab-program. For each image, the pixels were summed along the waveguide, giving an approximately Gaussian profile across the waveguide. Pixels within the FWHM-width of the profile were subsequently summed along and across the waveguide, giving a relative intensity for the image. This value was corrected for the exposure time, i.e. by dividing by the exposure time. The first image, taken near the input, was used as a reference and given the value $I(0) = 0$ dB. Images captured further from the input thus gave intensities $I(z)$, with intensity in dB and distance z measured from the position of the reference image.

Fig. 2 shows an example of the measured scattering as function of the propagation distance. The images are taken of scattering from randomly distributed imperfections, mostly on the waveguide surface. The measured intensities will thus have a statistical variation. A straight line was fitted to the data with the least-squares method. The slope was used to find the propagation loss and the standard deviation of the slope was used to characterize the statistical variation. For the case in Fig. 2, this gave a propagation loss of 6.7 ± 1.6 dB/cm.

For relatively wide waveguides, i.e. 5-10 μm for strip waveguides and 3-5 μm for rib waveguides, the propagation losses do not depend on width as seen in Fig. 3. Thus, propagation losses for these wide waveguides are less dependent on scattering from the sidewalls and mostly due to absorption and scattering from imperfections within the material. The average propagation loss is 1.4 dB/cm and 1.3 dB/cm for TE-polarization and 1.1 dB/cm and 1.5 dB/cm for

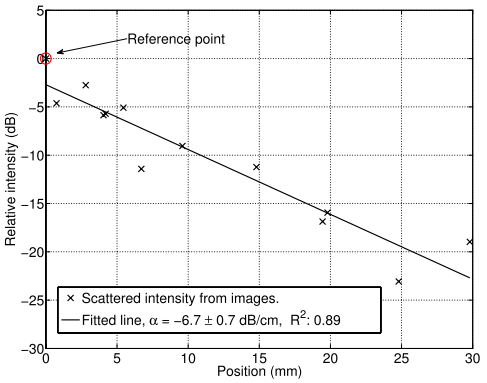

Fig. 2. Relative scattering intensity versus position for strip waveguide of width 1.5 μm and TE-polarization.

TM-polarization for wide strip and rib waveguides, respectively (see Fig. 3 and result-section). This average loss was subtracted from the measured values for all waveguide widths before simulations. The remaining loss, α_{dB}, is taken to be due to scattering from the sidewalls.

B. Simulation of Propagation Losses

Comsol Multiphysics was used to find the complex effective refractive index of waveguides. The sidewalls are represented in the model by an area of width t on each side of the core as shown in Fig. 1. Losses due to scattering from the sidewalls are included in the model by adding an imaginary part to the refractive index for this area. A width $t = 10$ nm was used for the simulations. It was tested that the results where independent of the width t by doing simulations with widths 5 and 20 nm for some cases.

To find the relationship between simulated complex effective refractive index and measured propagation loss, the attenuation coefficient, α_{dB} (in dB/cm), can be written as:

$$\alpha_{dB} = -10\log\left(P(z)/P_0\right) \tag{1}$$

where P_0 is the reference intensity and $P(z)$ is the intensity at distance z from the reference point. The power $P(z)$ is related to the effective refractive index n_{eff} by:

$$P(z) = |U(z)|^2 = |A_0\exp(-jkz)|^2 = P_0\exp(\frac{-4\pi}{\lambda_0}n_{im}z) \tag{2}$$

where $U(z)$ is the time-independent complex wavefunction, A_0 is the complex envelope constant, k is the wavevector and λ_0 is the wavelength (785 nm). A propagation loss α_{dB} thus corresponds to an imaginary part n_{im} of the effective refractive index with z = 0.01 m:

$$n_{im} = -\frac{\lambda_0\alpha_{dB}}{40z\pi\,loge} \tag{3}$$

Simulations in COMSOL are done to iteratively find the complex refractive index of the sidewalls, $n_{core} + jn_w$, that gave a complex effective refractive index (for the mode) equal to $n_{re} + jn_{im}$. Here n_{re} is the real part of the effective refractive index and n_{im} corresponds to the measured loss using Eq. 3. The complex value found, $n_{core} + jn_w$, is subsequently used to find the complex effective refractive index,

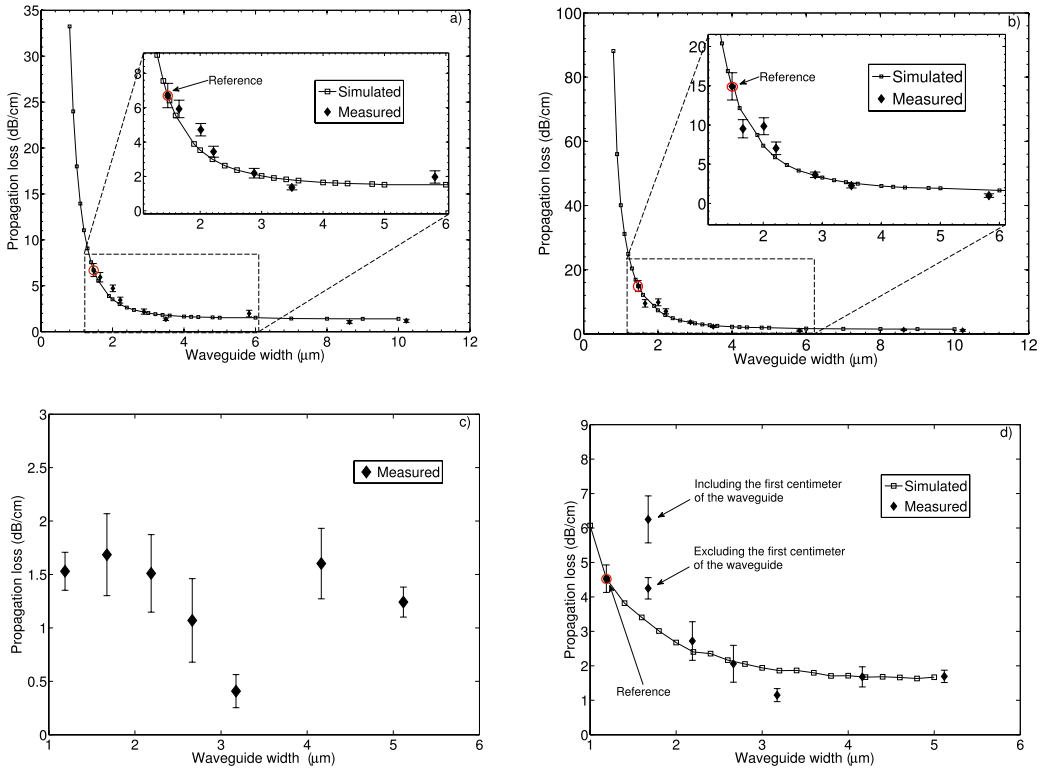

Fig. 3. Propagation losses as function of waveguide width for strip waveguides, for a) TE-polarization and b) TM-polarization. Propagation losses as function of waveguide width for rib waveguides, for c) TE-polarization and d) TM-polarization.

and thus the loss, for other waveguide widths. The selected reference waveguides had a width of 1.5 μm for strip waveguides and 1.2 μm for rib waveguides. The thickness of the waveguides simulated was the same as for the waveguides measured. Care was taken to avoid interference from higher order TE- solutions when simulating TM-polarization. Fig. 1(b) and 1(c) shows examples of simulated fundamental modes for TE- and TM-polarization ($\lambda = 785$ nm).

Our technique assumes that the random and spatially distributed surface roughness can be approximated with a thin layer of constant complex refractive index. Furthermore, the simulation only considers the fundamental mode. For multimode waveguides, higher order modes will have a different spatial distribution and thus be influence differently by the surface roughness compared to the fundamental mode.

III. Results and Discussion

Fig. 3(a) and 3(b) shows the measured and simulated propagation losses for strip waveguides for TE- and TM-polarization. The propagation losses increase very fast as the width decreases below 3 μm. For wider waveguides than 3 μm, the propagation losses show insignificant dependency on the width. The measurement uncertainty is small for these low losses, while for the larger losses of narrow waveguides, the measurement uncertainty also becomes larger. This is most likely due to the random nature of the imperfections, with some sections of the waveguide having low losses and others having large losses. The losses are considerably larger for TM-polarization than for TE-polarization. The simulated propagation losses show good overlap with the measurements. In particular, the simulations predict well the increase in propagation losses around 3μm width. An exponential fit to the data would be possible, but requires at least two reference points, whereas our simulation is based on a single reference point. It also gives a more physical approach to the propagation losses. However, care should be taken when extrapolating to very narrow waveguides. Measured and simulated propagation losses for rib waveguides are shown in Fig. 3(c) and 3(d). As for strip waveguides, the losses of rib waveguides for TM-polarization are larger than for TE-polarization. For TE-polarization, the losses show no significant dependency on waveguide width down to a width of 1.2 μm. For TM-polarization, losses increase rapidly for waveguides less than 3 μm wide. As there was no visible dependency on width for TE-polarization, this case cannot be simulated with our method. For TM-polarization there is good overlap between simulations and measurements. For a width of 1.7 μm, two results are included. The larger value includes measurements on the first 1 cm of the waveguide, while the lower value excludes these. There was a sharp decrease in measured intensity from 0.5 cm to 1 cm, probably cause by a large point defect between these measurements.

Propagation losses for the rib waveguides were, as expected, significantly smaller than for strip waveguides. For a 1.5 μm wide waveguide and TE-polarization, propagation losses

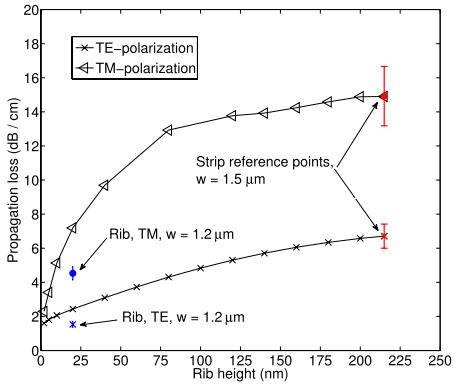

Fig. 4. Simulated propagation loss as function of rib height, $H-h$, based on measured propagation loss for a 1.5 μm wide strip waveguide. Also, measured loss is shown for waveguides with 20 nm rib height and 1.2 μm width.

decreases from 6.7 dB/cm to 1.7 dB/cm when changing from a strip to rib waveguide. To simulate this dependancy on rib height, we have used jn_w found for a strip waveguide, to find the losses for rib waveguides as function of rib height, H-h. In this case, the width was kept fixed at 1.5 μm. The propagation loss is shown in Fig. 4. The measured loss for a waveguide with rib height 20 nm is also shown, with the core thickness 170 nm, versus 215 nm for the strip waveguide.

The simulations show reasonable correspondence with the measured losses for the rib waveguides, given that the measurement uncertainties are large for the reference strip waveguide and the rib waveguides. The simulations predict that propagation losses for TM-polarization can be decreased significantly by reducing the rib height below 20 nm. For TE-polarization, the propagation losses are approximately linear with rib height. For shallow rib waveguides with rib height less than 10 nm, the losses due to sidewall roughness are small and losses from absorption and scattering within the material become dominant, according to our simulations.

IV. Conclusion

The measured propagation losses increased sharply for tantalum pentoxide strip waveguides less than 3 μm wide. For rib waveguides, the propagation losses are significantly smaller than for the strip waveguides. For TE-polarization, the propagation loss was not significantly influenced by the width for rib waveguides. Losses caused by random sidewall imperfections are dependent on fabrication and can vary along a waveguide, as demonstrated in Fig. 3(d) for a width of 1.7 μm. Our simulation method, based on an area with complex refractive index in a 2D-model, gave good estimates for the dependency of propagations losses on waveguide width. The method was also used to estimate the dependency of propagation losses on rib height, showing that losses for TM-polarization decrease fast for rib heights less than 20 nm. For TE-polarization, the losses were predicted to change gradually with rib height.

The measured dependency of propagation losses on waveguide width can, together with the simple proposed simulation method, give valuable information for the design of rib waveguides. The most common way of obtaining single-mode waveguides is to reduce the waveguide width. With the proposed method, it is possible to estimate how the propagation losses will increase when reducing the width for a given technology. The method is based on having several waveguide widths available and the usefulness of the method is thus if considering to reduce the width to even more narrow waveguides than those available. Reducing the rib height is another way of obtaining single-mode waveguides. It is necessary to make several wafers and do more processing to experimentally compare the influence of rib height on propagation losses, while the proposed method can estimate the influence of rib height based on one wafer with a single rib height.

Acknowledgment

The authors would like to thank Dr. Balpreet S. Ahluwalia and Dr. Pål Løvhaugen for helpful inputs.

References

[1] R. G. Hunsperger, *Integrated Optics: Theory and Technology*, vol. 2. New York, NY, USA: Springer-Verlag, 1984.
[2] M.-C. Estevez, M. Alvarez, and L. M. Lechuga, "Integrated optical devices for lab-on-a-chip biosensing applications," *Laser Photon. Rev.*, vol. 6, no. 4, pp. 463–487, 2012.
[3] C. A. Barrios, "Analysis and modeling of a silicon nitride slot-waveguide microring resonator biochemical sensor," *Proc. SPIE*, vol. 7356, pp. 735605-1–735605-10, May 2009.
[4] K. Schmitt, K. Oehse, G. Sulz, and C. Hoffmann, "Evanescent field sensors based on tantalum pentoxide waveguides—A review," *Sensors*, vol. 8, no. 2, pp. 711–738, 2008.
[5] O. Parriaux and G. J. Veldhuis, "Normalized analysis for the sensitivity optimization of integrated optical evanescent-wave sensors," *J. Lightw. Technol.*, vol. 16, no. 4, pp. 573–582, Apr. 1998.
[6] R. G. Heideman and P. V. Lambeck, "Remote opto-chemical sensing with extreme sensitivity: Design, fabrication and performance of a pig-tailed integrated optical phase-modulated mach–zehnder interferometer system," *Sens. Actuators B, Chem.*, vol. 61, no. 1, pp. 100–127, 1999.
[7] F. Prieto, A. Llobera, A. Calle, and L. M. Lechuga, "Design and analysis of silicon antiresonant reflecting optical waveguides for evanscent field sensor," *J. Lightw. Technol.*, vol. 18, no. 7, p. 966, Jul. 2000.
[8] K. Zinoviev, L. G. Carrascosa, J. S. del Río, B. Sepúlveda, C. Domínguez, and L. M. Lechuga, "Silicon photonic biosensors for lab-on-a-chip applications," *Adv. Opt. Technol.*, vol. 2008, pp. 383927-1–383927-6, Apr. 2008.
[9] D. Marcuse, "Mode conversion caused by surface imperfections of a dielectric slab waveguide," *Bell Syst. Tech. J.*, vol. 48, no. 10, pp. 3187–3215, 1969.
[10] F. P. Payne and J. P. R. Lacey, "A theoretical analysis of scattering loss from planar optical waveguides," *Opt. Quant. Electron.*, vol. 26, no. 10, pp. 977–986, 1994.
[11] T. Barwicz and H. Haus, "Three-dimensional analysis of scattering losses due to sidewall roughness in microphotonic waveguides," *J. Lightw. Technol.*, vol. 23, no. 9, pp. 2719–2732, Sep. 2005.
[12] B. S. Ahluwalia, A. Z. Subramanian, O. G. Hellso, N. M. B. Perney, N. P. Sessions, and J. S. Wilkinson, "Fabrication of submicrometer high refractive index tantalum pentoxide waveguides for optical propulsion of microparticles," *IEEE Photon. Technol. Lett.*, vol. 21, no. 19, pp. 1408–1410, Oct. 1, 2009.
[13] F. Wang, F. Liu, G.-K. Chang, and A. Adibi, "Precision measurements for propagation properties of high-definition polymer waveguides by imaging of scattered light," *Opt. Eng.*, vol. 47, no. 2, pp. 024602-1–024602-4, 2008. [Online]. Available: http://dx.doi.org/10.1117/1.2842390
[14] M. H. Jenkins, B. S. Phillips, Y. Zhao, M. R. Holmes, H. Schmidt, and A. R. Hawkins, "Optical characterization of optofluidic waveguides using scattered light imaging," *Opt. Commun.*, vol. 284, no. 16, pp. 3980–3982, 2011.

6.2 Paper 2: Characterization of a waveguide Mach-Zehnder interferometer using PDMS as a cover layer.

Published in Journal of the European Optical Society-Rapid publications, April, 2015.

Authors: Susan M. Lindecrantz, J-C Tinguely, B. Singh Ahluwalia, and Olav Gaute Hellesø.

Contribution notes: The modal behaviour and sensitivity of the optical waveguides was simulated by Susan M. Lindecrantz using COMSOL Multiphysics. These simulations were later verified and confirmed by J.-C. Tinguely using the software Fimmwave (Photon Design, Oxford, UK). All experiments were performed by Susan M. Lindecrantz. Balpreet S. Ahluwalia and Olav Gaute Hellesø supervised the project. The article was written together by Olav Gaute Hellesø and Susan Lindecrantz.

J. Eur. Opt. Soc.-Rapid **10,** 15020 (2015) www.jeos.org

Characterization of a waveguide Mach-Zehnder interferometer using PDMS as a cover layer

S. M. Lindecrantz
susanlindecrantz@gmail.com
UiT - The Arctic University of Norway, Department of Physics and Technology, N-9037 Tromsø, Norway

J.-C. Tinguely
UiT - The Arctic University of Norway, Department of Physics and Technology, N-9037 Tromsø, Norway

B. Singh Ahluwalia
UiT - The Arctic University of Norway, Department of Physics and Technology, N-9037 Tromsø, Norway

O. G. Hellesø
UiT - The Arctic University of Norway, Department of Physics and Technology, N-9037 Tromsø, Norway

A Mach-Zehnder interferometer made with shallow rib waveguides is studied experimentally and using simulations. The rib-height giving single-mode guidance is found as function of core thickness and polarization. Devices have been made using shallow rib waveguides (5 nm rib height) in silicon nitride. The sensitivity and the limit of detection (LOD) is studied experimentally regarding the length of the sensing window and for two cover media: water with hydrochloric acid (HCl) and polydimethylsiloxane (PDMS). For HCl-solution, which is the standard method for testing Mach-Zehnder interferometers, the measured sensitivity and LOD was 13000π rad/RIU and $1.1 \times 10^{-7}\pi$ RIU, respectively, for a 2 cm long sensing window. This is comparable to the best results reported previously. With PDMS as the cover medium, the temperature of the device was increased in order to measure the sensitivity. This is a new approach that makes it possible to measure the sensitivity with a solid cover medium which has a relatively high temperature coefficient for the refractive index. Measured sensitivity and LOD was 15200π rad/RIU and $1.3 \times 10^{-7}\pi$ RIU, respectively, again for a 2 cm long sensing window. Measured sensitivities agreed with simulations and increased linearly with sensing length as expected. However, the LOD showed a minimum for 2 cm sensing length. This was mainly due to increased noise for 3 cm sensing length, both for HCl-solution and PDMS. With higher sensitivity and similar LOD for PDMS compared to HCl-solution, it is concluded that using the temperature dependence of PDMS is a good alternative for testing Mach-Zehnder interferometers.
[DOI: http://dx.doi.org/10.2971/jeos.2015.15020]

Keywords: Rib waveguide, integrated optics, Mach-Zehnder interferometer, polydimethylsiloxane

1 INTRODUCTION

Waveguide Mach-Zehnder interferometers are highly sensitive and have been used successfully for a range of applications, e.g. sensing of pressure [1], gases [2], volatile organic compounds [3], DNA/RNA, proteins and other biological molecules[4, 5]. Several sensors can be combined on a single chip, giving a compact, sensitive and stable device [5]. The principle of the sensor is to use waveguides to split the light into two arms that recombine after a certain distance, see Figure 1. One of the arms (the sensing arm) is covered with a sensitive layer capturing the chemically inert species, while the other arm (the reference arm) is covered with a protective cladding. The evanescent field of the sensing arm interacts with the sensitive layer. A local change of refractive index in this region will change the effective refractive index of the guided mode of the sensing arm. When the reference mode and the sensing mode combine, constructive or destructive interference is obtained depending on the phase change. The phase change of the interference signal can be correlated to the concentration of the measurand with prior calibration.

In this article, the sensitivity and limit-of-detection (LOD) is studied and compared using simulations and measurements for water and polydimethylsiloxane (PDMS) as the cover mediums. Adding hydrochloric acid (HCl) to water is the standard method for characterizing waveguide Mach-Zehnder interferometers and the results can be directly compared with the state-of-the-art. A limit of detection of $10^{-7} - 10^{-8}$ refractive index units (RIU) have been demonstrated with rib waveguides and with a water-solution as the cover medium [6, 7]. Biological materials will normally be dissolved in water, and the most common cover media for biosensors thus have refractive indices close to that of water. For other types of sensors, e.g. gas sensors, various solids can be used to absorb the measurand and hence give a change in the refractive index of the solid. As an example, PDMS doped with cryptophane-A can be used to detect methane with surface plasmon resonance [8, 9]. PDMS is an organic material with a relatively high thermo-optic coefficient, and consequently gives a high thermal sensitivity for the guided mode [10]. This will normally give unwanted temperature dependency for the sensor. However, in this work the high thermal sensitivity is used to characterize the

Received February 05, 2015; revised ms. received March 03, 2015; published April 09, 2015 ISSN 1990-2573

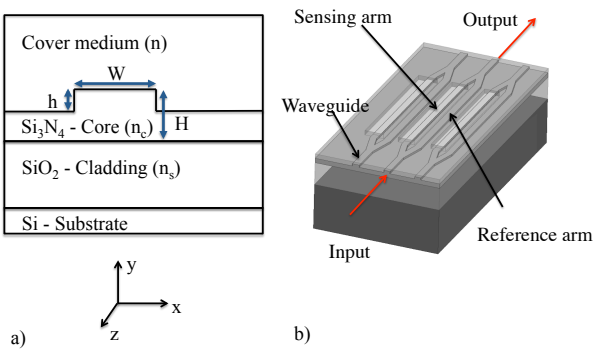

FIG. 1 Shows the outline of the designed sensor with a) cross-section of the waveguide structure and b) top-view of three Mach-Zehnder interferometers on a chip. *W* is the waveguide width, *H* is the core thickness and *h* is the rib height. Note that the drawings are not to scale.

sensor. A PDMS-layer is deposited on the sensing arm of a Mach-Zehnder interferometer, while the reference arm is covered by silica, which has a significantly smaller thermo-optic coefficient. By increasing the temperature of the device, the temperature of the PDMS-layer also increases. As the thermo-optic coefficient of PDMS is known, a controlled change in the refractive index of the PDMS-layer is thus obtained and the sensitivity of the sensor to this change can be measured.

Shallow rib waveguides with a Si_3N_4 core are suitable for Mach-Zehnder interferometers due to the high refractive index of Si_3N_4, good transparency in the visible range and the low propagation losses of the shallow rib structure [11, 12]. To obtain high visibility, the waveguides of the interferometer must be single-mode. We use simulations to determine the geometrical parameters of the waveguide cross-section which result in single-mode waveguides. Comsol Multiphysics, which is based on the finite element method, is used to determine single-mode conditions and to simulate the sensitivity of the sensor to changes in the refractive index of the cladding.

2 SIMULATIONS

The waveguides used in this work had a guiding core of Si_3N_4 (n_c = 2.00) on a silica layer (2 μm thick, n_s = 1.45). The waveguide width was set to 2 μm for the simulations, which can easily be obtained with standard photolithography. Various core thicknesses and rib heights were simulated, as will be shown in the next section. For the cover medium, simulations were done for refractive indices corresponding to water (n = 1.33) and to PDMS (n = 1.412). Figure 1 shows the cross-section of the rib waveguide used in the simulation, and the top-view of three Mach-Zehnder interferometers. A wavelength of 785 nm was used for all the simulations and experiments. Strip waveguides have also been simulated with, by definition, the rib height equal to the core thickness. In order to find the number of modes for the waveguide, and more specifically to find the limit where it becomes single-mode, a 2D mode analysis of the waveguide cross-section was done using Comsol Multiphysics. This mode analysis was also used to find the sensitivity, as explained in the next section. Figure 2 shows examples of the simulated modes for different waveguide widths and polarizations. The evanescent field of a guided mode decreases exponentially away from the waveguide. The single-mode limit was chosen as the point where the evanescent field of the first-order mode ceased to decrease exponentially.

The results obtained with Comsol were compared to simulations performed with Fimmwave (Photon Design, Oxford, UK), which is based on the film mode matching method (FMM) [13]. Using Fimmwave, the single-mode limit was taken as the point where the first-order mode becomes leaky (TE-polarization) or where its loss increases sharply (TM-polarization) when decreasing the rib height [14].

2.1 Geometrical parameters giving single-mode waveguides

Figure 3 shows the maximum rib height which will result in single-mode waveguides, as function of the core thickness. The waveguide width is 2 μm and the single-mode limit is shown for both TE- and TM-polarization and with water and PDMS as cover media. The results obtained with Comsol were confirmed by Fimmwave (not shown). For both polarizations, the differences between the two methods are small and comparable to the resolution of the methods (approximately 1 nm).

For the core thicknesses considered in Figure 3, the single mode limit is decreasing for TM-polarization and slowly increasing for TE-polarization. As the core thickness decreases towards zero, the guiding of the first-order mode will cease for any rib height. Thus, for decreasing core thickness, the single-mode limit increases. This effect is dominating for TM-polarization in Figure 3. For fixed rib height and increasing core thickness, the ratio of rib height to core thickness decreases. This will, at some point, give weaker guiding and the single-mode limit will increase with core thickness. This effect causes the slow increase of the single-mode limit for TE-polarization. For a given polarization and core thickness, the single-mode limit is approximately the same for water, Figure 3(a), as for PDMS, Figure 3(b).

To make single-mode rib waveguides, it is necessary to have tight control of the etching of the rib because a rib height of less than 7 nm is required. On the other hand, the width can be relatively large. The width of 2 μm considered in these simulations, is compatible with standard photolithography. By reducing the rib height further, towards 3 nm, waveguides can be made single-mode for a width of 4 μm [15]. For strip waveguides, the core is etched completely down and the control on the etching process is thus relaxed. However, the width has to be significantly smaller and it is thus difficult to make single-mode strip waveguides with standard contact photolithography.

2.2 Sensitivity of the sensor

The evanescent field reaches out into the cover medium on top of the waveguide. Any change of the refractive index of

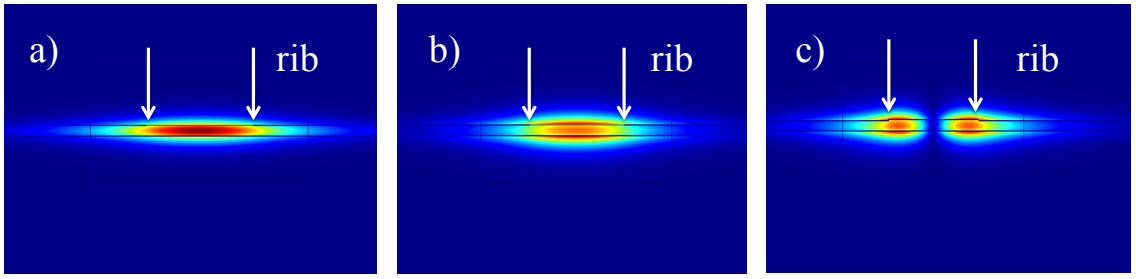

FIG. 2 Examples of modes for a shallow rib waveguide. a) and b) shows the fundamental TE- and TM-mode, respectively (5 nm rib height, 2 µm rib width and 200 nm core thickness). c) shows the first order TM-mode (15 nm rib height, 2 µm rib width and 200 nm core thickness).

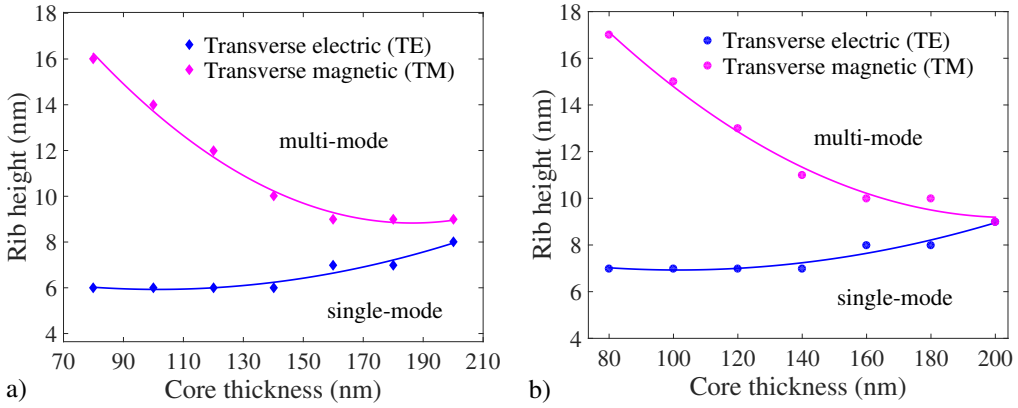

FIG. 3 Shows the simulated single-mode conditions for 2 µm wide rib waveguides with TE- and TM-polarization. The single-mode limit is shown for a cover medium of a) water (n = 1.33) and b) PDMS (n = 1.412).

the sensitive layer will thus change the effective refractive index of the mode. The sensitivity to this change in refractive index is dictated by the waveguide dimensions and by the choice of materials. Homogeneous sensitivity is defined as the rate of change of the effective refractive index of the guided mode, to the rate of change of the refractive index of a homogeneous cover medium. The homogeneous sensitivity can be expressed as [16, 17],

$$\frac{\Delta N}{\Delta n} = \frac{n}{N}\frac{P_o}{P_T} * (2\frac{N^2}{n^2} - 1)^r, \tag{1}$$

where n is the cover medium refractive index, N is the effective refractive index of the guided mode, P_o is the power of the guided mode in the cover medium, and P_T is the total power of the guided mode. Here $r = 0$ for TE-polarization and $r = 1$ for TM-polarization. Furthermore, the phase sensitivity for homogeneous sensing can be expressed as:

$$\frac{\Delta\theta}{\Delta n} = \frac{2\pi * L}{\lambda_o} * \frac{\Delta N}{\Delta n}, \tag{2}$$

where L is the sensing length, λ_o is the wavelength and $\frac{\Delta N}{\Delta n}$ is the homogeneous sensitivity found in Eq. (1). The minimum detectable phase shift, $\Delta\theta_{min}$, can be estimated as three times the signal-to-noise ratio, given by the noise, σ, divided by the maximum intensity change, ΔI, of the fringes:

$$\Delta\theta_{min} = \frac{3\sigma\pi}{\Delta I}. \tag{3}$$

To compare the performance of various sensors, it is most common to use the limit-of-detection (LOD = Δn_{min}), which is given by the minimum detectable phase shift divided by the phase sensitivity:

$$\Delta n_{min} = \frac{\Delta\theta_{min}}{S}. \tag{4}$$

Simulations were done with Comsol Multiphysics to determine the variables in Eq. (1) for various geometrical parameters, to find the corresponding sensitivity. Figure 4 shows the calculated homogeneous sensitivities as function of the core thickness for strip and rib waveguides, with PDMS and water as the cover media. The sensitivity is very dependent on the core thickness and to some degree on the polarization of the guided light. The sensitivity increases as the core thickness decreases, due to less confinement in the waveguide core, which implies more power in the cover medium. For even less core thickness, the sensitivity decreases as the mode approaches cut-off. In general, maximum sensitivity for TE-polarization is obtained with a thinner waveguide than for TM-polarization. The maximum sensitivity is highest for TM-polarization, being 28% higher than for TE-polarization for water as the sensing medium. Likewise, for PDMS as the sensing medium, the sensitivity is 18% higher for TM than for TE-polarization. Regarding water and PDMS as cover medium, the sensitivity is 47% higher for TE and 35% higher for TM for PDMS than for water as the cover medium. This can be explained by PDMS having a refractive index closer to that of the waveguide core. If PDMS is used as the sensing medium, it is thus better to test the sensor with PDMS rather than HCl-solution, as the sensitivity is higher for PDMS.

Strip waveguides give approximately 4–8% higher sensitiv-

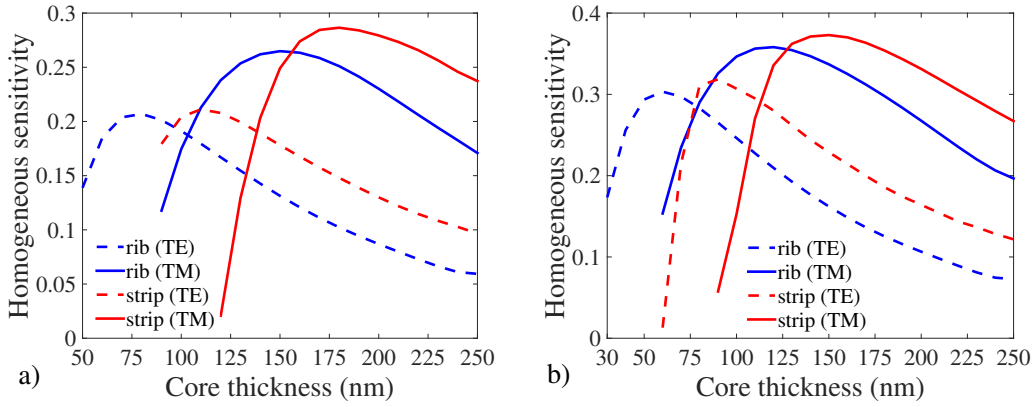

FIG. 4 Shows the homogeneous sensitivity with a) water as cover medium (n = 1.33) and b) with PDMS as cover medium (n = 1.412). The sensitivity is shown as function of core thickness for a 0.5 μm wide strip waveguide (red) and for a 2 μm wide rib waveguide (blue, 5 nm rib height). Both waveguides are single-mode.

ity compared to rib waveguides. The maximum sensitivity for both polarizations is also shifted towards higher core thicknesses for strip waveguides compared to rib waveguides (180 vs. 150 nm for water and TM-polarization). The sensitivity is thus not significantly dependent on the choice of strip or rib waveguides. We have also found that the sensitivity does not vary much as function of the waveguide width and rib height, and these results are thus not shown. This can be expected from the small change in effective refractive index of the mode relative to these parameters. Changing the wavelength merely gives a shift of the curves (also not shown).

3 MEASUREMENT OF THE SENSITIVITY OF THE SENSOR

Waveguide Mach-Zehnder interferometers were made with a core thickness of 150 nm, rib height of 5 nm and waveguide widths between 1.5 μm and 3 μm. According to the simulations, see Figure 3 and Figure 4, these dimensions give single-mode waveguides and maximum sensitivity for TM-polarization. The fabrication was done according to Prieto et al. [15]. First, a silica layer with a thickness of 2 μm was thermally grown on a silicon wafer. The core layer of silicon nitride, Si_3N_4, was deposited by low-pressure chemical vapor deposition (LPCVD) at 800 °C and the rib structure of 5 nm was etched by reactive ion etching (RIE). A protective layer was deposited by plasma-enhanced chemical vapor deposition (PECVD) at 300 °C. Sensing windows were opened in the protective layer by RIE and wet etching. These windows were 1, 2 and 3 cm long, 1 μm deep and 50 μm wide.

In this section, the sensitivity is measured with water and then with PDMS as the sensing medium (i.e. cover medium). The refractive index of water is increased by adding hydrochloric acid (HCl) and the refractive index of the solution is measured with a refractometer. Thus, changing the cover medium from pure water to an HCl-solution gives interference fringes. By measuring the number of fringes for solutions with various concentrations of HCl, the sensitivity of the sensor is found. For PDMS, a similar approach is not possible. However, the thermo-optic coefficient of the refractive index is $\Delta n/\Delta T = -4.2 \times 10^{-4}$ RIU/K for PDMS, compared to $\Delta n/\Delta T = 1.28 \times 10^{-5}$ RIU/K for silica [18]. Thus, by increasing the temperature of the device, the refractive index of PDMS will decrease and give interference fringes at the output of the interferometer. Note that the reference arm of the interferometer is covered with silica, and it is thus the difference in temperature coefficient between PDMS and silica that gives the interference fringes.

Figure 5 shows the experimental setup. Light from a 785 nm diode laser was coupled into the waveguide using beam expanding lenses and a 10x objective lens (NA = 0.30). The low magnification, 10x, was chosen in order to reduce the influence of thermal and mechanical noise on the input coupling. This was particularly important when increasing the temperature of the waveguide chip. The polarization was rotated with a half-wave plate to obtain TM-polarization for highest sensitivity. A microscope with a CCD camera was used to align the input beam with the waveguide and get optimal end-coupling into the waveguide. A second objective lens (40x, NA = 0.65) was used to couple light out from the waveguide and into a photodetector.

For measurements with water as the cover medium, the waveguide chip was enclosed within a microfluidic system connected to an injection port, providing constant feed of water or the diluted HCl. At room temperature, HCI is a colorless gas that is highly soluble in water. Concentrations of 0.03 mol/L to 0.3 mol/L of HCl was added to water. The refractive index of the solution was measured with a refractometer. For example, with a solution of 0.2 mol/L HCI, a change in refractive index of 0.0029 RIU relative to water, was obtained.

Water was pumped continuously at a rate of 0.03 to 0.06 ml/min to the sensing region of the interferometer through the microfluidic system. 5 ml of HCl-solution was injected via an injection port into the flow. Once the injection port was activated, (pure) water was replaced with HCl-solution, causing the first series of fringes at the output of the interferometer (see the insets in Figure 6). When the volume of HCl-solution was finished, water was pumped back into the system, giving rise to a second series of fringes. After the measurements, the phase was found by counting the fringes, with one fringe equal to 2π.

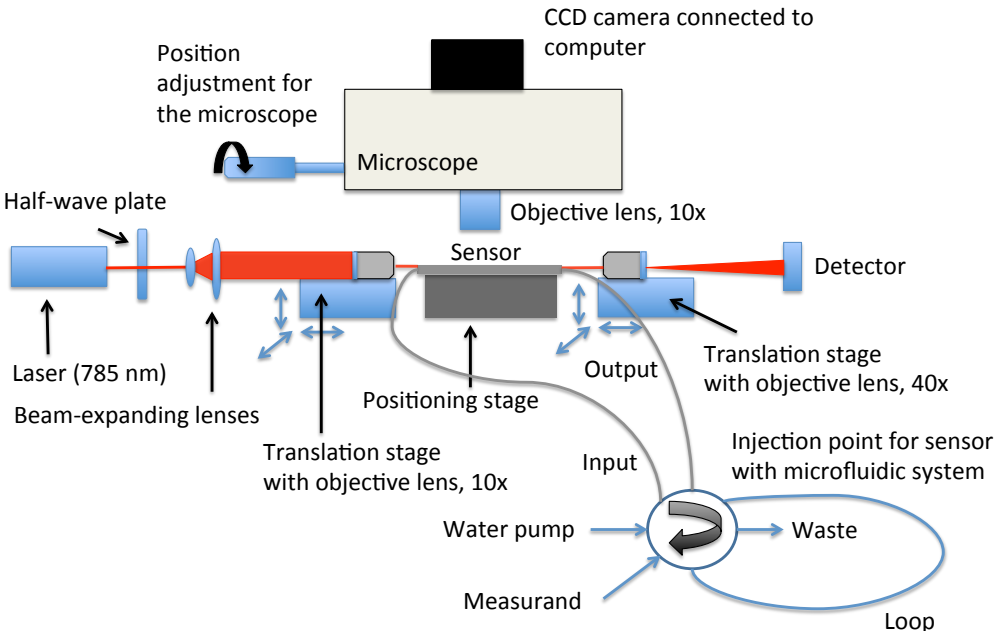

FIG. 5 Shows the experimental setup used for the measurements with a microfluidic system connected to an injection point for HCl and water pump system.

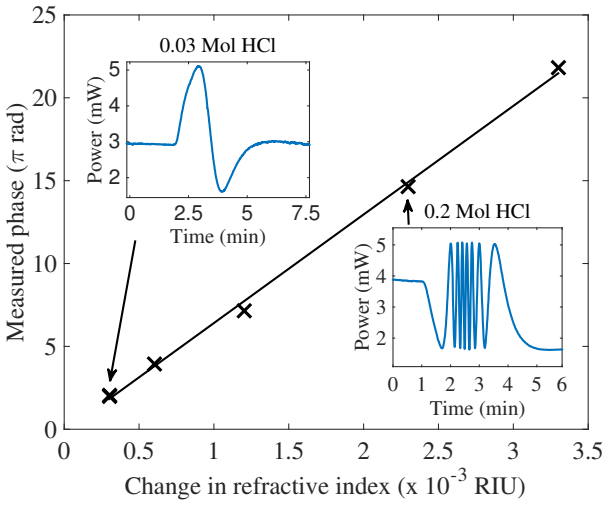

FIG. 6 Shows the calibration curve with HCl-solutions for a Mach-Zehnder interferometer with a 2 µm wide waveguide and a sensing length of 1 cm. A straight line is fitted to the measurements and a phase change of 6552π rad/RIU in water is obtained. The insets show the resulting interference fringes when changing the measurand from pure water to 0.03 mol and 0.2 mol HCl, respectively.

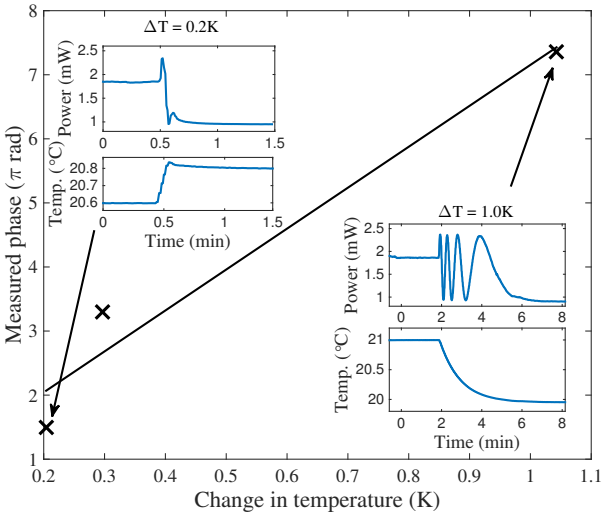

FIG. 7 Shows the calibration curve for a Mach-Zehnder interferometer with PDMS on the sensing arm. The waveguide is 2 µm wide and the sensing window is 2 cm long. A straight line is fitted to the measurements and a phase change of 6.4π rad/K in PDMS is obtained. The insets show the resulting interference fringes when increasing the temperature by 0.2 K and 1 K, respectively.

Figure 6 shows an example of a calibration curve obtained for different concentrations of HCI in water. The sensitivity of phase change to change in refractive index of the cover medium is found by making a linear fit to the measured values. This measurement series for 1 cm sensing length gave a sensitivity of $S = \Delta\theta/\Delta n = 6552\pi$ rad/RIU for water as cover medium.

To measure the sensitivity with PDMS as the cover medium, the waveguide chip was covered with a layer of PDMS using spin-coating (approximately 25 µm thick). A Peltier-element was used to control the temperature, with an aluminium plate on top holding the waveguide chip. A small current was used for the Peltier-element to obtain small temperature changes and avoid oscillations. A thermistor was fixed inside the aluminium plate to precisely measure the temperature changes. Thermal paste was used between the parts to have good thermal conductivity. The temperature and the resulting interference fringes were recorded, as shown in the insets in Figure 7. By applying increasing currents, and thus increasing temperature steps, the sensitivity was measured. An example of a measurement of sensitivity is shown in Figure 7 for an interferometer with a sensing length of 2 cm.

Cover medium:	**HCl-solution**			**PDMS**		
L [cm]	1	2	3	1	2	3
Simulated $S(n)$ $[\times 10^3\pi$ rad/RIU]	6.7	13.5	20.2	8.5	17.2	25.7
Measured $S(n)$ $[\times 10^3\pi$ rad/RIU]	6.5	13.0	19.8	8.8	15.2	26.2
Measured $S(T)$ $[\pi$ rad/K]	–	–	–	3.7	6.4	11.0
dP [mW]	3.4	0.6	0.8	0.7	1.4	0.7
σ [μW]	7.1	0.9	9.0	1.9	2.8	4.0
$\Delta\theta_{min}$ $[\times 10^{-3}\pi$ rad]	6.3	4.5	33.7	8.1	6.0	17.1
LOD(n) $[\times 10^{-7}\pi$ RIU]	3.1	1.1	5.4	3.0	1.3	2.1
LOD(T) [mK]	–	–	–	2.2	0.9	1.6

TABLE 1 Results obtained for various sensing lengths and with water and PDMS as the cover medium. L is the sensing length,S is the phase sensitivity as function of the refractive index $S(n)$ or temperature $S(T)$, dP is the mean visibility of the fringes, σ is the noise of the signal, $\Delta\theta_{\text{min}}$ is the minimum phase-change that can be detected and LOD is the limit-of-detection as function of refractive index, LOD(n), or temperature, LOD(T).

This measurement series gave a temperature sensitivity of $S = \Delta\theta/\Delta T = 6.4\pi$ rad/K. The temperature sensitivity is related to the phase sensitivity by:

$$\frac{\Delta\theta}{\Delta n} = \frac{\Delta\theta}{\Delta T} \times \frac{\Delta T}{\Delta n}. \tag{5}$$

As previously noted, the thermo-optic coefficient of the refractive index of PDMS is $\Delta n/\Delta T = -4.2 \times 10^{-4}$ RIU/K [18]. The phase sensitivity S can thus be found from Eq. (5). For PDMS, the phase sensitivity is thus calculated from the measured temperature sensitivity, while for HCl-solution, the phase sensitivity is measured directly by increasing the refractive index of the HCl-solution.

A summary of the results obtained for various sensing lengths is shown in Table 1 for both HCl-solution and PDMS. The sensitivity increased linearly with the length of the sensing window, as expected, and with very good correspondence with the simulation results. This implies that the thermo-optical coefficient used for PDMS is correct. The sensitivity for PDMS is higher than for HCl-solution due to the higher refractive index (1.42 vs. 1.33), as discussed in the simulation part.

As the sensing length increases, propagation losses are expected to reduce the fringe visibility. However, this effect is not clear from the results in Table 1, indicating that random coupling losses and waveguide defects are more important sources of loss than evenly distributed propagation losses. The noise level increases with sensing length, at least for PDMS. For HCl-solution, the flow cell had a length of 3 cm and was thus as long as the longest sensing window. The positioning of the flow cell relative to the sensing window and flow effects near the edges of the flow cell might have given increased noise for a sensing length of 3 cm. A longer chip with space for a longer flow cell might give lower noise and a lower detection limit for a 3 cm sensing length. For PDMS, noise is increasing with sensing length, indicating that temperature noise increases with length and that the sources of the noise are uniformly distributed. The temperature noise of the Peltier-element was approximately 0.5 mK. Reducing the temperature noise of the regulation system will also reduce the noise for the optical measurement. Due to the higher noise for 3 cm sensing length than for 2 cm, for both HCl-solution and PDMS, the limit-of-detection is lowest for a sensing length of 2 cm, at 1.1 and 1.3 $\times 10^{-7}\pi$ RIU, respectively.

As shown in Table 1, an LOD for temperature of approximately 1 mK corresponds to an LOD for phase of approximately $10^{-7}\pi$ RIU with PDMS on the sensing arm. Thus it is possible to use the PDMS layer for measuring temperature directly with a limit of detection of approximately 1 mK. If using PDMS as a sensitive layer for gas measurement, the temperature stability will influence the LOD for the gas measurement. If temperature stability is the limiting noise source and PDMS is used on the sensing arm only, a temperature noise of 1 mK will thus give an LOD for phase of $1 \times 10^{-7}\pi$ RIU. It might be possible to improve this if the reference arm is also covered with PDMS and subsequently protected with a layer that stops gas diffusion.

4 CONCLUSION

The main factors for the sensitivity are the core thickness relative to the wavelength of light, the polarization of the light and the refractive index of the core and cover medium. For shallow rib waveguides and a wavelength of 785 nm, the core thickness giving maximum sensitivity was found to be 80 nm and 150 nm for TE- and TM-polarization, respectively, with water as the cover medium. With PDMS as the cover medium, the corresponding values were 60 and 120 nm.

The sensitivity was found to be approximately 28% higher for TM-polarization than for TE-polarization for water and 18% higher for TM-polarization than for TE-polarization for PDMS. Strip waveguides give 4–8% higher sensitivity than rib waveguides. It is possible to make the shallow rib waveguides with standard contact photolithography, significantly simplifying the fabrication process, and the small reduction of sensitivity is thus justified. The sensitivity is 47% higher for TE and 35% higher for TM for PDMS than for water as the cover medium. This can be explained by PDMS having a refractive index closer to that of the waveguide core. However, in most cases it will be the type of measurand, e.g. biological or chemical, that decides the choice of cover medium, rather than the higher sensitivity for PDMS.

Sensitivity was measured with HCl as the cover medium and a Mach-Zehnder interferometer with 2 μm waveguide width, 5 nm rib height, 150 nm core thickness and 1, 2 and 3 cm sensing lengths. The measured sensitivities agreed well with the

simulated values. The lowest limit of detection was found for a sensing length of 2 cm, with LOD = $1.1 \times 10^{-7}\pi$ RIU. This is comparable to the results obtained in the literature [7, 19]. By improving the flow cell and reduce the noise for a sensing length of 3 cm, it may be possible to reduce the limit of detection further.

Water is the normal cover medium for biological sensors. However, for gas sensors, it is more common to have a solid cover medium and a different approach must be used when measuring the sensitivity. In this work, we have covered the sensing arm with PDMS and applied a temperature change to the sensor, which decreases the refractive index of the cover layer. This, in turn, was used to measure the sensitivity with PDMS as a cover medium. The sensitivity was, as expected, higher than for HCl-solution and the limit of detection was almost the same, at $1.3 \times 10^{-7}\pi$ RIU. This demonstrates that PDMS can be used to test waveguide Mach-Zehnder interferometers and it is thus an alternative to testing with HCl-solution. We chose to use a low-magnification objective for input coupling (10x), giving a relatively large spot on the endface of the waveguide. This was done in order to reduce noise from the input coupling when increasing the temperature. However, it comes at the expense of reduced coupling. In general, some experimental precautions must be taken when changing the temperature of the chip, as thermal expansion of the mechanical stage can reduce the input coupling.

It is also possible to use the PDMS-layer for temperature measurement, with a limit of detection of approximately 1 mK demonstrated here. If using a PDMS layer for sensing a different measurand, e.g. PDMS doped with cryptophane-A for methane-sensing, the thermal noise must be on the order of 1 mK to obtain a limit of detection of $1 \times 10^{-7}\pi$ RIU, if PDMS is used only on the sensing arm.

5 ACKNOWLEDGEMENTS

This work is part of the project Subsea Sensors for Oil and Gas funded by the Research Council of Norway. The waveguides were made by Carlos Dominguez and co-workers (CSIC, Barcelona, Spain).

References

[1] C. Wagner, J. Frankenberger, and P. P. Deimel, "Optical pressure sensor based on a Mach-Zehnder interferometer integrated with a lateral a-Si:H p-i-n photodiode," IEEE Photonic. Tech. L. **5**, 1257–1259 (1993).

[2] N. Fabricius, G. Gauglitz, and J. Ingenhoff, "A gas sensor based on an integrated optical Mach-Zehnder interferometer," Sensor. Actuat. B-Chem. **7**, 672–676 (1992).

[3] A. L. Siarkowski, L. F. Hernandez, B.-H. V. Borges, and N. I. Morimoto, "Sensing based on Mach-Zehnder interferometer and hydrophobic thin films used on volatile organic compounds detection," Opt. Eng. **51**, 054401 (2012).

[4] A. Densmore, D.-X. Xu, S. Janz, P. Waldron, J. Lapointe, T. Mischki, G. Lopinski, *et al.*, "Sensitive label-free biomolecular detection using thin silicon waveguides," Adv. Opt. Technol. **2008**, 725967 (2008).

[5] P. Kozma, F. Kehl, E. Ehrentreich-Förster, C. Stamm, and F. F. Bier, "Integrated planar optical waveguide interferometer biosensors: a comparative review," Biosens. Bioelectron. **58**, 287–307 (2014).

[6] R. Heideman, and P. Lambeck, "Remote opto-chemical sensing with extreme sensitivity: design, fabrication and performance of a pigtailed integrated optical phase-modulated Mach–Zehnder interferometer system," Sensor. Actuat. B-Chem. **61**, 100–127 (1999).

[7] S. Dante, D. Duval, B. Sepúlveda, A. B. González-Guerrero, J. R. Sendra, and L. M. Lechuga, "All-optical phase modulation for integrated interferometric biosensors," Opt. Express **20**, 7195–7205 (2012).

[8] C. Boulart, M. C. Mowlem, D. P. Connelly, J.-P. Dutasta, and C. R. German, "A novel, low-cost, high performance dissolved methane sensor for aqueous environments," Opt. Express **16**, 12607–12617 (2008).

[9] C. Boulart, R. Prien, V. Chavagnac, and J.-P. Dutasta, "Sensing dissolved methane in aquatic environments: an experiment in the central Baltic Sea using surface plasmon resonance," Environ. Sci. Technol. **47**, 8582–8590 (2013).

[10] C. Delezoide, I. Ledoux-Rak, and C. T. Nguyen, "General approach for the sensitivity analysis and optimization of integrated optical evanescent-wave sensors," J. Opt. Soc. Am. B **31**, 851–859 (2014).

[11] N. Daldosso, M. Melchiorri, F. Riboli, F. Sbrana, L. Pavesi, G. Pucker, C. Kompocholis, *et al.*, "Fabrication and optical characterization of thin two-dimensional Si_3N_4 waveguides," Mat. Sci. Semicon. Proc. **7**, 453–458 (2004).

[12] S. M. Lindecrantz, and O. G. Hellesø, "Estimation of propagation losses for narrow strip and rib waveguides," IEEE Photon. Technol. L. **26**, 1836–1839 (2014).

[13] X. Xu, S. Chen, J. Yu, and X. Tu, "An investigation of the mode characteristics of SOI submicron rib waveguides using the film mode matching method," J. Opt. A-Pure Appl. Op. **11**, 015508 (2009).

[14] F. T. Dullo, J.-C. Tinguely, S. A. Solbø, and O. G. Hellesø, "Single-mode limit and bending losses for shallow rib Si_3N_4 waveguides," IEEE Photon. J. **7**, 1–11 (2015).

[15] F. Prieto, B. Sepúlveda, A. Calle, A. Llobera, C. Domínguez, A. Abad, and A. Montoya, "An integrated optical interferometric nanodevice based on silicon technology for biosensor applications," Nanotechnology **14**, 907–912 (2003).

[16] K. Tiefenthaler, and W. Lukosz, "Sensitivity of grating couplers as integrated-optical chemical sensors," J. Opt. Soc. Am. B **6**, 209–220 (1989).

[17] F. Prieto, A. Llobera, D. Jiménez, C. Doménguez, A. Calle, and L. M. Lechuga, "Design and analysis of silicon antiresonant reflecting optical waveguides for evanscent field sensor," J. Lightwave Technol. **18**, 966-972 (2000).

[18] G. L. Klunder, and R. E. Russo, "Core-based intrinsic fiber-optic absorption sensor for the detection of volatile organic compounds," Appl. Spectrosc. **49**, 379–385 (1995).

[19] K. Zinoviev, L. G. Carrascosa, J. Sánchez del Río, B. Sepúlveda, C. Domínguez, and L. M. Lechuga, "Silicon photonic biosensors for lab-on-a-chip applications," Adv. Opt. Technol. **2008**, 383927 (2008).

6.3 Paper 3: Sensitive on-chip methane detection with a cryptophane-A cladded Mach-Zehnder interferometer.

Published in Optics Express, November, 2015.

Authors: Firehun T. Dullo, Susan M. Lindecrantz, Jana Jàgerskà, Jørn H. Hansen, Magnus Engqvist, Stian Andre Solbø, and Olav Gaute Hellesø.

Contribution notes: The experimental work was done in collaboration between Susan M. Lindecrantz and Firehun T. Dullo (joint first authors). Jana Jàgerskà contributed to the final stage of the methane sensing and wrote the main parts of the article. Jørn H. Hansen and Magnus Engqvist contributed with the fabrication of cryptophane-A and provided helpful discussions regarding cryptophane-A and the chemistry.

Sensitive on-chip methane detection with a cryptophane-A cladded Mach-Zehnder interferometer

Firehun Tsige Dullo,[1,2] Susan Lindecrantz,[1] Jana Jágerská,[1,*] Jørn H. Hansen,[3] Magnus Engqvist,[3] Stian Andre Solbø,[2] and Olav Gaute Hellesø[1]

[1]*Department of Physics and Technology, UiT The Arctic University of Norway, 9037 Tromsø, Norway*

[2]*Northern Research Institute, 9294 Tromsø, Norway*

[3]*Department of Chemistry, UiT The Arctic University of Norway, 9037 Tromsø, Norway*

[*]*jana.jagerska@uit.no*

Abstract: We report a methane sensor based on an integrated Mach-Zehnder interferometer, which is cladded by a styrene-acrylonitrile film incorporating cryptophane-A. Cryptophane-A is a supramolecular compound able to selectively trap methane, and its presence in the cladding leads to a 17-fold sensitivity enhancement. Our approach, based on 3 cm-long low-loss Si_3N_4 rib waveguides, results in a detection limit as low as 17 ppm. This is 1-2 orders of magnitude lower than typically achieved with chip-scale low-cost sensors.

OCIS codes: (130.3120) Integrated optics devices; (130.6010) Sensors; (230.3120) Integrated optics devices.

References and links

1. IPCC Fifth Assessment Report (WGI AR5), *Climate Change 2013: The Physical Science Basis, Summary for Policymakers* (Cambridge University, 2013).
2. J. Hodgkinson and R. P. Tatam, "Optical gas sensing: a review," Meas. Sci. Technol. **24**, 012004 (2013).
3. J. Shemshada, S. M. Aminossadati, M. S. Kizil, "A review of developments in near infrared methane detection based on tunable diode laser," Sens. Actuators B Chem. **171-172**, 77–92 (2012).
4. N. S. Lawrence, "Analytical detection methodologies for methane and related hydrocarbons," Talanta **69**, 385–392 (2006).
5. T. Brotin and J.-P. Dutasta, "Cryptophanes and Their Complexes–Present and Future," Chem. Rev. **109**, 88–130 (2009).
6. L. Garel, J.-P. Dutasta, and A. Collet, "Complexation of Methane and Chlorofluorocarbons by Cryptophane–A in Organic Solution," Angew. Chem. Int. Ed. Engl. **32**, 1169–1171, (1993).
7. E. Souteyrand, D. Nicolas, J.R. Martin, J.P. Chauvet, H. Perez, "Behaviour of cryptophane molecules in gas media," Sens. Actuators B Chem. **33**, 182–187 (1996).
8. K. E. Chaffee, H. A. Fogarty, T. Brotin, B. M. Goodson, and J.-P. Dutasta. "Encapsulation of small gas molecules by cryptophane–111 in organic solution. 1. Size-and shape-selective complexation of simple hydrocarbons," J. Phys. Chem. A **113**, 13675–13684 (2009).
9. M. Benounis, N. Jaffrezic-Renault, J.-P. Dutasta, K. Cherif, and A. Abdelghani, "Study of a new evanescent wave optical fibre sensor for methane detection based on cryptophane molecules," Sens. Actuators B Chem. **107**, 32–39 (2005).
10. J. Yang, Ch. Tao, X. Li, G. Zhu, and W. Chen, "Long-period fiber grating sensor with a styrene-acrylonitrile nano-film incorporating cryptophane A for methane detection," Opt. Express **19**, 14696–14706 (2011).
11. J. Yang, L. Zhou, J. Huang, Ch. Tao, X. Li, and W. Chen, "Sensitivity enhancing of transition mode long-period fiber grating as methane sensor using high refractive index polycarbonate/cryptophane A overlay deposition," Sens. Actuators B Chem. **207**, 477–480 (2015)

#245563 Received 10 Jul 2015; revised 21 Sep 2015; accepted 23 Oct 2015; published 24 Nov 2015

12. C. Boulart, M. C. Mowlem, D. P. Connelly, J.-P. Dutasta, and Ch. R. German, "A novel, low-cost, high performance dissolved methane sensor for aqueous environments," Opt. Express **16**, 12607–12617 (2008) .
13. C. Wagner, C., J. Frankenberger, and Peter P. Deimel. "Optical pressure sensor based on a Mach-Zehnder interferometer integrated with a lateral a-Si: H pin photodiode," IEEE Photon. Tech. Lett. **5**, 1257–1259 (1993).
14. N. Fabricius, G. Gauglitz, and J. Ingenhoff, "A gas sensor based on an integrated optical Mach-Zehnder interferometer," Sens. Actuators B Chem. **7**, 672–676, (1992).
15. A. L. Siarkowski, L. F. Hernandez, B.-H. Viana Borges, N. I.Morimoto, "Sensing based on Mach-Zehnder interferometer and hydrophobic thin films used on volatile organic compounds detection," Opt. Eng. **51**, 054401 (2012).
16. A. Densmore, D. X. Xu, S. Janz, P. Waldron, J. Lapointe, T. Mischki, G. Lopinski, A. Delâge, J. H. Schmid, and P. Cheben, "Sensitive label-free biomolecular detection using thin silicon waveguides," Adv. Opt. Technol. **2008**, 725967 (2008).
17. P. Kozma, F. Kehl, E. Ehrentreich-Frster, Ch. Stamm, F. F. Bier, "Integrated planar optical waveguide interferometer biosensors: A comparative review," Biosens. Bioelectron. **58**, 287–307, (2014).
18. F. Prieto, B. Sepúlveda, A. Calle, A. Llobera, C. Dominguez, A. Abad, and A. Montoya, "An integrated optical interferometric nanodevice based on silicon technology for biosensor applications," Nanotechnology **14**, 907–912 (2003).
19. S. Lindecrantz, J.-C. Tinguely, B. S. Ahluwalia, O. G. Hellesø, "Characterization of a waveguide Mach-Zehnder interferometer using PDMS as a cover layer," J. Eur. Opt. Soc, Rapid Publ. **10**,1990–2573 (2015).
20. F. T. Dullo, J.-C. Tinguely, S. A. Solbø, and O. G. Hellesø, "Single-mode limit and bending losses for shallow rib Si_3N_4 waveguides," IEEE Photon. J. **7**, 1–11 (2015).
21. J. Canceill, and A. Collet, "Two-step synthesis of D 3 and C 3h cryptophanes," J. Chem. Soc., Chem. Commun. **9**, 582–584 (1988).
22. N. Aissaoui, L. Bergaoui, J. Landoulsi, J.-F. Lambert, and S. Boujday, "Silane Layers on Silicon Surfaces: Mechanism of Interaction, Stability, and Influence on Protein Adsorption," Langmuir **28**, 656–665 (2012).
23. D. MacDougall, W. B. Crummett, "Guidelines for data acquisition and data quality evaluation in environmental chemistry," Anal. Chem. **52**, 2242–2249 (1980).
24. H.-P. Loock, P. D. Wentzell, "Detection limits of chemical sensors: Applications and misapplications," Sens. Actuators B Chem. **173**, 157–163 (2012).
25. D. R. Jacobson, N. S. Khan, R. Coll, R. Fitzgerald, L. Laureano-Prez, Y. Bai and I. J. Dmochowskia, "Measurement of radon and xenon binding to a cryptophane molecular host," Proc Natl. Acad. Sci. U.S.A. **108**, 10969–10973 (2011).
26. Z. Takacs, E. Steiner, J. Kowalewski, and T. Brotin, "NMR Investigation of Chloromethane Complexes of Cryptophane-A and Its Analogue with Butoxy Groups," J. Phys. Chem. B **118**, 2134–2146 (2014).

1. Introduction

Interest in methane detection has increased in recent years due to focus on the environmental effects of the greenhouse gases and climate change. Methane (CH_4) has approximately 30 times higher global warming potential than CO_2 and its amount in the atmosphere has increased by a factor of 2.5 since pre-industrial times: from 0.7 ppm to the current 1.8 ppm [1]. In order to better understand the global methane cycle, it is essential to quantify the atmospheric methane sources, including emissions from remote and inaccessible wetlands, permafrost and methane clathrates. Such a task requires the availability of low-cost and sensitive methane sensors, which are sufficiently small to be carried by lightweight planes or drones, and at the same time robust enough to be operated in extreme weather conditions. The currently available sensors are traditionally limited to high-end laboratory equipment, such as gas chromatographs, mass spectrometers or near-infrared and mid-infrared laser spectrometers, which perform extremely well in terms of sensitivity (ppt levels), specificity (interference-free) and long term stability, but are bulky and expensive [2, 3]. On the other hand, there are ultra low-cost devices such as nondispersive infrared sensors, pellistors, metal-oxide or electrochemical gas sensors, but these suffer from limited sensitivity, long-term drift and cross-responsivity to other chemical species [4].

An alternative approach to methane detection is based on cryptophanes [5], which are supramolecular compounds that form a host cavity. The cavity can selectively capture molecules whose dimensions are compatible with the cavity size. Cryptophane-A, the smallest of the series, exhibits a strong affinity towards methane [6–8]. When incorporated into polymer

#245563 Received 10 Jul 2015; revised 21 Sep 2015; accepted 23 Oct 2015; published 24 Nov 2015

solutions such as Polydimethylsiloxane (PDMS) or Styrene-Acrylonitrile (SAN), the resulting transparent films can be used as a sensitive cladding layer for optical refractive index sensors. An optical fibre sensor for methane detection based on cryptophane molecules incorporated in a PDMS cladding was first reported in 2005 by Bernouis et al. [9]. Since then, several different sensor designs were proposed. Long-period fiber grating sensors with a SAN and polycarbonate overlay [10, 11] have achieved a detection limit down to 0.1 vol. %. Another design, a surface plasmon resonance sensor for methane detection in water [12], has reached a remarkably low detection limit of 0.2 nM, which shows the potential of cryptophane-based sensing for specific methane detection down to ambient CH_4 concentrations. Nevertheless, the reported techniques unanimously rely on the measurement of resonance shifts, which implies the use of a tuneable laser source or a spectrometer. This increases the sensor price as well as its footprint.

On-chip interferometric techniques represent a solution to overcome this drawback. In particular, the waveguide Mach-Zehnder interferometer is highly appealing as it is sensitive to very small refractive index variations. It has been successfully employed for a wide range of applications, such as sensing of pressure [13], gases [14], volatile organic compounds [15], DNA/RNA, proteins and other biological molecules [16, 17]. Several sensors, including a reference Mach-Zehnder interferometer, can be combined on a single chip [17], resulting in a compact and stable device. The sensitivity range of Mach-Zehnder interferometers can be adapted to the application by choosing the waveguide length, and since they do not require a tuneable laser, they can be produced at a competitive price.

In this work, we adopt the above strategy to develop an on-chip methane sensor based on a Mach-Zehnder interferometer. The device is sensitised to methane by incorporating cryptophane-A molecules in the waveguide cladding, which results in more than one order of magnitude sensitivity and selectivity enhancement and a detection limit down to ppm levels. As such, it is an excellent candidate for quantification of methane release from a multitude of natural and anthropogenic emission sources.

2. Sensor design and principle of operation

Figure 1 shows an integrated Mach-Zehnder interferometer, where the optical signal is split into two branches: a reference arm which is protected from the surrounding environment and a sensing arm which is exposed to the analyte. The presence of the analyte modifies the refractive index in the sensing arm, resulting in a phase difference relative to the reference arm. This phase difference is recovered after the two arms are recombined into a single output, resulting in an interference signal:

$$I_T = I_S + I_R + 2\sqrt{I_S I_R}\cos(\Delta\phi_S + \Delta\phi_0) \tag{1}$$

Here I_S and I_R are the intensities of the light propagating in the sensing and the reference arm, respectively, $\Delta\phi_0$ is the initial phase difference due to unmatched optical lengths of the two arms, and $\Delta\phi_S$ is the phase difference induced by the analyte.

2.1. Waveguide design

The sensor is based on silicon nitride (Si_3N_4) shallow rib waveguides on a silica buffer layer, fabricated by low-pressure vapour deposition and reactive-ion etching as detailed in [18, 19]. The chosen material combination exhibits good transparency in both the visible and the near-infrared range and provides for high refractive index contrast and strong lateral confinement of the optical field. Also as schematically depicted in Fig. 1, the Mach-Zehnder interferometer is top-cladded with a 1 μm-thick silica layer, with a 25 μm-wide sensing window opened above the sensing arm. Devices were fabricated with sensing lengths of 1, 2 and 3 cm.

Figure 2 shows the cross-sectional view and an atomic force microscope (AFM) image of the waveguide, characterised by a core thickness of 150 nm, rib height of 5 nm and 2 μm in width.

#245563 Received 10 Jul 2015; revised 21 Sep 2015; accepted 23 Oct 2015; published 24 Nov 2015

This design is a result of an optimisation step in order to achieve low propagation losses and a high mode-overlap with the top cladding material [19, 20].

Rib waveguides are superior to strip and slot waveguides in terms of propagation loss because of a small spatial overlap of the optical mode with the shallow-etched side-walls. A propagation loss of only 0.8 dB/cm was measured for the silica-cladded waveguides, while the polymer-cladded waveguides with cryptophane-A exhibited a slightly higher loss of 1.3 dB/cm.

As the condition of single-mode operation is indispensable for Mach-Zehnder interferometers, the waveguide dimensions were carefully chosen to support a single TE and a single TM mode at the operating wavelength λ = 785 nm. The TM mode extends more into the top cladding, and therefore it is more sensitive to changes in the surrounding environment and more suitable for evanescent sensing. When covered with a polymer sensing layer (refractive index n = 1.56), it exhibits 47% overlap with the cladding as shown in Fig. 2(a).

2.2. *Methane-sensitive layer*

The key step for selective methane detection is the use of Cryptophane-A doped layer as a cladding on the sensing arm of the Mach-Zehnder interferometer. Cryptophane-A was prepared from commercial vanillin according to a published procedure [21] and purified by column chromatography. The synthetised material was characterised by nuclear magnetic resonance and high-resolution mass spectrometry, and found to exhibit identical properties to those reported [8] including host-guest behaviour towards methane.

Although most related publications use PDMS as the host for cryptophane-A, we opt for Styrene-acrylonitrile copolymer (SAN) that exhibits good chemical resistance and high clar-

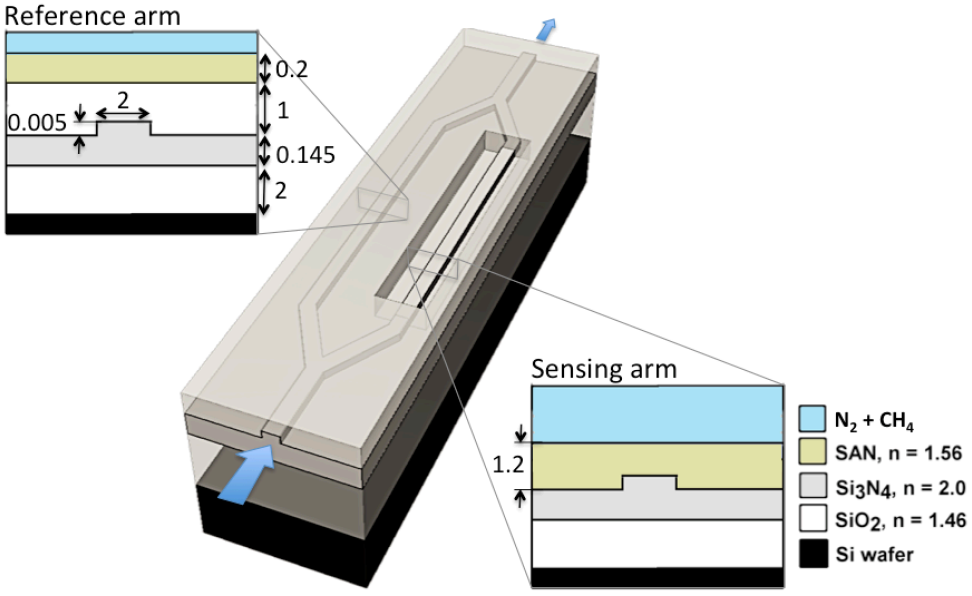

Fig. 1. 3D layout of the Mach-Zehnder interferometer, showing both the reference and the sensing arm cross-sections. The 25 µm-wide window opened above the sensing arm is filled with a cryptophane-A-doped, methane permeable polymer (SAN). This allows the methane molecules to diffuse to the waveguide surface. The waveguide dimensions and the layer thicknesses are given in micrometers.

#245563 Received 10 Jul 2015; revised 21 Sep 2015; accepted 23 Oct 2015; published 24 Nov 2015

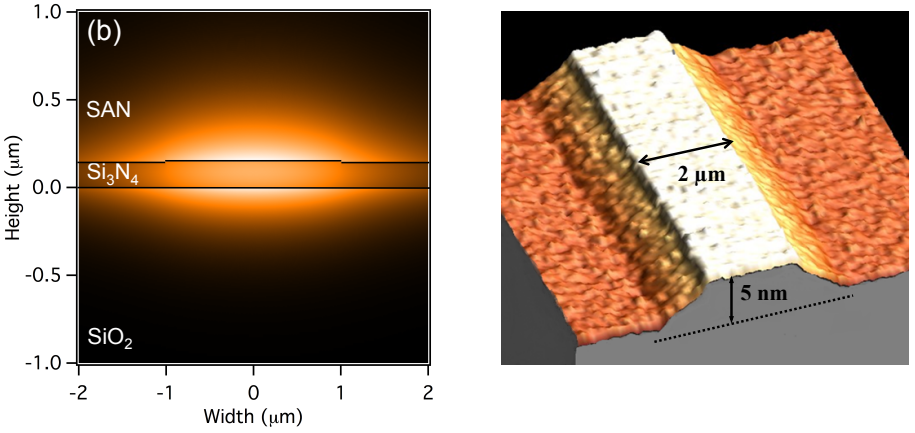

Fig. 2. The Si_3N_4 rib waveguide. (a) Numerically simulated mode field distribution of the fundamental TM mode over the waveguide cross-section; 47% of the optical field extends into the top polymer cladding. (b) AFM image of the waveguide surface; note the difference in the scaling of the lateral and the vertical axes.

ity. SAN was chosen for its compatibility with the solvent 1,1,2,2-tetrachloroethane, which can dissolve cryptophane much better than the solvents typically used with PDMS (e.g. tetrahydrofuran). This results in a higher transparency of the cladding film, which allows us to realise low-loss (1.3 dB/cm), centimeter-scale waveguides. Moreover, SAN has a higher refractive index (n = 1.56) than PDMS (n = 1.42), which has a positive effect on the field overlap and, thus, the sensitivity of the device.

The polymer was prepared from 5 mg (sensor A) or 1.6 mg (sensor B) of cryptophane-A solid powder and 45 mg SAN dissolved in 0.9 mL of 1,1,2,2-tetrachloroethane. Prior to deposition, the sample was silanized in 1% 3-aminopropyl-triethoxy silane (APTES)/ethanol solution in order to improve the adhesion of the polymer to the waveguide surface [22]. The cryptophane-A doped polymer was deposited on the chip surface by spin-coating at 4500 rpm for 2 minutes. As confirmed using KLA-Tencor P-6 stylus profiler, this resulted in a SAN film thickness of about 200 nm on the silica coated surface and 1200 nm inside the sensing windows (Fig. 2).

3. Experimental setup

The processed sensor chips were investigated using a setup that combines an optical path with a microfluidic gas-flow system for precise control of the methane flow rate and its concentration (Fig. 3). The sensor is enclosed in a microfluidic chamber with a sample volume of 0.2 mL, and mounted on a temperature-stabilised stage equipped with a Peltier element. The latter is used to control the sample temperature with an accuracy of 1 mK, and thus reduce the phase drift due to external temperature variations. TM-polarized light from a solid-state laser source emitting at 785 nm (DL785-120-SO, CrystaLaser, USA) is coupled into a polished waveguide facet using an objective lens. After propagating through the Mach-Zehnder interferometer, the output is collected at the rear sample facet by a second microscope objective and refocused on an iris, which acts as a spatial filter blocking spurious light from the sample substrate and the neighbouring slab waveguides. The output signal is detected using a silicon photodiode (NEP = 2.10^{-13}, 20 Hz bandwidth, SM1PD1A, Thorlabs, USA) and acquired at a rate of 2 Hz with a custom-written Labview program that also monitors the temperature and regulates the gas flow.

In order to investigate the response of the device to methane, two mass-flow controllers

#245563 Received 10 Jul 2015; revised 21 Sep 2015; accepted 23 Oct 2015; published 24 Nov 2015

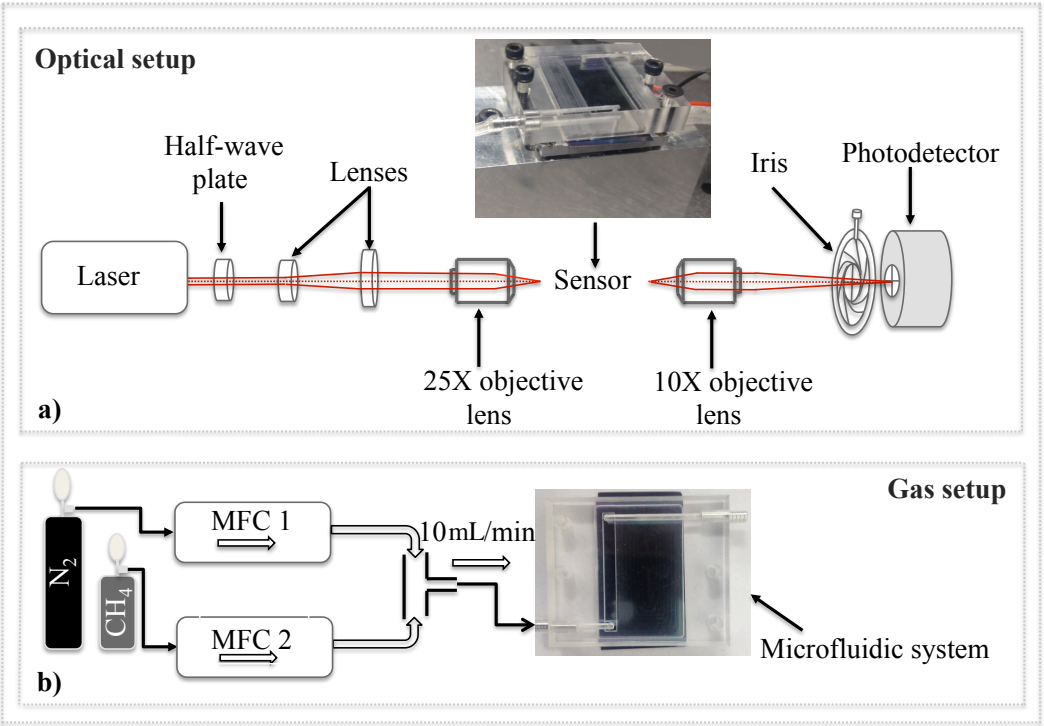

Fig. 3. Schematic diagram of (a) the optical setup and (b) the gas flow system. The top photograph shows the 25 mm × 40 mm sensor chip enclosed in a microfluidic chamber and mounted on a thermo-electrically stabilised stage.

(MFCs, 100 mL/min, EL-Flow, Bronkhorst) are used to prepare a mixture of methane and pure nitrogen (2% CH_4 in N_2). By adjusting the mixing ratios of the two gases, the methane concentration can be varied between 0 and 2%. The total gas flow through the microfluidic system is kept constant at 10 mL/min.

4. Results and discussion

Figure 4 shows the response of sensor A when alternately exposed to 2% methane or pure nitrogen. The intensity measured at the sensor output (Fig. 4(a)) exhibits a distinct and reproducible change each time the methane gas is introduced. According to Eq. (1), this intensity change is directly related to the phase difference between the interferometer arms, and can be expressed as:

$$\Delta\phi_S(t) = \Delta\phi_0 + \arccos\frac{I_T(t) - I_S - I_R}{2\sqrt{I_S I_R}} \tag{2}$$

Experimental values of I_S and I_R are obtained from the maxima and the minima of the measured intensity modulation as $I_S + I_R = (I_{max} + I_{min})/2$ and $2\sqrt{I_S}\sqrt{I_R} = (I_{max} - I_{min})/2$. The initial phase shift $\Delta\phi_0$ between the respective interferometer arms, which is always present due to different optical, thermo-optical and opto-mechanical properties, can be modified by e.g. tuning the temperature of the sensor chip. It is generally beneficial to set $\Delta\phi_0$ to $\pi/2$, i.e. in the middle of an interference fringe, where the intensity change induced by an infinitesimal phase change is maximum and thus the sensitivity of the sensor is the highest. If the phase change $\Delta\phi_S$ should exceed $\pi/2$, the result of Eq. (2) has to be unwrapped by respecting the condition of continuity of the $\Delta\phi_S(t)$ function and its first order derivative as demonstrated in Figs. 4(c) and 4(d).

#245563 Received 10 Jul 2015; revised 21 Sep 2015; accepted 23 Oct 2015; published 24 Nov 2015

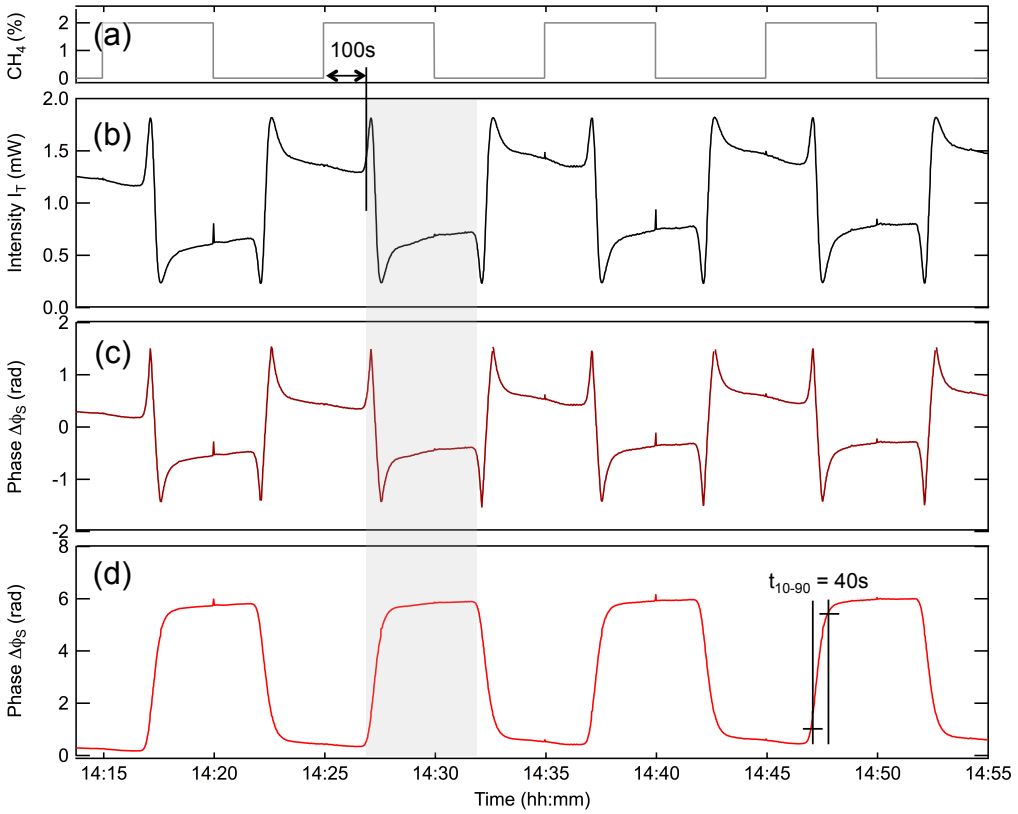

Fig. 4. Varying input methane concentration (a) and the resulting optical transmission change using sensor A (b). The corresponding phase change calculated using Eq. (2) before (c) and after unwrapping (d). The temporal offset of 100 s between the change in methane concentration and the phase response, as well as the 10% to 90% rise time of 40 s, are primarily related to the gas transport from the MFCs to the microfluidic chip. The spikes visible in the data are due to a shock wave generated upon switching between the respective MFCs.

4.1. Time response

From the temporal behaviour of the phase change (Fig. 4(d)), the sensor time response, stability and repeatability can be found. After penetration of methane into the microfluidic chamber, the phase $\Delta\phi_S$ exhibits a rapid increase with a 10% to 90% rise time $t_{10-90} = 40$ s, before it stabilises within another 80 s of measurement. The measured time constant t_{10-90} gives only an upper estimate of the response time, as in the current configuration it is not possible to decouple the response time of the sensor from the settling time of the MFCs upon switching (several seconds) and potential mixing of the gases prior to contact with the sensor surface.

Following the 120 s period of stabilisation, a small linear phase drift can still be observed in the measured signal. This is due to a rather high temperature sensitivity of the interferometer ($5.6\,\mathrm{rad}/^{\circ}C$) that reacts to any temperature variations of the sampled gas and the surrounding environment. The drift is expected to diminish in a system with only one flow control element. Furthermore, environmental changes of pressure and temperature can be compensated using a balanced interferometer, or by a reference sensor of identical design but no cryptophane-A contained in the polymer cladding.

#245563 Received 10 Jul 2015; revised 21 Sep 2015; accepted 23 Oct 2015; published 24 Nov 2015

4.2. *Sensitivity and detection limit*

In order to experimentally investigate the sensitivity, the methane concentration was varied between 300 ppm and 2%, and the methane-induced phase change was recorded as shown for sensor A in Fig. 5(a). Despite the slow temperature drift, the reproducibility of the phase change in response to the same concentration of methane was high: if the amplitude of the phase change was taken systematically after 120 s from the rise onset, the scatter of the measured data exhibited a standard deviation of only 1%, which is a good estimate of the sensor accuracy.

Figure 5(b) shows the amplitude of the phase change plotted against the methane concentration for two sensor chips A and B that differ in the Cryptophane-A amount in the polymer cladding. Both plots exhibit a linear dependence of the phase change on the methane concentration c, which allows us to define the device sensitivity as:

$$S = \frac{\Delta\phi_S}{c} \tag{3}$$

Figure 5(b) also demonstrates that the amount of Cryptophane-A has a strong influence on the device sensitivity: while the sensitivity of sensor A reaches 2.67×10^{-4} rad/ppm, the sensitivity of sensor B that contains about 3-times less Cryptophane-A is roughly 3-times lower.

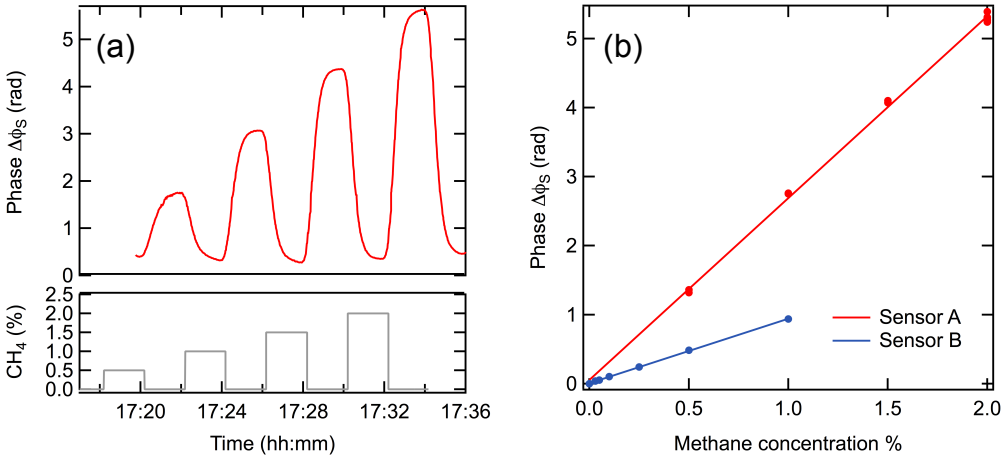

Fig. 5. (a) Recorded phase change $\Delta\phi_S$ for sensor A and 4 different methane concentrations. (b) Phase change versus methane concentration for sensors A (red) and B (blue).

The limit of detection (LOD, 99% confidence level) was calculated according to the procedure suggested by the American Chemical Society [23, 24]:

$$LOD = \frac{2.821\sigma_y}{S}, \tag{4}$$

where S is the sensitivity and σ_y is the standard deviation of the measurement at a concentration close to the expected detection limit. To find σ_y, the methane concentration was cycled 10 times between 0 and 300 ppm, and the read-out was averaged during the last 15 s of each cycle. This procedure resulted in $\sigma_y = 1.65 \times 10^{-3}$, which translates into a detection limit of 17 ppm for sensor A and 50 ppm for sensor B. These values are significantly lower than typically achieved with low-cost calorimetric or solid state sensors [4], manifesting the potential of our on-chip sensor for practical applications. The actual sensitivities and the related detection limits are summarized for both sensors in Table 1.

#245563 Received 10 Jul 2015; revised 21 Sep 2015; accepted 23 Oct 2015; published 24 Nov 2015

Table 1. Sensitivity and limit of detection for the measured sensors.

Sensor	Crypt.-A : SAN	Sensitivity (10^{-4} rad/ppm)	σ_y (10^{-3} rad)	LOD (ppm)
Sensor A	1:9	2.67	1.65	17
Sensor B	1:28	0.94	1.65	50

4.3. Sensitivity enhancement due to cryptophane

To evaluate the sensitivity enhancement due to cryptophane, we compared the above results to the response of a refractive index sensor based on the same Mach-Zehnder interferometer, but with no cryptophane-A in the polymer cladding. As shown in Fig. 6, the phase change of a 3 cm long sensor without Cryptophane-A is 0.31 rad. On the other hand, sensor A exhibits, for the same methane concentration, a phase change of 5.28 rad. This demonstrates a 17-fold sensitivity enhancement, which is likely to further increase with the amount of Cryptophane-A. However, a detailed study relating the concentration of the cryptophane to the sensitivity enhancement, scattering loss of the waveguide and the limit of detection, is still needed in order to explore the full potential of the current approach.

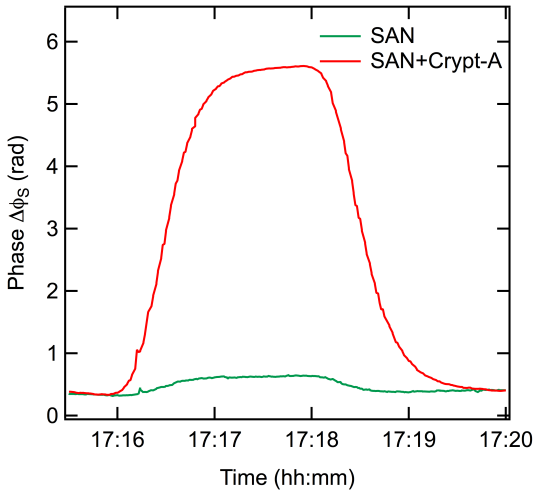

Fig. 6. Comparison of the phase response to 2% methane from sensors with and without cryptophane-A, showing a 17-fold sensitivity enhancement due to cryptophane.

4.4. Cross-sensitivity

The sensitivity enhancement observed for the cryptophane-cladded sensors indicates that 16/17 of the total phase change is related to the methane encapsulation in the cryptophane cages. Only the remaining fraction of the phase change is non-specific, i.e., related to the refractive index change of the gas regardless of its chemical composition. Therefore, the cross-sensitivity of the sensor to other gases is scaled by the same factor, and can be eliminated by using a reference sensor cladded by a pure SAN film without the cryptophane component. Nevertheless, interference with the few species that also exhibit high affinity to cryptophane-A, such as xenon, radon and chloromethanes [8, 25, 26], is hard to avoid. This should be quantified and taken into consideration when targeting practical applications.

#245563 Received 10 Jul 2015; revised 21 Sep 2015; accepted 23 Oct 2015; published 24 Nov 2015

5. Conclusions

In summary, we have demonstrated an on-chip methane sensor based on an integrated Mach-Zehnder interferometer, which uses a polymer cladding doped with cryptophane-A to increase the sensitivity and selectivity. The choice of styrene-acrylonitrile as a host polymer for cryptophane molecules was a key to the successful realisation of low-loss centimetre-scale waveguides, constituting the principal building block of the sensor. Our approach resulted in a 17-fold sensitivity enhancement compared to a refractive index sensor, and a detection limit as low as 17 ppm. This sensitivity is sufficient for practical use in safety and process control, as well as in some environmental applications such as monitoring of methane emission sources. Furthermore, the 1200 nm-thin cladding, matched to the decay length of the evanescent field, provides for fast methane diffusion and, hence, fast response of the sensor. The sensor chips are small, light, and, when pigtailed with optical fibres, sufficiently rigid for air-borne deployment. Moreover, since they are patterned with standard photolithography, the sensor chips are cheap and eligible for mass production.

In the next step, our efforts will focus on increasing the chip sensitivity by optimising the cryptophane cage size, as well as shifting the excitation wavelength to a region of strong methane dispersion. Moreover, a new chip design comprising reference interferometers will be proposed to compensate for temperature and pressure drift and to increase the long-term stability and specificity of the sensor. Our final aim is to make a prototype sensor for installation on a civilian drone, to conduct surveys of remote and poorly-accessible natural methane sources.

Acknowledgments

The first two authors contributed equally to this work. The work is a part of the project Sensor Technology, funded by the Research Council of Norway (grant 195308). The authors want tho acknowledge the support from Laura Lechuga Gómez (ICN, Barcelona, Spain), as well as Carlos Dominguez and co-workers (CSIC, Barcelona, Spain) who fabricated the waveguides.

#245563 Received 10 Jul 2015; revised 21 Sep 2015; accepted 23 Oct 2015; published 24 Nov 2015

Chapter 7

Conclusion and future work

7.1 Conclusion

This dissertation describes the initial development and characterisation of an optical waveguide interferometer for detection of methane gas and methane in water. Methane is measured with a sensing layer, consisting of a polymer with a supra-molecular compound that entraps the methane molecule. The waveguide interferometer detects the change in refractive index in the sensing layer, when the methane molecules are accumulated. Simulations were made to find the optimised design parameters for silicon nitride (Si_3N_4) waveguides, giving high sensitivity with respect to change in refractive index and single-mode waveguides with low losses.

In paper 1, propagation losses were measured for tantalum pentoxide strip waveguides and rib waveguides, similar to silicon nitride in refractive index. Scattering losses caused by random sidewall imperfections are dependent on fabrication and can vary along a waveguide. As the sidewalls of a rib waveguide are lower than those of a strip waveguide, scattering losses are expected to be smaller for a rib than for a strip waveguide. The propagation losses were measured with a non-destructive method of recording the scattered light along the waveguide. It was found that the propagation losses increased sharply for strip waveguides with a width smaller than 3 μm. The propagation losses were significantly smaller for rib waveguides than for the strip waveguides. The scattering loss was simulated by adding an area with complex refractive index in the 2D-model of the waveguide. The measured loss of a reference waveguide with a given width was used to estimate the complex refractive index by measuring the propagation losses for that waveguide. The model gave a good estimate of the dependency of the propagations losses on waveguide width. The measured and simulated dependency of propagation losses on waveguide width, give valuable information for the design of rib waveguides. For silicon-nitride waveguides with 5 nm rib height, the propagation losses were measured to 0.8 - 1.3 dB/cm.

In paper 2, the mode-behaviour and the sensitivity of the proposed sensor was investigated with COMSOL. It was shown that the sensitivity to refractive index changes is mainly dependent on the refractive index of the core and cover medium, core thickness, wavelength and polarisation. Maximum sensitivity was obtained for a core thickness of 60 nm (TE-polarisation) and 120 nm (TM-polariation), with PDMS as the cover medium. The sensitivity was found to be approximately 18% higher for TM-polarization than for TE-polarization. Strip waveguides give slightly higher sensitivity (4 to 8%) than rib waveguides. However, as shown in paper 1, strip waveguides have higher propagation losses and must be less than 1 μm wide to be single-mode.

Based on the simulations, the waveguide interferometers were designed with shallow rib waveguides, with a 150 nm thick silicon nitride core, waveguide widths of 1.5, 2 and 3 μm and a rib height of 5 nm.

The sensors were characterised regarding sensitivity to change of refractive index, using two different methods. With increasing concentrations of HCl and with a sensing length of 2 cm, a sensitivity of $13.0\times10^3\pi$ rad/RIU and a detection limit of $1.1\times10^{-7}\pi$ RIU was found, comparable to the results published in the literature [55, 58]. The limit of detection may be improved by reducing the noise of the system by optimising the design of the microfluidic chamber. The sensitivity was also measured with a PDMS layer deposited onto the sensor. A phase change was obtained by inducing a temperature change to the sensor, which decreases the refractive index of the cover medium. For a sensing length of 2 cm, a sensitivity of $15.2\times10^3\pi$ rad/RIU and a detection limit of $1.3\times10^{-7}\pi$ RIU was obtained, thus similar to the values obtained with HCl. It is also possible to use the PDMS for temperature measurements with a detection limit of 1 mK, as demonstrated in paper 2. Since this paper was published, styrene acrylonitrile (SAN) was chosen as cover medium. The SAN polymer gives a much higher theoretical bulk sensitivity of 0.54, compared to 0.34 for PDMS, giving a sensitivity of $26.0\times10^3\pi$ rad/RIU for a 2 cm long sensing length.

In paper 3, measurements of methane gas was demonstrated with an on-chip Mach-Zehnder interferometer. The surface of the sensor was coated with a 200nm-thick layer of SAN, mixed with cryptophane-A for high sensitivity and selectivity. With a cryptophane-A:SAN ratio of 1:9 in the sensing layer, a 17-fold increase of the sensitivity was shown relative to pure SAN. The sensitivity could potentially increase with the amount of cryptophane-A. This, however, has to be studied further with respect to scattering losses, sensitivity and limit of detection. With a cryptophane-A:SAN ratio of 1:9 in the sensing layer, a detection limit of 17 ppm was obtained. This is 1-2 orders of magnitude lower than typically obtained with a low-cost and mobile evanescent field sensor.

In addition to the work and the results presented in the three papers, methane dissolved in water was detected with the sensor. The SAN polymer showed to be unstable

in contact with water and a protective layer of PDMS was deposited to cover the methane sensitive layer. Experiments showed that the protected coating (SAN with PDMS) still caused problems with small bubbles appearing, giving rise to scattering along the sensing window. The amplitude of the fringes decreased with time, until in some cases the intensity was completely lost in the sensing windows. Despite these problems, dissolved methane was measured with two sensors. A sensitivity of 3.48×10^{-2} rad/nM and a detection limit of 49 nM was obtained. This demonstrates that the sensor is suitable for measurements of methane dissolved in water.

7.2 Future work

Along the way of designing and characterising the waveguide interferometer, some insights have been gained. With the sensitivity being directly proportional to the sensing length, the sensitivity can be improved by increasing the sensing length while keeping the propagation and bending losses low. The sensitivity can also be improved by increasing the concentration of cryptophane-A. However, too high concentrations may be difficult to dissolve and may cause scattering in the sensing window. Cryptophanes has a strong affinity towards methane, but it can also entrap other neutral molecules that fits within its cavity. By optimising the size of the cage, the cross-sensitivity and sensitivity towards methane may be further improved.

Instabilities, such as temperature-induced drifts, can be improved by using symmetric Mach-Zehnder interferometers, i.e. a sensing arm covered with the sensing polymer (SAN with Cryptophane-A) and the second arm covered with pure polymer (SAN only). More stable in-coupling (e.g. using fibre pigtail or grating) can reduce noise from the in-coupling and thus improve the limit of detection. In addition, stability can be improved further by adding a reference arm with a y-junction before the Mach-Zehnder interferometer, to measure variations in the guided power.

Further investigations may include measurement of the cross-sensitivity to other dissolved gases, the effects from exposure of seawater (water with higher salinity), the mixing of methane in water (regarding reproducibility and homogeneity) and measurements with lower concentrations (less than 10μM) to find the ultimate detection limit of the sensor. Most important, in order to improve the sensor for measurements of dissolved methane, is finding an alternative polymer that meets the requirements of the host-polymer and is resistant to water.

Bibliography

[1] J. Yang, J. Huang, X. Li, S. Li, B. Luo, C. Tao, and W. Chen. High-sensitivity long-period fiber grating sensor with SAN/cryptophane-A for coal mine gas detection. Chinese Optics Letters, 11(8):080601, August 2013.

[2] C. Boulart, R. Prien, V. Chavagnac, and J-P. Dutasta. Sensing dissolved methane in aquatic environments: an experiment in the central Baltic Sea using surface plasmon resonance. Environmental science & technology, 47(15):8582–8590, July 2013.

[3] S. Wu, Y. Zhang, Z. Li, S. Shuang, C. Dong, and M. Choi. Mode-filtered light methane gas sensor based on cryptophane-A. Analytica Chimica Acta, 633(2): 238–243, February 2009.

[4] M. Benounis, N. Jaffrezic-Renault, J.-P. Dutasta, K. Cherif, and A. Abdelghani. Study of a new evanescent wave optical fibre sensor for methane detection based on cryptophane molecules. Sensors and Actuators B: Chemical, 107(1):32–39, May 2005.

[5] T. F. Stocker (Ed.) and et al. Climate change 2013: the physical science basis: Working Group I contribution to the Fifth assessment report of the Intergovernmental Panel on Climate Change. Cambridge University Press, Mars 2014.

[6] C. Davenport. Obama is planning new rules on oil and gas industry's methane emissions, 2015. URL `http://www.nytimes.com/2015/01/14/us/politics/obama-administration-to-unveil-plans-to-cut-methane-emissions.html?_r=0`.

[7] A. Takahashi, Y. Urano, K. Tokuhashi, and S. Kondo. Effect of vessel size and shape on experimental flammability limits of gases. Journal of hazardous materials, 105 (1):27–37, December 2003.

[8] J. W. Steed and J. L. Atwood. Supramolecular chemistry. John Wiley & Sons, May 2013.

[9] T. Liu, C. Wang, Y. Wei, Y. Zhao, D. Huo, Y. Shang, Z. Wang, and Y. Ning. Fibre optic sensors for mine hazard detection. Journal of Physics: Conference Series, 178 (1):012004, 2009.

[10] R. S. Keir, O. Schmale, R. Seifert, and J. Sültenfuß. Isotope fractionation and mixing in methane plumes from the Logatchev hydrothermal field. Geochemistry, Geophysics, Geosystems, 10(5), May 2009.

[11] O. Schmale, J. Schneider von Deimling, W. Gülzow, G. Nausch, J. J. Waniek, and G. Rehder. Distribution of methane in the water column of the Baltic Sea. Geophysical Research Letters, 37(12), June 2010.

[12] W. Wang, H. Hu, S. He, Y. Pan, C. Zhang, and C. Dong. A room temperature SAW based methane gas sensors. In Ultrasonics Symposium (IUS), 2013 IEEE International, pages 2148–2150. IEEE, July 2013.

[13] G. Abril, S. Richard, and F. Guérin. In situ measurements of dissolved gases (CO_2 and CH_4) in a wide range of concentrations in a tropical reservoir using an equilibrator. Science of the Total Environment, 354(2):246–251, February 2006.

[14] N. S. Lawrence. Analytical detection methodologies for methane and related hydrocarbons. Talanta, 69(2):385–392, 2006.

[15] J. Su, L. Cao, L. Li, J. Wei, G. Li, and Y. Yuan. Highly sensitive methane catalytic combustion micro-sensor based on mesoporous structure and nano-catalyst. Nanoscale, 5(20):9720–9725, 2013.

[16] X. Liu, S. Cheng, H. Liu, S. Hu, D. Zhang, and H. Ning. A survey on gas sensing technology. Sensors, 12(7):9635–9665, July 2012.

[17] J. Shemshad, S. M. Aminossadati, and M. S. Kizil. A review of developments in near infrared methane detection based on tunable diode laser. Sensors and Actuators B: Chemical, 171:77–92, September 2012.

[18] J. Kamieniak, E. P. Randviir, and C. E. Banks. The latest developments in the analytical sensing of methane. TrAC Trends in Analytical Chemistry, 73:146–157, November 2015.

[19] P. Bergamaschi, M. Schupp, and G. W. Harris. High–precision direct measurements of $^{13}CH_4/^{12}CH_4$ and $^{12}CH_3D/^{12}CH_4$ ratios in atmospheric methane sources by means of a long-path tunable diode laser absorption spectrometer. Applied Optics, 33(33):7704–7716, November 1994.

[20] H. Xia, W. Liu, Y. Zhang, R. Kan, M. Wang, Y. He, Y. Cui, J. Ruan, and H. Geng. An approach of open–path gas sensor based on tunable diode laser absorption spectroscopy. Chinese Optics Letters, 6(6):437–440, June 2008.

[21] P. Pandey and R. S. Chauhan. Membranes for gas separation. Progress in Polymer Science, 26(6):853–893, August 2001.

[22] S. De Gregorio, S. Gurrieri, and M. Valenza. A PTFE membrane for the in situ extraction of dissolved gases in natural waters: Theory and applications. Geochemistry, Geophysics, Geosystems, 6(9), September 2005.

[23] R. J. Bell, R. T. Short, F. H. W. Van Amerom, and R. H. Byrne. Calibration of an in situ membrane inlet mass spectrometer for measurements of dissolved gases and volatile organics in seawater. Environmental science & technology, 41(23): 8123–8128, October 2007.

[24] M.-C. Caumon, P. Robert, E. Laverret, A. Tarantola, A. Randi, J. Pironon, J. Dubessy, and J.-P. Girard. Determination of methane content in $NaCl - H_2O$ fluid inclusions by Raman spectroscopy. Calibration and application to the external part of the Central Alps (Switzerland). Chemical Geology, 378:52–61, June 2014.

[25] H. Schmidt, N. B. Ha, J. Pfannkuche, H. Amann, H.-D. Kronfeldt, and G. Kowalewska. Detection of PAHs in seawater using surface–enhanced Raman scattering (SERS). Marine pollution bulletin, 49(3):229–234, August 2004.

[26] M. Schlüter and T. Gentz. Application of membrane inlet mass spectrometry for online and in situ analysis of methane in aquatic environments. Journal of the American Society for Mass Spectrometry, 19(10):1395–1402, October 2008.

[27] T. Gentz and M. Schlüter. Underwater cryotrap–membrane inlet system (CT–MIS) for improved in situ analysis of gases. Limnology and Oceanography: Methods, 10 (5):317–328, 2012.

[28] A. Rogalski and K. Chrzanowski. Infrared devices and techniques. Optoelectronics Review, 10(2):111–136, June 2002.

[29] M. A. Linne. Spectroscopic measurement: an introduction to the fundamentals. Academic Press, July 2002.

[30] M. Schmidt, P. Linke, and D. Esser. Recent development in IR sensor technology for monitoring subsea methane discharge. Marine Technology Society Journal, 47 (3):27–36, May 2013.

[31] C. Boulart. Methane in deep sea hydrothermal plumes. Development of a new in-situ methane sensing technology. Doctoral dissertation, University of Southampton, 2008.

[32] F. Vogt, N. Pennington, B. Mizaikoff, et al. Mid-infrared spectroscopic sensors for in-situ monitoring of methane dissolved in sea water. In Offshore Technology Conference. Offshore Technology Conference, January 2003.

[33] S. D. Wankel, Y.-W. Huang, M. Gupta, R. Provencal, J. B. Leen, A. Fahrland, C. Vidoudez, and P. R. Girguis. Characterizing the distribution of methane sources and cycling in the deep sea via in situ stable isotope analysis. Environmental science & technology, 47(3):1478–1486, January 2013.

[34] R. Camilli and A. Duryea. Characterizing marine hydrocarbons with in-situ mass spectrometry. In OCEANS 2007, pages 1–7. IEEE, September 2007.

[35] C. Boulart, D. P. Connelly, and M. C. Mowlem. Sensors and technologies for in situ dissolved methane measurements and their evaluation using technology readiness levels. TrAC Trends in Analytical Chemistry, 29(2):186–195, February 2010.

[36] P. G. Brewer, G. Malby, J. D. Pasteris, S. N. White, E. T. Peltzer, B. Wopenka, J. Freeman, and M. O. Brown. Development of a laser raman spectrometer for deep-ocean science. Deep Sea Research Part I: Oceanographic Research Papers, 51 (5):739–753, May 2004.

[37] T. Murphy, S. Lucht, H. Schmidt, and H.-D. Kronfeldt. Surface-enhanced raman scattering (SERS) system for continuous measurements of chemicals in sea-water. Journal of Raman spectroscopy, 31(10):943–948, October 2000.

[38] J. D. Pasteris, B. Wopenka, J. J. Freeman, P. G. Brewer, S. N. White, E. T. Peltzer, and G. E. Malby. Raman spectroscopy in the deep ocean: successes and challenges. Applied Spectroscopy, 58:195A–195A, July 2004.

[39] K. C. Hester, R. M. Dunk, S. N. White, P. G. Brewer, E. T. Peltzer, and E. D. Sloan. Gas hydrate measurements at Hydrate Ridge using Raman spectroscopy. Geochimica et Cosmochimica Acta, 71(12):2947–2959, June 2007.

[40] K. C. Hester, S. N. White, E. T. Peltzer, P. G. Brewer, and E. D. Sloan. Raman spectroscopic measurements of synthetic gas hydrates in the ocean. Marine Chemistry, 98(2):304–314, February 2006.

[41] M. Sackmann and A. Materny. Surface enhanced raman scattering (SERS)-a quantitative analytical tool? Journal of Raman Spectroscopy, 37(1-3):305–310, 2006.

[42] A. Otto. Excitation of nonradiative surface plasma waves in silver by the method of frustrated total reflection. Zeitschrift für Physik, 216(4):398–410, August 1968.

[43] J. Homola. Surface plasmon resonance sensors for detection of chemical and biological species. Chemical reviews, 108(2):462–493, February 2008.

[44] S. Y. Wu, H. P. Ho, W. C. Law, C. Lin, and S. K. Kong. Highly sensitive differential phase-sensitive surface plasmon resonance biosensor based on the Mach–Zehnder configuration. Optics Letters, 29(20):2378–2380, October 2004.

[45] M.-C. Estevez, M. Alvarez, and L. M. Lechuga. Integrated optical devices for lab-on-a-chip biosensing applications. Laser & Photonics Reviews, 6(4):463–487, July 2012.

[46] T. Urashi and T. Arakawa. Detection of lower hydrocarbons by means of surface plasmon resonance. Sensors and Actuators B: Chemical, 76(1):32–35, June 2001.

[47] Z. Sun, Y. He, and J. Guo. Surface plasmon resonance sensor based on polarization interferometry and angle modulation. Applied optics, 45(13):3071–3076, May 2006.

[48] L. Liu, Z. Hu, S. Ma, Y. Zhang, Y. He, and J. Guo. Detection of methane by a surface plasmon resonance sensor based on polarization interferometry and angle modulation. Optics and Lasers in Engineering, 48(12):1182–1185, May 2010.

[49] C. Boulart, M. C. Mowlem, D. P. Connelly, J.-P. Dutasta, and C. R. German. A novel, low-cost, high performance dissolved methane sensor for aqueous environments. Optics express, 16(17):12607–12617, May 2008.

[50] H. Waechter, J. Litman, A. H. Cheung, J. A. Barnes, and H.-P. Loock. Chemical sensing using fiber cavity ring-down spectroscopy. Sensors, 10(3):1716–1742, Mars 2010.

[51] J. Yang, C. Tao, X. Li, G. Zhu, and W. Chen. Long-period fiber grating sensor with a Styrene-Acrylonitrile nano-film incorporating cryptophane-A for methane detection. Optics express, 19(15):14696–14706, July 2011.

[52] L. Zehnder. Ein neuer Interferenzrefraktor. Springer, 1891.

[53] L. Mach. Uber einen interferenzrefraktor. Z. für Instrumentenkunde, 12:89–93, 1892.

[54] P. Kozma, F. Kehl, E. Ehrentreich-Förster, C. Stamm, and F. F. Bier. Integrated planar optical waveguide interferometer biosensors: A comparative review. Biosensors and Bioelectronics, 58:287–307, August 2014.

[55] K. Zinoviev, L. G. Carrascosa, J. Sánchez del Río, B. Sepúlveda, C. Domínguez, and L. M. Lechuga. Silicon photonic biosensors for lab-on-a-chip applications. Advances in Optical Technologies, page 6, June 2008.

[56] A. Ymeti, J. S. Kanger, J. Greve, G. A. J. Besselink, P. V. Lambeck, R. Wijn, and R. G. Heideman. Integration of microfluidics with a four-channel integrated optical Young interferometer immunosensor. Biosensors and Bioelectronics, 20(7): 1417–1421, January 2005.

[57] R. G. Heideman and P. V. Lambeck. Remote opto-chemical sensing with extreme sensitivity: design, fabrication and performance of a pigtailed integrated optical phase-modulated Mach–Zehnder interferometer system. Sens. Actuators B: Chem., 61(1):100–127, December 1999.

[58] S. Dante, D. Duval, B. Sepúlveda, A. B. González-Guerrero, J. R. Sendra, and L. M. Lechuga. All-optical phase modulation for integrated interferometric biosensors. Optics express, 20(7):7195–7205, Mars 2012.

[59] Stefania Dante. All-optical phase modulation for advanced interferometric point-of-care biosensors. Doctoral dissertation, Universitat Autónoma de Barcelona, December 2014.

[60] Optisense, 2015. URL `http://www.optisense.nl/content/blogcategory/18/38/`.

[61] X. Xu, S. Chen, J. Yu, and X. Tu. An investigation of the mode characteristics of SOI submicron rib waveguides using the film mode matching method. Journal of Optics A: Pure and Applied Optics, 11(1):015508, December 2009.

[62] F. T. Dullo, J.-C. Tinguely, S. A. Solbø, and O. G. Hellesø. Single-mode limit and bending losses for shallow rib waveguides. Photonics Journal, IEEE, 7(1):1–11, February 2015.

[63] F. Prieto, B. Sepulveda, A. Calle, A. Llobera, C. Domínguez, A. Abad, A. Montoya, and L. M. Lechuga. An integrated optical interferometric nanodevice based on silicon technology for biosensor applications. Nanotechnology, 14(8):907, July 2003.

[64] K. Tiefenthaler and W. Lukosz. Sensitivity of grating couplers as integrated-optical chemical sensors. JOSA B, 6(2):209–220, February 1989.

[65] F. Prieto, A. Llobera, A. Calle, and L. M. Lechuga. Design and analysis of silicon antiresonant reflecting optical waveguides for evanscent field sensor. J. Lightw. Technol., 18(7):966, July 2000.

[66] R. G. Hunsperger. Integrated optics: Theory and technology, volume 2. Springer, 1984.

[67] F. P. Payne and J. P. R. Lacey. A theoretical analysis of scattering loss from planar optical waveguides. Opt. and Quant. Electr., 26(10):977–986, October 1994.

[68] D. Marcuse. Mode conversion caused by surface imperfections of a dielectric slab waveguide. Bell Syst. Tech. J., 48(10):3187–3215, December 1969.

[69] F. Grillot, L. Vivien, S. Laval, D. Pascal, and E. Cassan. Size influence on the propagation loss induced by sidewall roughness in ultrasmall SOI waveguides. Photonics Technology Letters, IEEE, 16(7):1661–1663, July 2004.

[70] T. Barwicz and H. A. Haus. Three-dimensional analysis of scattering losses due to sidewall roughness in microphotonic waveguides. Lightwave Technology, Journal of, 23(9):2719–2732, September 2005.

[71] G. L. Klunder and R. E. Russo. Core-based intrinsic fiber-optic absorption sensor for the detection of volatile organic compounds. Applied spectroscopy, 49(3):379–385, Mars 1995.

[72] L. Garel, J.-P. Dutasta, and A. Collet. Complexation of methane and chlorofluorocarbons by cryptophane-A in organic solution. Angewandte Chemie International Edition in English, 32(8):1169–1171, August 1993.

[73] T. Brotin and J.-P. Dutasta. Xe@ cryptophane complexes with C_2 symmetry: Synthesis and investigations by ^{129}xe NMR of the consequences of the size of the host cavity for xenon encapsulation. European Journal of Organic Chemistry, 2003 (6):973–984, Mars 2003.

[74] O. Taratula, P. A. Hill, N. S. Khan, P. J. Carroll, and I. J. Dmochowski. Crystallographic observation of 'induced fit' in a cryptophane host–guest model system. Nature communications, 1:148, December 2010.

[75] E. Souteyrand, D. Nicolas, J. R. Martin, J. P. Chauvet, and H. Perez. Behaviour of cryptophane molecules in gas media. Sensors and Actuators B: Chemical, 33(1): 182–187, July 1996.

[76] K. Bartik, M. Luhmer, J.-P. Dutasta, A. Collet, and J. Reisse. ^{129}xe and ^{1}H NMR study of the reversible trapping of xenon by cryptophane-A in organic solution. Journal of the American Chemical Society, 120(4):784–791, February 1998.

[77] J. Canceill and A. Collet. Two-step synthesis of D_3 and C_{3h} cryptophanes. Journal of the Chemical Society, Chemical Communications, -(9):582–584, 1988.

[78] K. E. Chaffee, H. A. Fogarty, T. Brotin, B. M. Goodson, and J.-P. Dutasta. Encapsulation of small gas molecules by cryptophane-111 in organic solution. 1. size- and shape-selective complexation of simple hydrocarbons. The Journal of Physical Chemistry A, 113(49):13675–13684, November 2009.

[79] Z. Tošner, O. Petrov, S. V. Dvinskikh, J. Kowalewski, and D. Sandström. A ^{13}C solid-state NMR study of cryptophane-E: chloromethane inclusion complexes. Chemical physics letters, 388(1):208–211, April 2004.

[80] J. Friend and L. Yeo. Fabrication of microfluidic devices using polydimethylsiloxane. Biomicrofluidics, 4(2):026502, June 2010.

[81] D. A. Chang-Yen, R. K. Eich, and B. K. Gale. A monolithic PDMS waveguide system fabricated using soft-lithography techniques. Journal of lightwave technology, 23(6):2088, June 2005.

[82] A. H. Khoshaman. Application of electrospun thin films for supra-molecule based gas sensing. Doctoral dissertation, Applied Science: School of Engineering Science, August 2011.

[83] D. MacDougall and W. B. Crummett. Guidelines for data acquisition and data quality evaluation in environmental chemistry. Analytical Chemistry, 52(14):2242–2249, December 1980.

[84] H.-P. Loock and P. D. Wentzell. Detection limits of chemical sensors: Applications and misapplications. Sensors and Actuators B: Chemical, 173:157–163, October 2012.

[85] R. M. van Dam. Solvent-resistant elastomeric microfluidic devices and applications. Doctoral dissertation, California Institute of Technology, Engineering and Applied Science, August 2006.

[86] D. Psaltis, S. R. Quake, and C. Yang. Developing optofluidic technology through the fusion of microfluidics and optics. Nature, 442(7101):381–386, July 2006.